Engineering the Synthesis and Properties of Two-Dimensional Colloidal Perovskite Nanoplatelets

by

Seung Kyun Ha

Bachelor of Science in Chemical and Biological Engineering
Seoul National University, 2015

Master of Science in Chemical Engineering Practice
Massachusetts Institute of Technology, 2017

Submitted to the Department of Chemical Engineering
in partial fulfillment of the requirements for the degree of
DOCTOR OF PHILOSOPHY IN CHEMICAL ENGINEERING
at the
MASSACHUSETTS INSTITUTE OF TECHNOLOGY
September 2021

Signature of Author ……...

Seung Kyun Ha

Department of Chemical Engineering

June 22nd, 2021

Certified by ……..……..

William A. Tisdale

ARCO Career Development Professor of Chemical Engineering

Thesis Supervisor

Accepted by ……..

Patrick S. Doyle

Robert T. Haslam (1911) Professor of Chemical Engineering

Chairman, Committee for Graduate Students

Engineering the Synthesis and Properties of Two-Dimensional Colloidal Perovskite Nanoplatelets

by
Seung Kyun Ha

Submitted to the Department of Chemical Engineering on June 22, 2021 in partial fulfillment of the requirements for the degree of Doctor of Philosophy in Chemical Engineering

Abstract

Colloidal semiconductor nanocrystals are among the leading material platforms for a wide range of optoelectronic applications including photovoltaics, displays, photodetectors, and thermoelectrics. Their colloidal stability enables facile device fabrication by providing solution processability, and tunability of the bandgap with particle size opens up the opportunity to independently optimize nanocrystal properties for specific applications. Recently, colloidal lead halide perovskite nanoplatelets (chemical formula: $L_2[ABX_3]_{n-1}BX_4$, L: alkylammonium, A: methylammonium or formamidinium or cesium, B: lead, X: halide, n: number of $[BX_6]^{4-}$ octahedral layers in the direction of thickness) have emerged as a promising class of novel semiconductor nanocrystals capitalizing on their strong absorption, bright emission with high color purity, strong quantum- and dielectric-confinement, and anisotropic transition dipole moment orientation. This dissertation seeks to establish a robust synthetic protocol for the preparation of colloidal perovskite nanoplatelets and further engineer their desirable properties.

First, I briefly review the history of perovskite nanoplatelets and introduce a protocol for the facile synthesis of colloidal perovskite nanoplatelets at room-temperature. Monodispersity of the nanoplatelets is confirmed by optical and structural characterizations. Photoluminescence and absorption spectra reveal strongly-confined excitonic features which can be tuned in the visible range by changing nanoplatelet thickness and varying the composition of halide anions. Furthermore, I show that multiple species of surface-bound alkylammonium ligands can be introduced. This demonstrates the possibility of further optimizing the surface properties of nanoplatelets which can hugely impact the charge transport behavior inside the device as well as the operating stability.

Then I focus on lead bromide nanoplatelets, whose deep-blue luminescence makes it one of the leading light-emitting platforms for the next-generation displays. I systematically investigate key factors that determine the stability of the nanoplatelets under UV excitation, which mimics the condition of hot-carrier injection into an operating device. It is shown that the freshness of the perovskite precursor solution is crucial in maintaining the stability and efficient luminescence. Then I show that the decrease in photoluminescence intensity upon UV irradiation primarily results from intrinsic instability of the perovskite lattice, whereas the moisture triggers the transformation of nanoplatelets into thicker nanostructures. Then substitution of the organic cation from formamidinium to methylammonium and the addition of excess alkylammonium bromide ligands during the synthesis are shown to be effective stabilization strategies.

Lastly, doping of manganese (Mn^{2+}) ions — a powerful method for manipulating excited state dynamics and altering semiconductor nanocrystal properties — in colloidal perovskite nanoplatelets is demonstrated. Substitutional doping of manganese for lead introduces bright and

long-lived mid-gap Mn^{2+} atomic states, and the doped nanoplatelets exhibit dual emission from the band edge and the dopant state due to facile band edge-to-dopant excitation transfer. I show that photoluminescence quantum yields and band-edge-to-dopant photoluminescence intensity ratios exhibit strong excitation power dependence that cannot be explained by the saturation of long-lived dopant states. By developing a kinetic model combined with time-resolved spectroscopic studies, it is demonstrated that the annihilation of dopant-site excitons by interacting with band-edge excitons is responsible for the observed power dependence. Then I discuss significantly faster band edge-to-dopant excitation transfer in methylammonium-containing nanoplatelets compared to the transfer in formamidinium-containing nanoplatelets.

Thesis Supervisor: William A. Tisdale
Title: ARCO Career Development Professor of Chemical Engineering

Acknowledgements

First of all, I would like to thank my advisor Prof. William Tisdale. Will has given me great guidance throughout my PhD, shown me how to become an independent researcher, and always supported every decision I made. His passion for science has always been inspirational. He has respected my opinions and made himself available whenever I needed his advice, both in and outside of research. He always supported my decisions of taking more classes and being involved in student organizations even if they were not directly relevant to the research, saying that I should maximize learning opportunities at MIT as a graduate student. Thanks to his support, I have had great learning experiences at MIT, and I will always be grateful to Will for that. I also truly respect Will's efforts on building the inclusive and friendly group culture. I was lucky to have an opportunity to pursue my PhD in such a great environment, and joining the Tisdale lab was the best decision I made at MIT.

I would also like to thank the members of my thesis committee: Prof. Heather Kulik and Prof. Vladimir Bulovic. Heather's intuition about modeling has always inspired me to think about the fundamentals of the materials. Vladimir's expertise in optoelectronics and materials physics have given me new perspectives, which prompted new ideas and enriched my project. Also, their support in my research ideas has made me feel that I am working on an important scientific problem and given me additional motivation to drive the research.

Also, I would like to acknowledge Center for Excitonics and US Department of Energy for funding my research, and Kwanjeong Educational Foundation for supporting me with a fellowship.

I was lucky to join such a friendly and cohesive group. I have enjoyed every moment in the Tisdale lab and appreciate all the members of the group for making me feel at home. I have not only enjoyed spending time with them, but also learned a lot from them by working together. Mark Weidman and Michael Seitz introduced me to the world of perovskite nanoplatelets. Katie Mauck taught me how to interpret FTIR and NMR analysis data. Wenbi Shcherbakov-Wu and Watcharaphol "Oat" Paritmongkol always helped me designing the experiments and answered my spectroscopy-related questions. Eric Powers showed me how to analyze transient absorption data, and Kris Williams provided me valuable insights on the interaction of excitons in nanoplatelets. Furthermore, I have been fortunate enough to meet all those talented scientists throughout my PhD: Yunan (Steve!) Gao, Dan Congreve, Jolene Mork, Rachel Gilmore, Liza Lee, Aaron Goodman (and Buddy), Matt Ashner, Nabeel Dahod, Dahin Kim, Katie Shulenberger, Sam Winslow, Leo Spiegel, Deepankur Thureja, Alexia Stollmann, Alex Hernandez Oendra, Makhsud Saidaminov, Nannan Mao, Ruomeng Wan, Woo Seok Lee, Narumi Wong, Abby Taussig and Tomoaki Sakurada. Everyone has taught me invaluable lessons, both in and out of the lab. I also had the privilege of working with talented undergraduate students throughout my PhD. I would like to thank Nick Morgante, Sarai Patterson, and Abraham Corea Diaz for working with me on my projects. And I appreciate Barb Balkwill's presence and availability. I have always enjoyed visiting her office and talking about the day.

I also had great collaborators. Carolyn Mills and Helen Yao from the Olsen lab helped me with dynamic light scattering measurements. Dong-Gwang "DG" Ha from the Baldo lab helped me with time-resolved photoluminescence measurements. Mahesh Gangishetty from the Congreve lab at Rowland Institute at Harvard showed me how to make a light-emitting diodes and taught me the fundamental device physics. I also enjoyed working together with Ferry Prins and Alvaro Magdaleno de Benito from the Prins lab at Universidad Autonoma de Madrid. Although our international collaboration project was interrupted by the pandemic, I wish it would be resumed

when everything comes back to normal. Also, I would like to thank Team Coherence members from the Schlau-Cohen lab for having fun together playing volleyball.

I have been fortunate to have wonderful friends at MIT. Within Course X, I want to thank Moo Sun Hong, Tedrick Thomas Salim Lew, Beatrice Soh, Hongbo Zhao, Lisa Hsieh, Sam Winslow, Colin Grambow, Ki-Joo Sung, Kim Dinh, Stan Wang, Terry Gani, Yunsie Chung, Aisulu Aitbekova and Sun Jin Moon. Sharing my life with friends who understand what I am going through has always invigorated me. Outside of Course X, I would like to thank Hyungmok Son, Seong Soon Jo, Byong Ha Kang, Sunho Kim, Youngsup Song, Gene Woo Kang and Byungkyu Park for the wonderful friendship and having so much fun together. I also want to thank everyone from MIT Korean Student Association Soccer Team, for spending time together and making such good memories throughout the past 6 years. I also appreciate Prof. Peko Hosoi and Christina Chase for letting me join MIT Sports Lab, and Lukas Brink and Ferran Vidal-Codina for the wonderful collaboration and friendship. As a sports fan, it has brought me great joy to organize MIT Sports Summit, learn how science and engineering can revolutionize sports, meet pioneers in the field of sports, and become friends with fellow scientists who are passionate about sports.

Outside of MIT, I would like to thank my friends from my days in Korea: Chul Kyun Im, Young Moon Ryoo, Soonmo Kwon, Wawa Hong, Saecheol Oh, Hankyu Yoon, Jong Ju Lee, Jongwook Choi, Yongsun Lee, Yongjin Lee, and June-Hun Kim. Despite 10+ hour time difference, they have always made themselves available when I needed them. During difficult times, video chatting with them helped me forget about research and made me feel refreshed. I also want to thank Tae Keun Ane, Taehwan Kwon, Minseo Kim, and fellow FC Boston and K-Wolves teammates in Boston/Cambridge area. Playing soccer and spending time with them on weekends have been a big part of my weekly routine, which I have always looked forward to.

And I thank my family for their love and support. I think my journey as a chemical engineer started 25 years ago when my parents gave me a molecular model kit, instead of a Lego, to play with. My parents have taught me everything I know, always loved me, and supported me. As time goes by, I become more grateful for everything my parents have provided me. Also, my sister has always been on my side and I do not remember ever fighting with her even when we were kids. She has been a big part of me growing up as a person who I am. I would also like to thank my brother-in-law for his support and encouragement, and my two adorable nephews for always making me smile. I owe everything to my family.

Finally, none of this would have been possible without Nayoung Kim, my life companion and the best friend. She has filled my life with unconditional support, love, and joy. Although we live in different continents and time zones, she was always there whenever I felt lost. She has always listened to me, given me confidence, and made me believe in myself. Her love has been my source of energy to navigate through this journey, and made it possible for me to reach this point. For her, I cannot thank enough.

Again, thank you everyone, for standing by my side and supporting me throughout this journey.

Table of Contents

List of Figures

List of Tables

Chapter 1. Introduction

1.1. Importance of Colloidal Semiconductor Nanocrystals

One of the key tasks in modern engineering is to develop material systems that possess desirable properties for specific applications. Characteristics that are desired for each application widely vary, and thus designing a perfect material with all advantageous characteristics has always been a holy grail to the engineers.

Colloidal semiconductor nanocrystals are solution-processable nanomaterials that have led the development of cutting-edge energy conversion technologies in the past few decades. There has been a rapid development of a wide range of optoelectronic applications based on semiconductor nanocrystals,[1] which include photovoltaics,[2-8] light-emitting devices,[9-15] photodetectors,[8, 16-18] lasers,[8, 14, 19] flexible electronics,[20-22] and thermoelectrics.[23-25] Compared to bulk semiconductor crystals, nanocrystals provide additional merits of solution processability, which can facilitate the device fabrication process, and property tunability via engineering surface ligands,[26-28] composition,[29, 30] and size.[1, 31, 32] In particular, having those additional tuning handles opens up the window for independently optimizing various material properties — including bandgap,[1, 31, 32] surface properties,[33, 34] stability,[35-37] charge carrier dynamics[38-40] — which can eventually lead to the development of the material with ideal properties. Thus, it is of great importance to study novel semiconductor nanocrystals and precisely modulate their properties for the design of next-generation optoelectronic devices.

1.2. Semiconductor Nanocrystal Structure and Physics

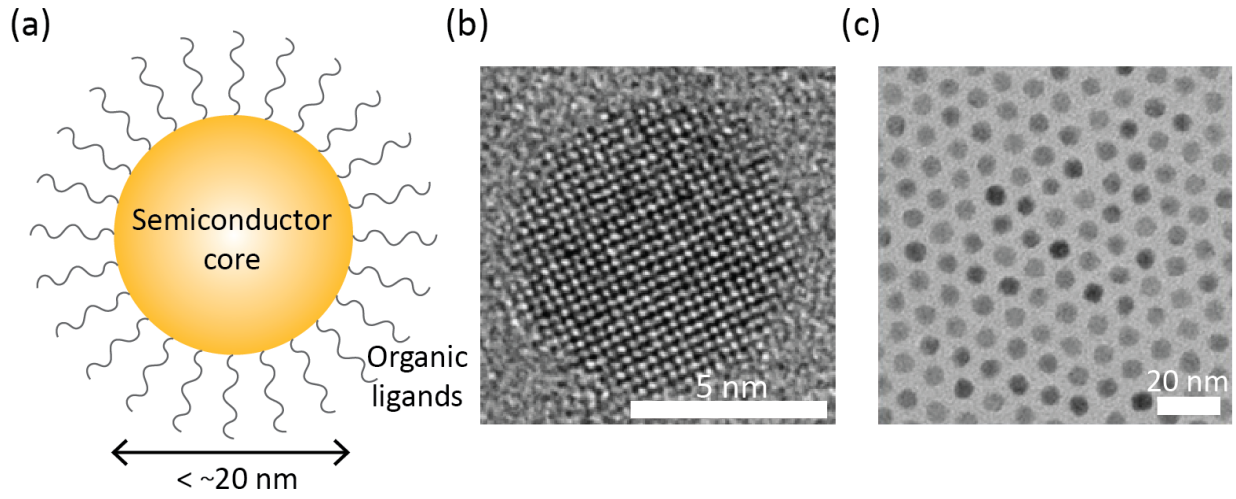

Figure 1.1. Structure of colloidal semiconductor nanocrystals. (a) Schematic illustration of a semiconductor nanocrystal. (b) High-resolution transmission electron microscopy (TEM) image of a single semiconductor (PbS) nanocrystal. (c) TEM image of semiconductor nanocrystal array. Panel b and c are reprinted from ref. 41. Copyright 2014 American Chemical Society. Further permissions related to the material excerpted must be directed to the American Chemical Society.

Colloidal semiconductor nanocrystals are colloidally-stable nanometer-sized semiconductor crystallites (Figure 1.1a). The size of their semiconductor cores is comparable to the characteristic distance between an electron and a hole inside the semiconductor (Bohr radius), which is typically a few nanometers.[42, 43] Organic ligands surrounding the semiconductor core provides colloidal stability in organic solvents and also electronically isolates the semiconductor core from the surrounding environments. Depending on the number of dimensions that are comparable to Bohr radius, semiconductor core can be classified into various shapes including 0D quantum dots (QDs: all three dimensions comparable to Bohr radius), 1D nanorods (NRs: two dimensions comparable to Bohr radius), and 2D nanoplatelets (NPLs: one dimensions comparable to Bohr radius). Transmission electron microscopy (TEM) is a widely used technique to observe nanocrystals and study their structures. Even a single nanocrystal with lattice fringes can be observed using high-resolution transmission electron microscopy (Figure 1.1b).[41] However, contrast of nanocrystal cores are usually higher than that of organic ligands and it is challenging to directly observe surface-passivating ligands in TEM images. Nonetheless, even though they may not be directly visible in TEM images, the presence of organic ligands results in the visible separation between nanocrystals (Figure 1.1c).[41]

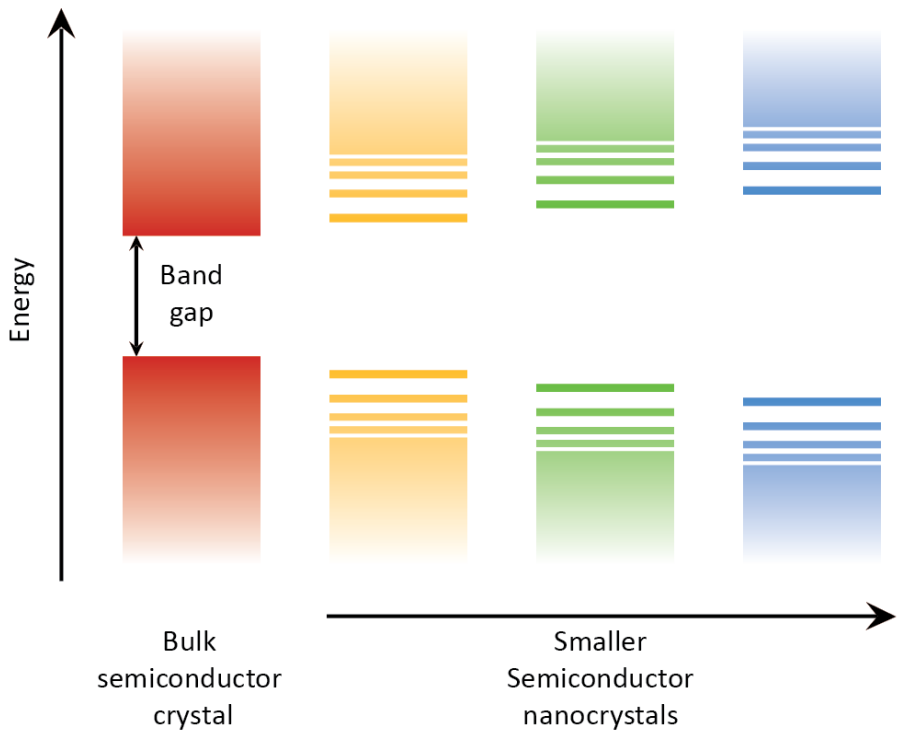

Figure 1.2. Schematic showing quantum-confinement effect of nanocrystals.

When an electron and hole pair, which is called an exciton, in a nanocrystal is squeezed into a dimension that is comparable to the characteristic length scale of an electron and hole pair, due to the small size of the nanocrystal, bandgap of the material becomes dependent on the size of nanocrystals. It is a quantum mechanical phenomenon called quantum confinement effect (Figure 1.2). As nanocrystals get smaller, energy levels in the nanocrystal become more quantized and the bandgap gets larger compared to the bandgap of bulk semiconductor crystal. Intrinsic bandgap of bulk semiconductors varies with composition,[29, 30] and this size-dependency of the energy levels provides another handle to tune the bandgap of nanocrystals. As a simple approximation, change in the bandgap of nanocrystals due to quantum confinement effect can be estimated using the following particle-in-a-box model,[1, 31]

$$E_g(r) = E_g^{bulk} + \frac{h^2}{8m_{eh}r^2}$$

where E_g is the bandgap, h is the Planck constant, m_{eh} is the effective mass of the electron and hole, and r is the characteristic length of the nanocrystal (e.g., radius of 0D quantum dots or thickness of 2D nanoplatelets).

Figure 1.3. Colloidal solutions of semiconductor (CdSe) nanocrystals under ultraviolet illumination exhibiting size-dependent bandgap tunability. Reprinted from ref. 44. Copyright 2016 Nature Publishing Group.

Figure 1.3 shows the emission from semiconductor nanocrystals of the same composition (CdSe) with different sizes under ultraviolet illumination.[44] It beautifully demonstrates the tunability of the bandgap throughout the visible range by only changing the size of the crystal without any change in composition. Being able to decouple semiconductor composition from the bandgap of the material is a huge advantage in designing novel nanomaterials which are crucial building blocks of future optoelectronic devices.

One of the most commonly used method for the synthesis of semiconductor nanocrystals is colloidal synthesis. It typically involves dissolving the precursor compounds in organic solvents with the aid of surfactants, and supersaturating the solution which triggers the nucleation and growth of nanocrystals.[31] Widely used techniques to induce supersaturation of the solution include rapid injection of other precursor compounds and initiating the change in the solubility of precursor compounds by varying the temperature or polarity of the system (e.g. injecting solvents with different polarity).[26, 31] Organic ligand species, which are usually long hydrocarbon chains with functional groups that can bind to the surface of semiconductor core, play crucial roles in colloidal synthesis of nanocrystals. By passivating to the surface of nanocrystals, they not only provide the colloidal stability, but also confine the growth of the crystal.[32]

1.3. Two-Dimensional Semiconductor Nanoplatelets

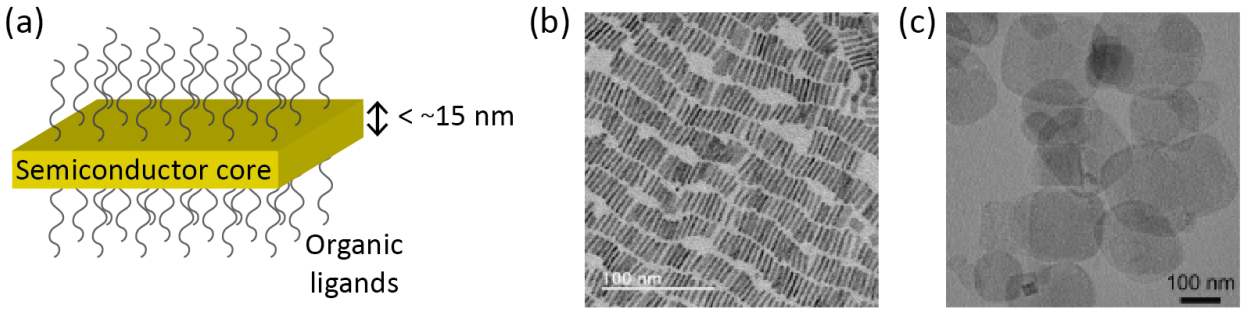

Figure 1.4. Structure of colloidal semiconductor nanoplatelets. (a) Schematic illustration of a semiconductor nanoplatelet. (b) TEM image of stacked semiconductor (CdSe) nanoplatelets with edge-up configuration on a substrate. (c) TEM image of randomly-overlapping semiconductor (lead halide perovskite) nanoplatelets with face-down configuration on a substrate. Panel b is reprinted from ref. 45. Copyright 2017 American Chemical Society. Panel c is reprinted from ref. 46. Copyright 2016 American Chemical Society. Further permissions related to the material excerpted must be directed to the American Chemical Society.

Colloidal semiconductor nanoplatelets are two-dimensional (2D) semiconductor with only one dimension being comparable to the Bohr radius of the material (Figure 1.4a). Like all nanocrystals with different shapes, surface-bound organic ligands provide colloidal stability, while also confining the growth of the crystal. Since nanoplatelets are highly confined in one dimension (thickness), its bandgap is primarily determined by the thickness, while the effect of lateral dimensions being negligible unless they become comparable to the Bohr radius.[47, 48] Due to the two-dimensional shape, nanoplatelets have been reported to undergo preferential face-to-face stacking self-assembly (Figure 1.4b),[45, 49] and when the lateral dimension is large, they have been observed to lie flat on the substrate with face-down configuration (Figure 1.4c).[46, 50]

Among nanocrystals of different shapes, 2D nanoplatelets possess several characteristics that can be highly valuable to a wide range of optoelectronic applications. For 0D quantum dots, it is challenging to synthesize nanocrystals with each dimension smaller than the Bohr radius and they are weakly confined in many cases.[51] On the other hand, it is relatively easy to prepare 2D nanoplatelets with the confined dimension smaller than the Bohr radius,[49, 52] which results in stronger confinement of excitons. Strong confinement of excitons, which is accompanied by large exciton binding energy,[53] facilitates the recombination of electrons and holes which can increase the luminescence efficiency[31, 54] and be utilized to build more efficient display devices. Furthermore, unlike 0D quantum dots synthesis where it is challenging to minimize polydispersity of nanocrystals,[41, 55-57] synthesizing highly monodisperse 2D nanoplatelets has been widely

reported.[52, 58-60] Monodisperse nanocrystals can make clear and wide color-gamut display devices. It has also been reported that strong confinement maximizes the interaction between the carriers and photoactive dopants,[61, 62] which enables the modulation of carrier dynamics. Lastly, due to the anisotropic shape of the nanoplatelets, transition dipole moments are preferentially oriented in the direction parallel to the surface of nanoplatelets.[45, 63-65] Thus, by stacking nanoplatelets on the substrate with face-down configuration, this thin film of nanoplatelets can be engineered to preferentially absorb and emit light in the direction perpendicular to the substrate. For light-emitting applications, this directional emission can hugely boost the outcoupling efficiency.[63, 64]

1.4. Metal Halide Perovskites

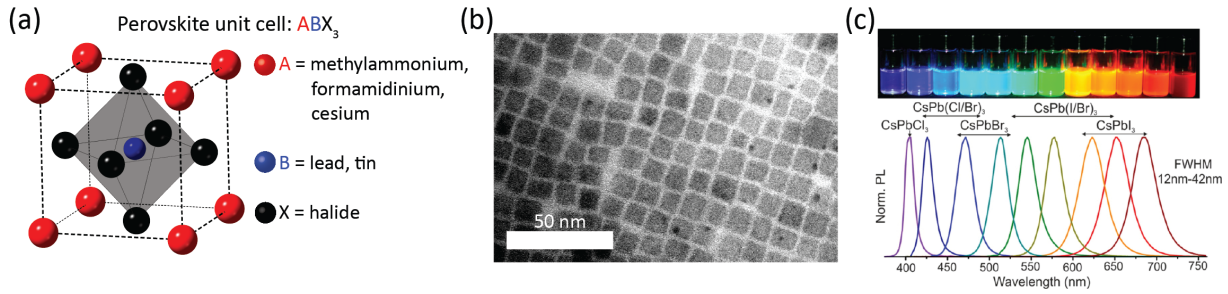

Figure 1.5. Structure of metal halide perovskites. (a) Schematic illustration of a metal halide perovskite unit cell. (b) TEM image of lead halide perovskite ($CsPbBr_3$) nanocrystals. (c) Bandgap tunability of lead halide perovskite nanocrystals with size and halide composition. Panel c is reprinted from ref. 66. Copyright 2015 American Chemical Society. Further permissions related to the material excerpted must be directed to the American Chemical Society.

Metal halide perovskites (Figure 1.5a), especially lead halide perovskites, have recently emerged as a highly promising semiconductor material platform. Rapid development of perovskite solar cells[67-75] at an unprecedented rate in the last decade effectively demonstrates exciting properties of those materials including long carrier diffusion length,[76-79] strong absorption and compositional tunability[70, 71, 80] which are highly beneficial to a wide range of optoelectronic applications. In particular, defect tolerance[81, 82] and soft ionic nature of the lattice[82-85] makes lead halide perovskites fundamentally different from other semiconductors. Unlike conventional semiconductors such as CdSe whereas nonbonding states reside inside the bandgap and act as deep traps, nonbonding states in lead halide perovskites reside either inside the bandgap or close to the band edge and do not act as deep traps.[81] This is because only antibonding states participate in the lead halide perovskite bandgap formation, while both bonding and antibonding states participate in the bandgap formation in the case of conventional semiconductors.[81] Furthermore, soft ionic nature of lead halide perovskite lattice results in the effective formation of polarons that can protect charge carriers.[84]

When prepared in the form of nanocrystals (Figure 1.5b),[66, 86, 87] lead halide perovskites exhibit even more exciting properties. Due to quantum- and dielectric-confinement, perovskite nanocrystals exhibit large exciton binding energy,[86, 88] which facilitates the recombination of electrons and holes. Similar to conventional nanocrystals, they also show size-dependent tunability.[66, 86, 87] Their bandgaps can also be tuned by simply varying the stoichiometry of halide anions (Figure 1.5c),[66, 89] which is another effective handle to modulate the nanocrystal bandgap. Additionally, perovskite nanocrystals have been reported to demonstrate bright and narrow

emission without any inorganic shells,[66, 90, 91] while most of the conventional semiconductor nanocrystals require the passivation of the semiconductor core with an inorganic shells to minimize the effect of surface traps and achieve efficient emission.[29] Since its first report in 2015,[66] incorporation of lead halide perovskite nanocrystals in optoelectronic devices — including solar cells,[75, 92, 93] light-emitting diodes (LEDs),[93-96] photodetectors,[18, 93, 97, 98] and lasers[95, 98, 99] — has been one of more active research areas in the wider field of semiconductors.

Another advantage lead halide perovskite nanocrystals has over conventional semiconductors is the potential for low-cost large-scale synthesis.[100] Although synthetic techniques are relatively well-established for various types of conventional nanocrystals,[26, 41, 101-105] their colloidal synthesis typically requires high reaction temperature reaching up to 300 ºC[31, 106] and are usually carried out in small solution volumes less than a few hundred microliters.[41, 105, 107] Despite ongoing efforts on developing more commercially viable synthetic protocols by implementing non-extreme reaction conditions,[108-111] facilitating continuous flow synthesis,[112, 113] or enabling larger scale synthesis,[114-116] it is still largely limited by the fact that usually higher-quality nanocrystals are obtained under extreme reaction conditions and those commercially viable protocols are not yet well-established. On the other hand, high-quality lead halide perovskites have been reported to be easily synthesizable at room-temperature (or at low-temperature)[82, 117] which makes it easy to be incorporated into continuous flow reactors[118-120] or scaled-up.[121-123] Facile room-temperature synthesis of perovskites is often ascribed to the small enthalpy of formation and low energy barrier.[124-128] However, this ease of synthesis is a double-edged sword. Being synthesized easily means that they can also be destroyed easily. Lead halide perovskites, including both bulk crystals and nanocrystals, seriously suffer from inferior stability[129-136] and significant enhancement of the material stability is needed before the commercialization of perovskite-based devices becomes viable.

1.5. Lead Halide Perovskite Nanoplatelets

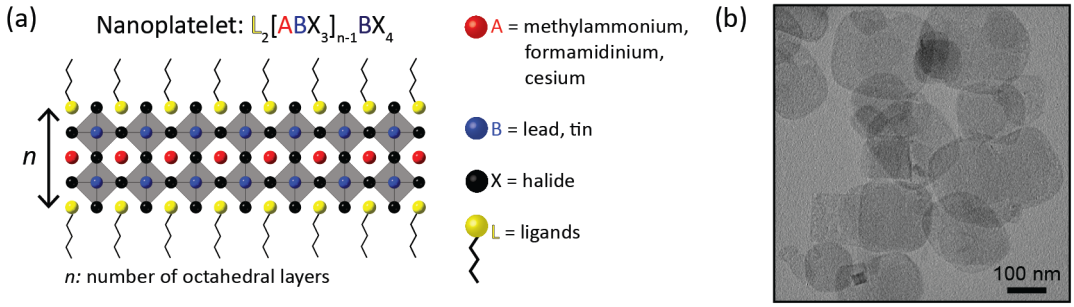

Figure 1.6. Structure of colloidal perovskite nanoplatelets. (a) Schematic illustration of a perovskite nanoplatelet. (b) TEM image of a single semiconductor (PbS) nanocrystal. (c) TEM image of randomly-overlapping perovskite ($n = 2$ lead bromide) nanoplatelets. Panel b is reprinted from ref. 46. Copyright 2016 American Chemical Society. Further permissions related to the material excerpted must be directed to the American Chemical Society.

Colloidal lead halide perovskite nanoplatelets are two-dimensional nanocrystals of lead halide perovskites (Figure 1.6). As Figure 1.6a shows, '*n*' is used to refer to the number of $[BX_6]^{4-}$ octahedral layers in the direction of thickness (e.g., $n = 1$, $n = 2$, etc.), which is a widely-used convention to indicate the thickness of the nanoplatelets. Perovskite nanoplatelets share general properties of perovskite nanocrystals summarized in the previous section. They are only a few unit cells thick and exhibit strong quantum- and dielectric-confinement that induce significant blueshift of the bandgap compared to the bulk crystals or most of the nanocrystals with other shapes,[46, 66, 137] as well as large enhancement of exciton binding energy.[86, 138] Unless the lateral dimensions of nanoplatelets are comparable to Bohr radius, bandgap of perovskite nanoplatelets are primarily determined by the thickness.[138] Additionally, they can be synthesized with high monodispersity,[36, 46, 139-149] and this thickness homogeneity enables color-pure emission from those nanoplatelets which is highly beneficial for light-emitting applications.[46, 140, 150] Moreover, it has been reported that the presence of organic ligands on the surface enhances the stability of two-dimensional perovskites.[151, 152]

However, considering the relatively short history of perovskite nanoplatelets which spans less than a decade,[139, 140, 153, 154] there still exists a large room for improvements including the advancements of synthetic capabilities, deeper understanding of material characteristics, and further expansion of material functionalities. This thesis primarily focuses on addressing those topics. More historical backgrounds and in-depth discussions on the properties of perovskite nanoplatelets will be provided in the following chapters in relation to the motivation of projects.

1.6. Thesis Overview

The overarching goal of this thesis is to develop a robust protocol for the synthesis of colloidal lead halide perovskite nanoplatelets and design their properties. I believe that advancing the synthetic technique and manipulating important material characteristics such as stability and exciton dynamics will be crucial for the ultimate utilization and commercialization of perovskite nanoplatelets in next-generation devices.

Chapter 2 focuses on the synthesis of colloidal perovskite nanoplatelets. History and the development of colloidal perovskite nanoplatelets are reviewed and facile room-temperature synthesis of perovskite nanoplatelets is displayed. In addition, fascinating tunability of the nanoplatelet bandgap and surface-passivating ligands are demonstrated.

Chapter 3 systematically investigates the photostability of perovskite nanoplatelets. After categorizing the two aspects of nanoplatelet photoinstability, intrinsic and extrinsic factors that primarily affect nanoplatelet stability are identified and their effects are elucidated. Based on those knowledge, effective stabilization strategies are demonstrated.

Chapter 4 demonstrates the synthesis of manganese(Mn^{2+})-doped colloidal perovskite nanoplatelets and elucidates the dynamics between excitons in the band edge and those in Mn^{2+} dopant atomic states. Mn-doped perovskite nanoplatelets exhibit excitation power-dependent photoluminescence intensity and quantum efficiency, and it is demonstrated that exciton-exciton annihilation, not the saturation of long-lived dopant states, is responsible for the observed power dependence. Lastly, effects of nanoplatelet composition on the exciton dynamics is discussed.

In Chapter 5, the potential impact of those work and future research directions are briefly discussed.

Overall, this thesis aims to advance the understanding of how colloidal perovskite nanoplatelets can be synthesized and their properties can be designed. I believe this thesis can serve as a guide for the fabrication of next-generation devices based on colloidal perovskite nanoplatelets.

Chapter 2. Synthesis of Two-Dimensional Colloidal Perovskite Nanoplatelets

The basis of this chapter has been published as:

Ha, S.K.; Tisdale, W.A. "Facile Synthesis of Colloidal Lead Halide Perovskite Nanoplatelets via Ligand-Assisted Reprecipitation" ***J. Vis. Exp.*** 152, e60114 (2019)

Dey, A.; Ye, J.; De, A.; Debroye, E.; Ha, S.K.; Bladt, E.; Kshirsagar, A.S.; Wang, Z.; Yin. J.; Wang, Y.; Quan, L.N.; Yan, F.; Gao, M.; Li, X.; Shamsi, J.; Debnath, T. Cao, M.; Scheel, M.A.; Kumar, S.; Steele, J.A.; Gerhard, M.; Chouhan, L.; Xu, K.; Wu, X.-g.; Li, Y.; Zhang, Y.; Dutta, A.; Han, C.; Vincon, I.; Rogach, A.L.; Nag, A.; Samanta, A.; Korgel, B.A.; Shih, C.-J.; Gamelin, D.R.; Son, D.H.; Zeng, H.; Zhong, H.; Sun, H.; Demir, H.V.; Scheblykin, I.G.; Mora-Seró, I.; Stolarczyk, J.K.; Zhang, J.Z.; Feldmann, J.; Hofkens, J.; Luther, J.M.; Pérez-Prieto, J.; Li, L.; Manna, L.; Bodnarchuk, M.I.; Kovalenko, M.V.; Roeffaers, M.B.J.; Pradhan, N.; Mohammed, O.F.; Bakr, O.M.; Yang, P.; Müller-Buschbaum, P.; Kamat, P.V.; Bao, Q.; Zhang, Q.; Krahne, R.; Galian, R.E.; Stranks, S.D.; Bals, S.; Biju, V.; Tisdale, W.A.; Yan, Y.; Hoye, R.L.Z.; Polavarapu, L. "State of the Art and Prospects in Halide Perovskite Nanocrystals" ***ACS Nano***, ASAP (2021)

2.1. Overview: Development of Colloidal Perovskite Nanoplatelet Synthesis

2.1.1. Origins of Perovskite Nanoplatelets

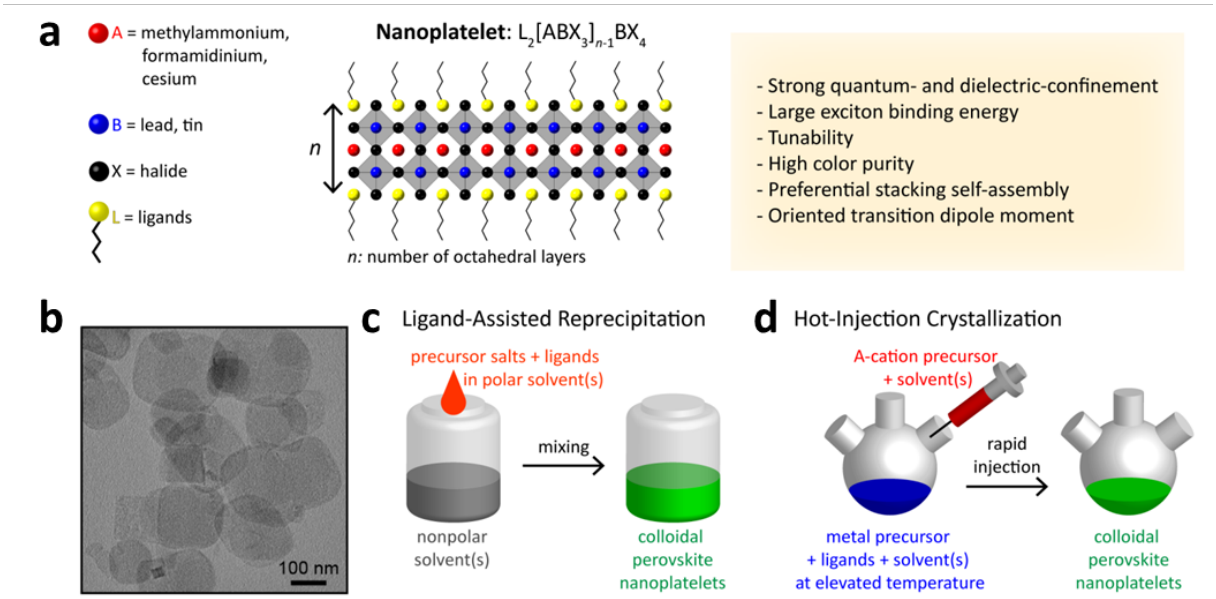

Figure 2.1. Structure of colloidal perovskite nanoplatelets and synthetic approaches. (a) Perovskite nanoplatelet structure and its unique properties. (b) Transmission Electron Microscopy (TEM) image of nanoplatelets. Reprinted with permission from Ref. 46. Copyright 2016 American Chemical Society. Further permissions related to the material excerpted must be directed to the American Chemical Society. (c) Schematic illustration of ligand-assisted reprecipitation method. (d) Schematic illustration of hot-injection crystallization method.

Two-dimensional (2D) metal halide perovskite nanoplatelets trace their origin to the synthesis of Ruddlesden-Popper (RP) phase layered perovskite crystals. In the 1990s, it was discovered that substituting the usual small A-site cations (e.g. methylammonium (MA), formamidinium (FA), cesium (Cs)) for larger organic cations (e.g. butylammonium) could induce the self-organization into layered structures.[155-161] Those layered perovskite crystals consist of alternating inorganic layers of lead halide octahedra and organic cations; the inorganic metal halide layer primarily determines the optoelectronic properties and the large organic cation layer electronically isolates the inorganic layers. Because of quantum-confinement effects, layered perovskites exhibit drastically different properties compared to the bulk 3D phase.[162] Also, layered perovskites showed enhanced stability compared to 3D counterparts due to a negative enthalpy of formation[124-

[126] as well as the presence of organic spacer layers that protects inorganic layers from external factors such as oxygen and moisture.[151]

Around 2015, multiple groups reported the synthesis of colloidal perovskite nanoplatelets (NPLs)[139, 140, 153, 154] – 2D perovskite crystals much like their RP predecessors, but dispersed in solution. Colloidal perovskite NPLs are generally characterized by the chemical formula of $L_2[ABX_3]_{n-1}BX_4$ (Figure 2.1a and 2.1b) where *n* indicates the number of inorganic metal halide octahedral layers in thickness. Thickness of NPLs are confined to a few unit cells and NPLs can tolerate lateral dimension dispersity as long as thickness homogeneity is ensured.[138] Surface ligands act as surfactants, entropically stabilizing the 2D crystals in solution, but their role in 2D nanocrystal formation is debated.[163] Since layered RP perovskites can be thought as a crystal of stacked NPLs with electronically decoupled inorganic layers, there are many parallels between layered perovskites and perovskite NPLs. They seem to be tunable over the same range and composition with identical bandgap and optical properties,[46, 138, 140, 162, 164, 165] which implies that previous studies on layered perovskites can also shed light on the properties of colloidal perovskite NPLs.

Colloidal perovskite NPLs were first identified as a side product of $MAPbBr_3$ nanocrystal synthesis,[154] but very quickly the ability to precisely control thickness was reported.[139, 140, 146, 153] Following these initial reports, subsequent efforts focused on developing refined synthetic protocols for NPLs with well-controlled thicknesses and improved material properties. For instance, the color of emission can be tuned by varying thickness and composition.[46, 139-141, 150, 153, 166] Also, reports on the tunability of surface-capping ligands, ranging from short ligands for optimal charge transport behavior to long and functionalized ligands for enhanced stability, have highlighted the possibility of optimizing surface properties of NPLs for specific applications.[36, 166, 167] It has also been reported that the lateral dimension of NPLs, which may affect electronic transport in NPL optoelectronic devices, can be tuned from tens of nanometers[139-141, 143, 146, 168, 169] to several micrometers[46, 138, 145, 149] without loss of quantum confinement in the vertical direction.

2.1.2. Unique Properties of Nanoplatelets

2D nanoplatelets possess unique characteristics specific to their 2D shape (Figure 2.1a). The exciton Bohr radius of lead halide perovskite materials has been reported to be ~3 nm or larger,

depending on composition.[66, 138, 139, 153, 160] It is synthetically challenging to prepare 0D nanocrystals with such small dimensions, however, perovskite NPLs as thin as 0.6 nm in thickness[46, 147, 167, 170] exhibiting strong quantum- and dielectric-confinement can be easily realized. This strong confinement induces excitonic absorption and emission features to be blue-shifted from those of bulk phase by up to 0.7 eV,[46, 137] which enable the synthesis of bluer light-emitting nanocrystals. Spatial confinement of excitons in 2D structures also yields large exciton binding energies reaching up to several hundred meV[86, 137, 160, 161] which can facilitate efficient recombination of excitons. Moreover, monodisperse NPLs exhibit superior emission color purity due to atomically precise thickness homogeneity. Achieving monodispersity is of great importance for NPLs since bandgaps of strongly-confined NPLs show significantly larger shifts when thickness changes[46, 138, 150] compared to other weakly confined nanocrystals.[66, 171] Nonetheless, monodisperse nanoplatelets have been widely demonstrated.[36, 46, 139-149]

A 2D structure is ideal for integration into optoelectronic devices. A key advantage of 2D NPLs is the tendency for the transition dipole moment to preferentially orient within the 2D plane,[63, 172] which is advantageous for optical coupling. Additionally, NPLs exhibit face-to-face stacking[140, 143, 144] and preferential face-down assembly on a given substrate.[35, 46, 149, 167] This tendency – combined with transition dipole anisotropy – leads to preferential emission in the out-of-plane direction.[63] Moreover, large lateral dimensions of NPLs[46, 145, 149, 153] can potentially be utilized to minimize grain boundaries in-plane and lower the percolation threshold for charge transport.[173]

2.1.3. Development of Synthetic Protocols

Numerous synthetic approaches to perovskite NPLs have been developed. In this Chapter, I will first discuss the two most widely used techniques – ligand-assisted reprecipitation (Figure 2.1c) and hot-injection crystallization (Figure 2.1d) – and then introduce other synthetic approaches. The ligand-assisted reprecipitation (LARP) method usually consists of dissolving perovskite NPL precursor salts in relatively polar solvent(s) (e.g., N,N-Dimethylformamide (DMF), Dimethyl sulfoxide (DMSO)) and then mixing it with less polar solvent(s) (e.g., Toluene, hexane) to induce crystallization at room-temperature. In 2015, Sichert et al. published the first synthesis of thickness-controlled $MAPbBr_3$ NPLs via LARP (Figure 2.2a).[153] They dissolved NPL precursors (MABr, $PbBr_2$ and OABr) in DMF and NPLs were crystallized upon mixing it with excess toluene. Precise tuning of NPL thickness was achieved by varying methylammonium-to-

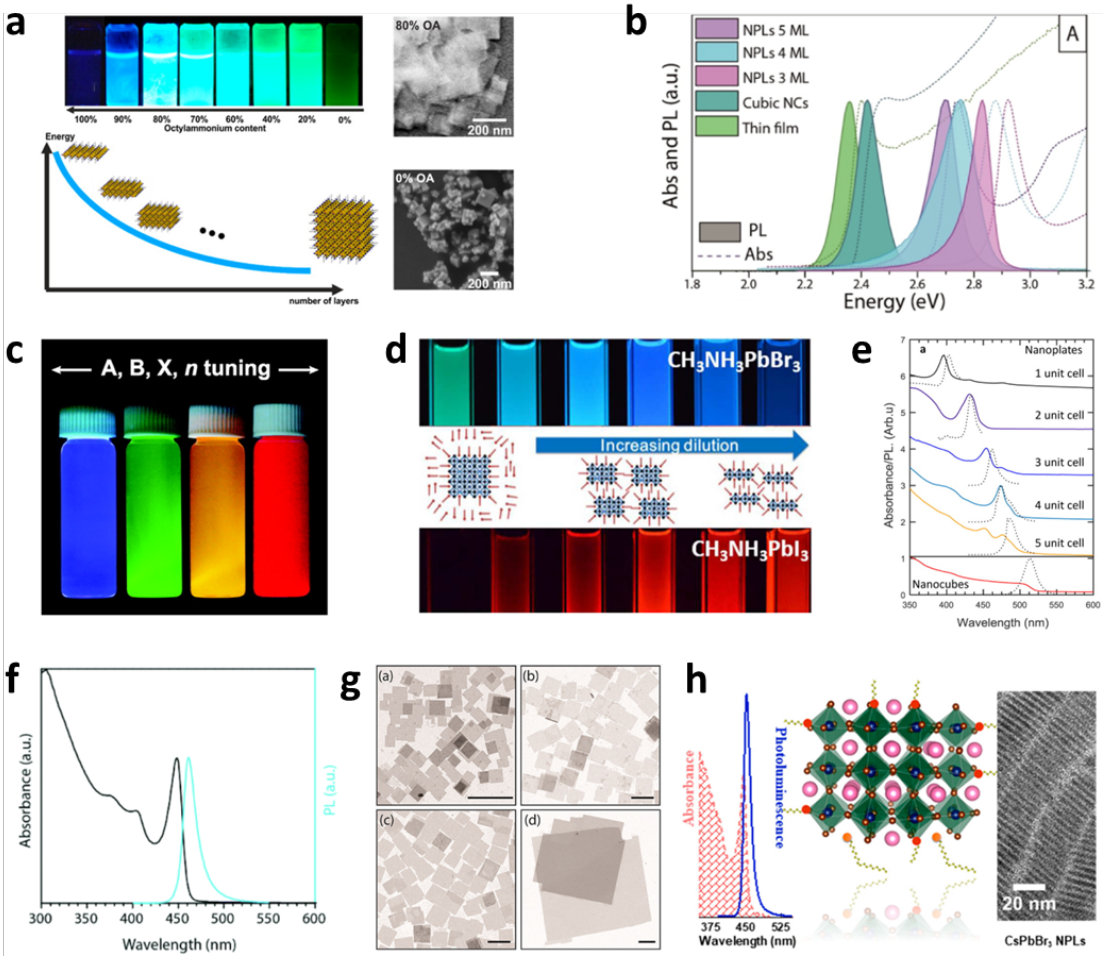

Figure 2.2. Advancements of colloidal perovskite nanoplatelet synthesis. (a) Synthesis of thickness-controlled $MAPbBr_3$ nanoplatelets via ligand-assisted reprecipitation (LARP). (b) Synthesis of $CsPbBr_3$ nanoplatelets via LARP. (c) Thickness and compositional tunability of nanoplatelets via LARP. (d) Dilution-induced nanoplatelet formation via LARP. (e) Thickness-controlled $CsPbBr_3$ nanoplatelet synthesis via hot-injection crystallization (HI). (f) $n = 3$ $MAPbBr_3$ NPL synthesis via HI. (g) NPL lateral dimension control through HI synthesis. (h) Synthesis of hexylphosphonate-capped NPLs with enhanced stability via heat-up approach. Reprinted with permission from (a) Ref. 153. Copyright 2015 American Chemical Society (b) Ref. 139. Copyright 2016 American Chemical Society (c) Ref. 46. Copyright 2016 American Chemical Society. (d) Ref. 174. Copyright 2016 American Chemical Society (e) Ref. 140. Copyright 2015 American Chemical Society (f) Ref. 146. Copyright 2016 The Royal Society of Chemistry (g) Ref. 145. Copyright 2016 American Chemical Society. (h) Ref. 36. Copyright 2020 American Chemical Society. Further permissions related to the material excerpted must be directed to the American Chemical Society.

octylammonium ratio in precursor solution. Soon after, Akkerman et al. reported the synthesis of $n = 3 - 5$ $CsPbBr_3$ NPLs with modified LARP process where the addition of acetone into the precursor solution mixture induced destabilization of precursor complexes and induced NPL crystallization under ambient conditions (Figure 2.2b).[139] They also showed that the bandgap of

the NPLs can be continuously tuned by anion exchange reaction. Later, Weidman et al. published $n = 1$ and $n = 2$ perovskite NPLs with wide ranging composition (A = MA/FA/Cs, B = Pb/Sn, X = Cl/Br/I, ligand = butylammonium/octylammonium) via LARP by simply varying the stoichiometric ratios of precursor solutions (Figure 2.2c).[46] Tong et al. demonstrated the breakup of large $MAPbX_3$ nanocrystals synthesized via LARP into NPLs by diluting the solution which triggered osmotic swelling by solvent (Figure 2.2d).[174] In addition, Sun et al. carried out a systematic study and showed that the choosing the right combination of ligand species plays crucial role in determining the shape of the nanocrystals synthesized via LARP.[175]

In general, LARP enables facile synthesis of colloidal perovskite NPLs with easily tunable composition and ligands. Moreover, LARP can be highly cost-effective as it delivers colloidal perovskite NPLs in ambient atmosphere at room-temperature. However, thinner NPLs synthesized via LARP tend to exhibit lower photoluminescence quantum yield (PLQY)[46, 153, 167] and it is difficult to target thicker ($n >= 3$) dispersions with good thickness control.[167, 176, 177] Recent works have focused on refining the synthesis and improving material properties – expanding synthetic capability,[142, 166, 170] improving thickness selectivity,[167, 170] modulating surface properties by incorporating new ligand species,[166, 167] boosting photoluminescence quantum yield (PLQY)[142, 148, 150] and enhancing material stability.[35] Although significant advancements have been made in the past few years, there still exists an imminent need for further development.

Another widely used synthetic approach is hot-injection (HI) crystallization. The HI approach is based on the rapid injection of a precursor solution into another solution of other precursors, ligands and solvent(s) at elevated temperature. HI synthesis enables the separation of nucleation and growth of nanocrystals so that it can deliver high-quality nanocrystals.[117] Also, it does not involve any polar solvent which could potentially be detrimental to colloidal perovskites. First reports of perovskite NPL synthesis via HI protocol[140, 146] came out a few months after Protesescu et al. published the synthesis of $CsPbX_3$ quantum dots via HI.[66] Bekenstein et al. found that lowering the temperature of cesium precursor injection into lead halide precursor solution results in the formation of $n = 1 - 5$ $CsPbBr_3$ NPLs (Figure 2.2e).[140] They also demonstrated NPL bandgap tuning via halide exchange reaction. Around the same time, Vybornyi et al. reported the HI synthesis of $n = 3$ $MAPbBr_3$ NPLs (Figure 2.2f).[146] Along with the previous report from Sichert et al. on the synthesis of $MAPbBr_3$ NPLs via LARP,[153] those reports opened up the field of thickness-controlled colloidal perovskite NPL synthesis. However, it was pointed out that lateral dimensions

of perovskite NPLs synthesized via HI (10 − 100 nm)[140, 141, 146] are generally smaller than those of NPLs synthesized via LARP (100 − 1000 nm).[46, 153, 167] In response to it, Shamsi et al. showed that the lateral dimension of $CsPbBr_3$ NPLs can be increased to several microns by adjusting the ratio of shorter ligands to longer ligands in the synthetic mixture during HI synthesis (Figure 2.2g).[145] Similarly, Zhang et al. published the synthesis of micron-sized n = 2 $FAPbBr_3$ NPLs.[149] Furthermore, Pan et al. provided deeper insight into HI synthesis by identifying the key factors that control the shape of the nanocrystals in HI synthesis – reaction temperature and choice of ligands.[178]

Recent works on NPL synthesis via HI have focused on refining the synthesis of NPLs accompanied by detailed structural characterizations[141] and understanding the complex dynamics of HI reaction.[168, 179] However, HI synthesis is still highly focused on Cs-based NPLs[140, 141, 145, 168, 178, 179] and there are only a limited number of reports on organic cation-based NPLs.[146, 149] Compared to LARP-synthesized NPLs, HI-synthesized NPLs are generally smaller in lateral dimensions[140, 141, 146] and usually capped by longer ligands,[46, 140, 141, 153] which could undermine electronic transport properties. Since the HI method requires high temperature and inert atmosphere, scalability and cost-effectiveness could be greater barriers to eventual commercialization for HI than for LARP. Historically, HI-synthesized NPLs have shown higher PLQY,[139, 140] though PLQY of LARP-synthesized NPLs have recently become comparable.[142, 148, 150, 174] Thus, more efforts on further developing HI synthesis of perovskite NPLs are needed.

Apart from LARP and HI, other creative approaches to perovskite NPL synthesis have been demonstrated. Shamsi et al. showed that n = 3 $CsPbBr_3$ NPLs can be synthesized by mixing of cesium oleate solution with $PbBr_2$-ligands complex solution, adding isopropanol to initiate nucleation and then heating the solution to grow NPLs.[122] A few years later, Shamsi et al. slightly modified this heat-up method and demonstrated the synthesis of hexylphosphonate-capped NPLs (Figure 2.2h).[36] They observed that stronger binding of phosphonate ions compared to conventional alkylammonium ions to NPL surface[36, 178] greatly improved the stability of NPLs and suppressed transformation of NPLs into thicker, less-confined structures which can result in the loss of desirable optical properties.[35, 122, 134] Huang et al. reported the scalable synthesis of n = 4 $FAPbI_3$ NPLs by mixing FA-ligands complex solution with PbX_2-ligands complex solution in toluene.[143] This approach was a hybrid of HI and LARP in that it was done under ambient conditions at room temperature but no polar solvent was involved. Another interesting approach

is ultrasonication-assisted synthesis; Tong et al.[180] and Hintermayr et al.[181] reported the synthesis of perovskite NPLs by sonicating the dispersion of perovskite precursors in the presence of coordinating ligands. Lastly, Dou et al. demonstrated the direct synthesis of atomically-thin monolayer of L_2BX_4 perovskite on the substrate by dropcasting the solution of precursor salts dissolved in DMF/chlorobenzene co-solvent.[182] Even though this was not a 'colloidal nanoplatelet' synthesis, it introduces another promising route to deposit a thin layer of 2D perovskites.

2.1.4. Outstanding Questions and Future Opportunities

Although various synthetic techniques have been developed for colloidal perovskite NPLs, a complete understanding of anisotropic perovskite NPL growth is lacking. How can thin 2D structures grow from an isotropic crystal lattice and homogeneous solvent environment? An in-depth study carried out by Riedinger et al. on the formation of 2D CdSe NPLs from isotropic materials[163] provides some interesting insight. In that paper, the authors started with experimentally verifying that CdSe NPLs can be formed in isotropic environment in the absence of any molecular mesophases, and then formulated a growth model based on experimental results. General theory of nucleation and growth predicts the growth of a nanocrystal to occur through the nucleation of a new island on one of the facets; when this island reaches a critical size, expansion of the island becomes thermodynamically favorable and leads to the formation of a complete new layer to the facet. Riedinger et al. showed that when specific criteria are met – namely, 1) nanocrystal formation occurs through nucleation-limited growth, 2) initial small crystallites can adopt anisotropic 2D shapes due to the random fluctuations in the reaction mixture, and 3) thickness of this initial crystallite is smaller than the critical island size − certain combinations of volume, surface and edge formation energies of nanocrystals in the system can lead to a lower nucleation barrier for narrower facets compared to large planar facets. This lower nucleation barrier results in the faster growth on the narrower facet, which can eventually yield anisotropic 2D NPLs. Their model also predicts higher narrow-facet nucleation barrier for thicker NPLs than thinner NPLs, and it is consistent with the observations by Bekenstein et al.[140] and Pan et al.[178] that thicker perovskite NPLs were formed at higher reaction temperatures. Although Riedinger et al. studied CdSe NPL system, their theoretical model is generalizable to any isotropic materials system, including perovskite NPLs. It should also be noted that, along with reaction temperature,

previous reports listed careful choice of ligands, precise control of perovskite precursor composition and concentration of precursor solution as other key factors in the shape-controlled synthesis of perovskite NPLs.[175, 178, 179] I speculate that optimized synthetic conditions in those reports may in fact reflect precisely tuned volume, surface and edge formation energies of the nanocrystal in the system where the formation of anisotropic 2D NPLs is favored. And more recently, Burlakov and coworkers proposed a $CsPbBr_3$ NPL formation mechanism based on the competitive nucleation of an inorganic perovskite layer and an organic ligand layer.[183] Being consistent with the discussion above, their work also focused on temperature and interaction energies between constituents as primary factors that determine nucleation kinetics. Through a combination of theoretical and experimental work, they showed that, under certain conditions, narrower facets can favor crystal layer nucleation while wider facets are more effectively passivated by ligand layer formation, which can lead to anisotropic two-dimensional crystal growth. Their theoretical prediction of preferential formation of thinner NPLs at low reaction temperature was experimentally verified, and is also consistent with the observations by Bekenstein et al.[140] and Pan et al.[178] But still, this picture is far from complete and deeper studies are needed on how anisotropic NPL are formed from isotropic environments.

In addition to open questions regarding nucleation and growth, a detailed understanding of electronic structure in 2D NPLs is still lacking. Furthermore, it is unclear to what extent perovskite NPLs actually exist as isolated sheets in solution rather than small crystallites of RP phase.[184] Spontaneous stacking[144, 146] and slow precipitation of NPLs[167] in concentrated solutions have been observed which may indicate the existence of large RP phase crystallites with poor colloidal stability. Thus, systematic study on the behavior of NPLs in colloidal solution is needed for better utilization of solution processability. Lastly, continuous efforts on tackling the generic drawbacks of perovskite NPLs are needed − improving low PLQY[142, 148] and enhancing the stability.[35] Additional goals include synthesis of stable lead-free NPLs,[46] doping NPLs to expand their functionality,[185] and integrating NPLs into state-of-the-art optoelectronic devices.[150]

2.2. Project Introduction

In the past decade, fabrication of lead halide perovskites solar cells[67-72] has effectively highlighted the excellent properties of this semiconductor material, including long carrier diffusion lengths,[76-79] compositional tunability,[70, 71, 80] and low-cost synthesis.[186] In particular, the unique nature of defect tolerance[81, 82] makes lead halide perovskites fundamentally different from other semiconductors and thus highly promising for next-generation optoelectronic applications.

In addition to solar cells, lead halide perovskites have been shown to make excellent optoelectronic devices such as light-emitting diodes,[72, 90, 91, 150, 187-191] lasers,[192-194] and photodetectors.[195-197] Especially, when prepared in the form of colloidal nanocrystals,[46, 66, 138, 140, 142, 145, 146, 150, 153, 154, 198-203] lead halide perovskites may exhibit strong quantum- and dielectric-confinement, large exciton binding energy,[86, 88] and bright luminescence[90, 91] along with facile solution processability. Various reported geometries including quantum dots,[66, 198-200] nanorods,[175, 202] and nanoplatelets[46, 138, 140, 142, 145, 146, 150, 153, 154] further demonstrate the shape tunability of lead halide perovskite nanocrystals.

Among those nanocrystals, colloidal two-dimensional (2D) lead halide perovskites, or "perovskite nanoplatelets", are especially promising for light-emitting applications due to strong confinement of charge carriers, large exciton binding energy reaching up to hundreds of meV,[86] and spectrally narrow emission from thickness-pure ensembles of nanoplatelets.[140] Additionally, anisotropic emission reported for 2D perovskite nanocrystals[63] and other 2D semiconductors[45, 65] highlights the potential of maximizing outcoupling efficiency from perovskite nanoplatelet-based light-emitting devices.

Here, a protocol for the simple, universal, room-temperature synthesis of colloidal lead halide perovskite nanoplatelets (Chemical formula: $L_2[ABX_3]_{n-1}BX_4$, L: butylammonium (BA) and octylammonium (OA), A: methylammonium (MA) or formamidinium (FA), B: lead (Pb), X: bromide (Br) and iodide (I), n: number of $[BX_6]^{4-}$ octahedral layers in the direction of nanoplatelet thickness) is demonstrated via a ligand-assisted reprecipitation technique.[35, 46, 153] Perovskite nanoplatelets incorporating iodide and/or bromide halide anions, methylammonium or formamidinium organic cations, and variable organic surface ligands are demonstrated. Procedures for controlling the absorption and emission energy and the thickness purity of the colloidal dispersion are discussed.

2.3. Synthesis of Perovskite Nanoplatelets via Ligand-Assisted Reprecipitation

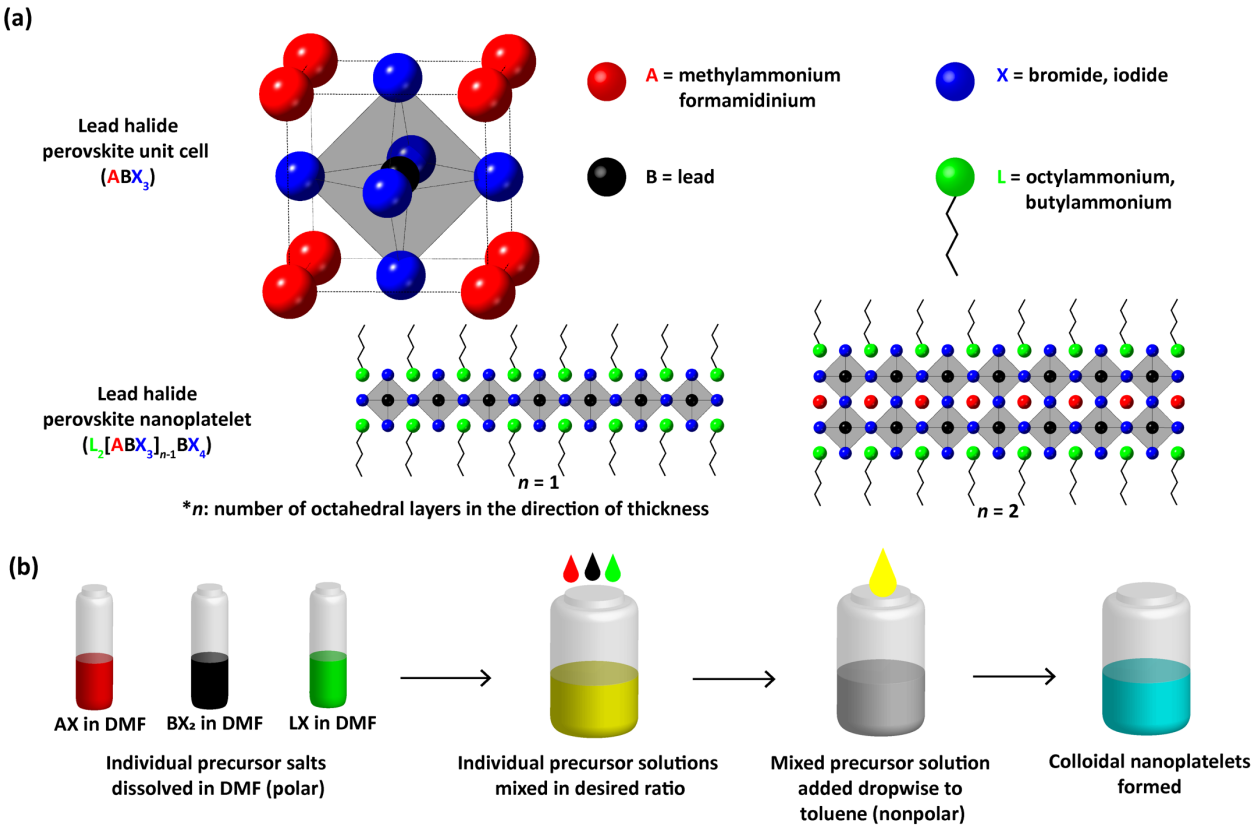

Figure 2.3. Perovskite nanoplatelet structure and synthesis procedure. (a) Illustration of perovskite unit cell and nanoplatelet structure. (b) Schematic illustration of colloidal perovskite nanoplatelet synthesis.

Using ligand-assisted reprecipitation technique, two-dimensional colloidal perovskite nanoplatelets capped by alkylammonium halide surface ligands could be synthesized as shown in Figure 2.3a. In particular, I focused on the synthesis of $n = 1$ and $n = 2$ nanoplatelets. For clarity, simpler notations of '$n = 1$ BX' and '$n = 2$ ABX' that indicate the thickness and composition of nanoplatelets will be used, instead of complex chemical formula of L_2BX_4 and $L_2[ABX_3]BX_4$, respectively. Figure 2.3b demonstrates the synthetic procedure of colloidal perovskite nanoplatelets. To briefly summarize the synthetic procedure, constituent precursor salts were dissolved in a polar solvent N,N-dimethylformamide (DMF) in specific ratios for desired thickness and composition, and then injected into toluene, which is nonpolar. Due to the abrupt change in solubility, colloidal perovskite nanoplatelets started to crystallize instantaneously. In general, any polar solvent can be used to dissolve perovskite precursor salts while any nonpolar solvent can be used to disperse colloidal nanoplatelets. However, miscibility of those nonpolar and polar solvents

is crucial for homogeneous synthesis of colloidal perovskite nanoplatelets, and thus DMF and toluene were chosen. Also, it is important to have nonpolar solvent in large excess to the added polar solvent for the crystallization of perovskite nanoplatelets to occur. Adding too much polar solvent increases the polarity of the resulting solvent mixture (i.e., DMF + toluene), which can dissolve the nanoplatelets.

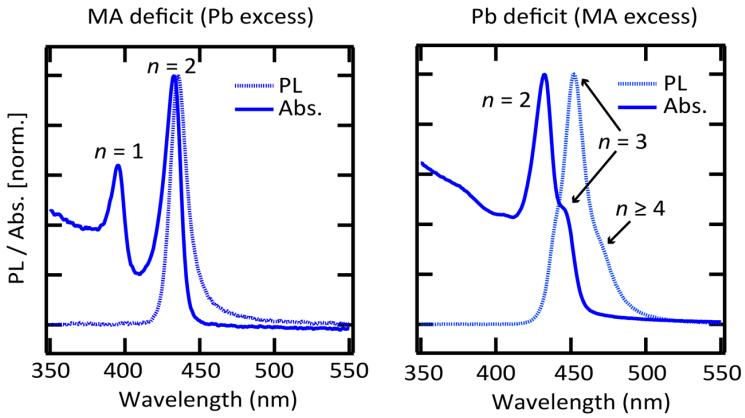

Figure 2.4. Example photoluminescence and absorption spectra of MA-deficit and Pb-deficit attempts on synthesizing n = 2 MAPbBr nanoplatelets.

When preparing the mixed precursor solution, ratios between constituent precursors primarily determined the thickness of resulting nanoplatelets. For n = 2 MAPbBr nanoplatelet synthesis, stoichiometric ratio of MABr and $PbBr_2$ in the precursor mixture is 1:2 as can be seen from the ratio of MA and Pb in the chemical formula of $L_2[MAPbBr_3]PbBr_4$. And when MA or Pb was deficient in the precursor mixture, it resulted in the formation of thinner and thicker nanoplatelets, respectively, alongside the intended n = 2 MAPbBr nanoplatelets as shown in Figure 2.4.

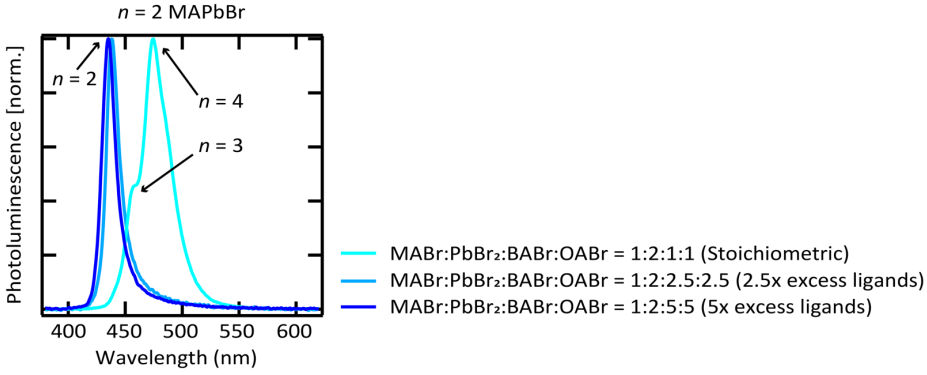

Figure 2.5. Necessity of adding excess ligands in the precursor solution for precise thickness control.

	MABr	FABr	$PbBr_2$	BABr	OABr	MAI	FAI	PbI_2	BAI	OAI
n=1 PbBr	0	0	1	1	1	0	0	0	0	0
n=2 FAPbBr	0	1	2	5	5	0	0	0	0	0
n=2 MAPbBr	1	0	2	5	5	0	0	0	0	0
n=1 PbI	0	0	0	0	0	0	0	1	1	1
n=2 FAPbI	0	0	0	0	0	0	1	2	5	5
n=2 MAPbI	0	0	0	0	0	1	0	2	5	5

Table 2.1 Formulation guidelines for perovskite nanoplatelet precursor solutions. Numbers in the table indicate the volumetric equivalents of each precursor solution (columns) that should be combined to achieve the targeted nanoplatelet (rows), according to the concentration specifications in the Methods section.

In addition, the presence of excess ligands in precursor solution was found to be crucial in ensuring the thickness homogeneity of the product. When stoichiometric amount of ligand species was present in the precursor solution mixture for $n = 2$ nanoplatelet synthesis, photoluminescence from the nanoplatelet solution was dominated by red-shifted emissions from $n = 3$ and $n = 4$ nanoplatelets as shown in Figure 2.5. However, with 2.5-times or 5-times excess amounts of ligands present in the precursor mixture, as-synthesized nanoplatelet solution showed desired deep-blue photoluminescence from $n = 2$ MAPbBr nanoplatelets without any signs of thinner or thicker nanoplatelets, which indicated particle thickness homogeneity. Based on this result, adding 5-times excess amounts of ligands, compared to the stoichiometric ratio, was chosen as the standard procedure for the synthesis of all $n = 2$ nanoplatelets with varying compositions in order to fully ensure nanoplatelet monodispersity. Since A-site cations such as Cs, MA, and FA are not necessary for $n = 1$ nanoplatelet synthesis, they were not included in $n = 1$ nanoplatelet precursor solution mixture. Since nanoplatelets cannot grow thicker without the presence of A-site cations, stoichiometric amount of ligand species in $n = 1$ nanoplatelet precursor solution was sufficient for synthesizing monodisperse n = 1 nanoplatelets. By using the same synthetic protocol with only simply varying the composition of precursor solution mixture, various perovskite nanoplatelets with varying A-site cations and halide anions could be synthesized including $n = 1$ PbBr, $n = 1$ PbI, $n = 2$ MAPbBr, $n = 2$ FAPbBr, $n = 2$ MAPbI, and $n = 2$ MAPbI. Formulation guidelines for those perovskite nanoplatelet precursor solutions are summarized in Table 2.1.

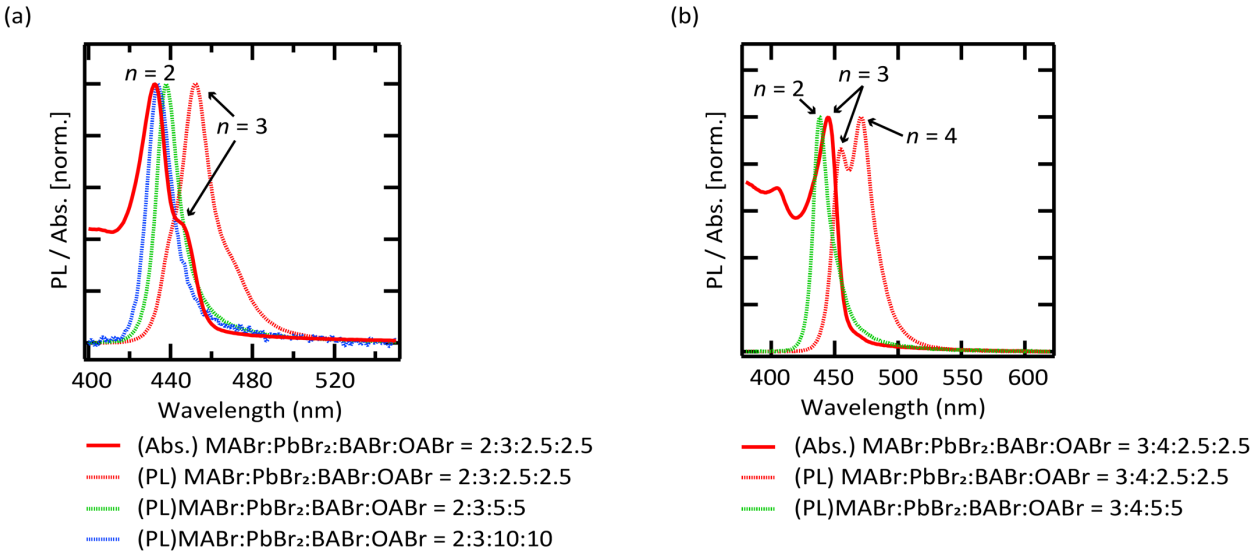

Figure 2.6. Unsuccessful attempts on the synthesis of (a) $n = 3$ and (b) $n = 4$ MAPbBr nanoplatelets.

Finally, it should be noted that only the $n = 1$ and $n = 2$ members have been synthesized with good thickness homogeneity by this method; attempts at making thicker ($n \geq 3$) nanoplatelets by varying the ratio of constituent precursor species typically yield mixed-thickness dispersions (Figure 2.6). Further studies will be needed in expanding this synthetic scheme to $n \geq 3$ nanoplatelets.

2.4. Characterization of Perovskite Nanoplatelets

2.4.1. Optical Characterization

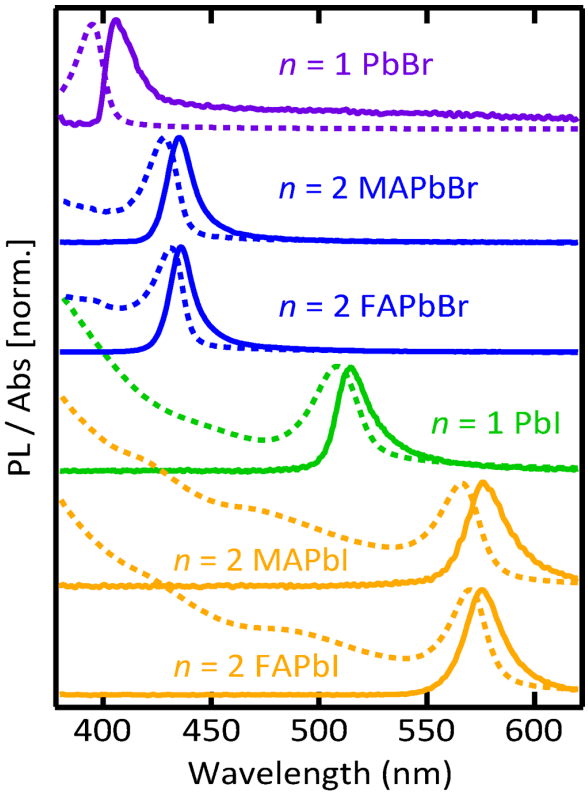

Figure 2.7. Photoluminescence and absorption spectra of colloidal perovskite nanoplatelet solutions. Bandgap of the nanoplatelets can be tuned with thickness and composition. Longpass filter (Cut-on wavelength: 400 nm) was used to filter out excitation UV light before photoluminescence spectrum collection and it could have slightly altered $n = 1$ lead bromide nanoplatelet emission spectrum.

Figure 2.7 shows the normalized photoluminescence (PL) and absorption spectra of colloidal perovskite nanoplatelet solutions, which are consistent with previous reports,[46, 142, 162, 164] demonstrating the tunability of perovskite nanoplatelets with thickness and constituent species. For all nanoplatelets, strong excitonic features in the absorption spectra and significant blue-shift of the spectra compared to bulk perovskites[138] were observed due to strong quantum- and dielectric-confinement. Changing the organic cation from methylammonium to formamidinium did not significantly affect the band gap – either for bromide or iodide nanoplatelets – in agreement with understanding of the valence electronic structure in lead halide perovskites.[81] Figure 2.8 shows the images of as-synthesized colloidal perovskite nanoplatelet solutions illuminated by UV light, where the emission of the nanoplatelets can be clearly seen along the beam path. It can be

seen that the colors of those solutions also vary because the wavelength of light being absorbed changes with thickness and composition as absorption spectra in Figure 2.7 shows.

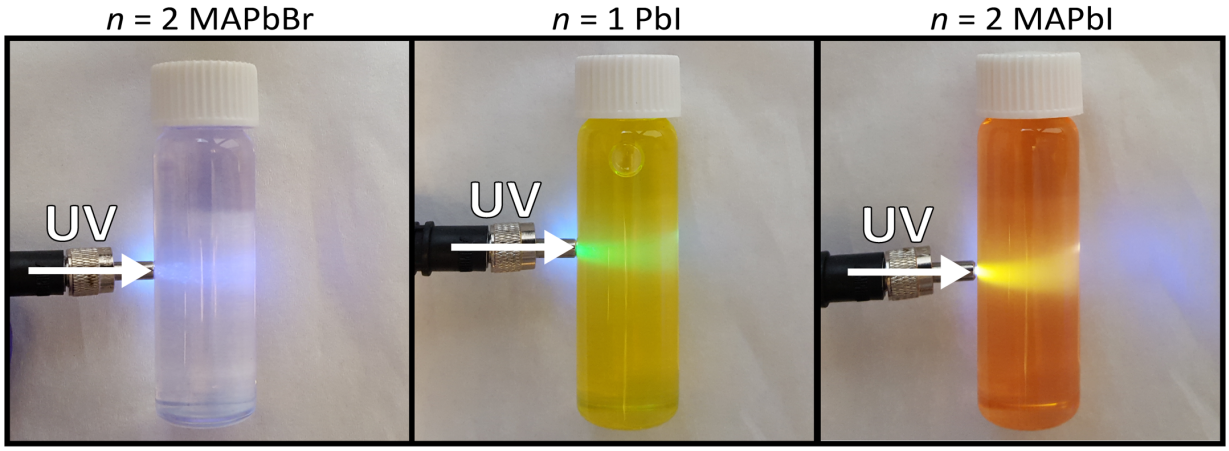

Figure 2.8. Colloidal perovskite nanoplatelet solutions illuminated by UV light. Emission from the nanoplatelets can be clearly seen along the beam path.

Nanoplatelets	PLQY
n = 1 PbBr	< 0.1 %
n = 2 MAPbBr	6.8 %
n = 2 FAPbBr	5.8 %
n = 1 PbI	0.2 %
n = 2 MAPbI	0.9 %
n = 2 FAPbI	0.7 %

Table 2.2. Photoluminescence quantum yields (PLQY) of as-synthesized colloidal perovskite nanoplatelets in toluene.

Table 2.2 summarizes the photoluminescence quantum yields (PLQYs) of those colloidal perovskite nanoplatelet solutions. For PLQY measurements, samples were excited using a 405 nm LED except *n* = 1 PbBr because 405 nm light was still slightly below the bandgap. Instead, *n* = 1 PbBr nanoplatelet solution was excited using a 365 nm LED. However, sample emission was too weak and below the detection limit of the setup. Except, *n* = 1 species, bromide nanoplatelets generally exhibited higher PLQYs than iodide nanoplatelets. However, PLQYs of perovskite nanoplatelets in solution were all lower than 10%. Significant improvement of nanoplatelet PLQYs is necessary for the utilization of nanoplatelets, and it is currently one of the more active research areas.[142, 148]

2.4.2. Structural Characterization

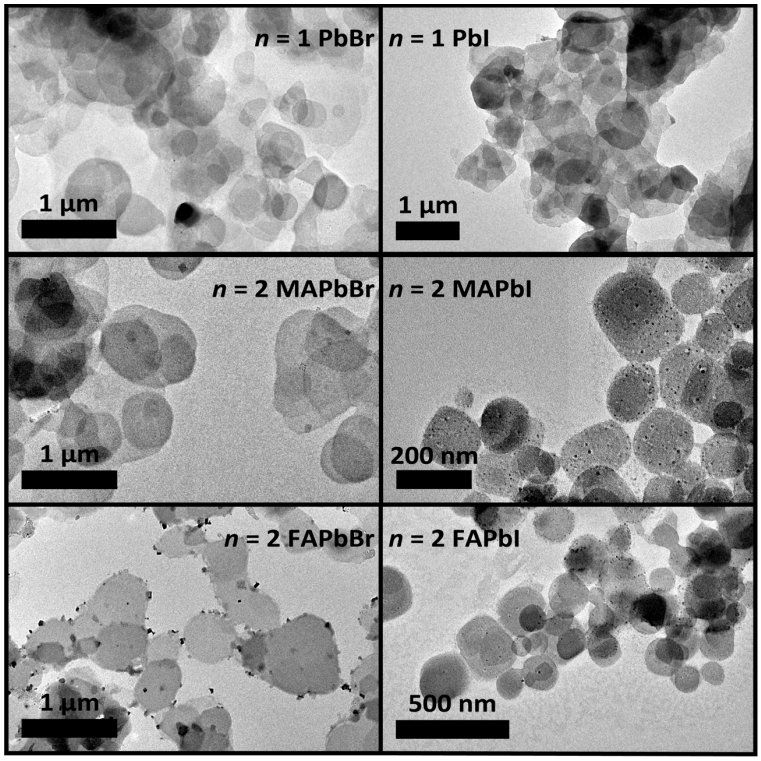

Figure 2.9. Transmission electron microscopy (TEM) images of various perovskite nanoplatelets. Images show randomly-overlapping nanoplatelets.

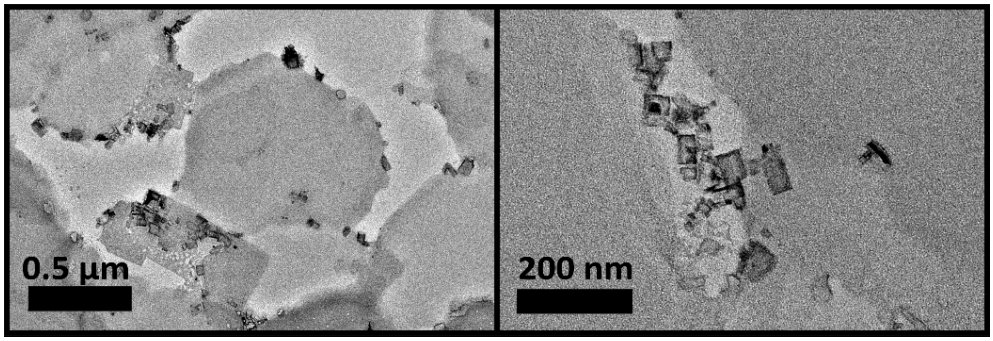

Figure 2.10. Transmission electron microscopy (TEM) images of n = 2 FAPbBr nanoplatelets.

The two-dimensional structure of the perovskite nanoplatelets was confirmed by transmission electron microscopy (TEM) and X-ray diffraction (XRD). In Figure 2.9, TEM images show partially overlapping two-dimensional perovskite nanoplatelets, with individual lateral dimensions ranging from a few hundred nanometers to a micrometer. The image contrast and random configuration of nanoplatelets on the TEM grid suggests that they are dispersed in solution as

individual sheets – rather than stacked lamellar crystals. Small, dark spherical dots appeared upon electron beam irradiation as observed in Figure 2.9, especially in iodide nanoplatelets, and they are believed to be metallic Pb as previously reported.[139, 153] And smaller structures in $n = 2$ FAPbBr TEM image is believed to be smaller nanoplatelets, as TEM images with higher magnifications in Figure 2.10 shows.

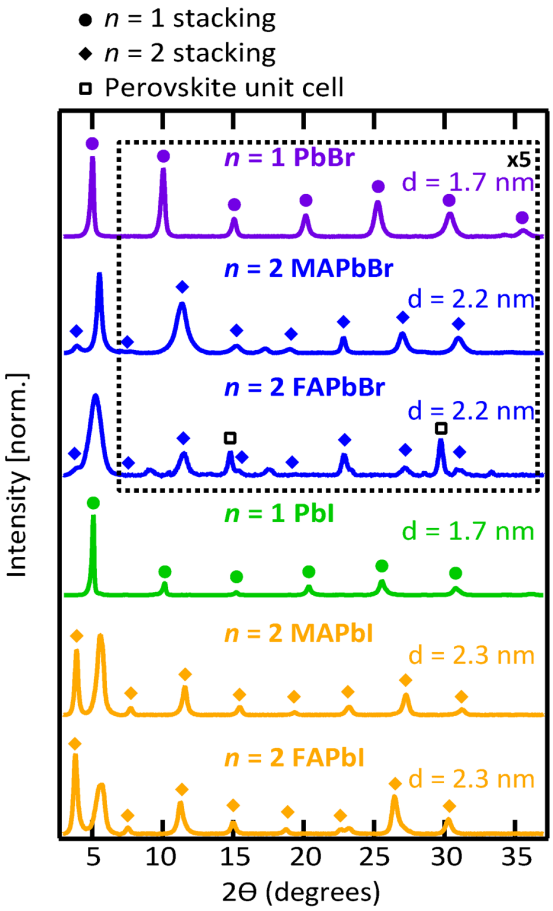

Figure 2.11. X-ray diffraction (XRD) patterns and d-spacings of perovskite nanoplatelets. XRD patterns are dominated by nanoplatelet stacking peaks which confirm the two-dimensional nature of the nanoplatelets and their face-to-face self-assembly in dropcast films.

Due to the large lateral dimensions of perovskite nanoplatelets, they preferentially lay flat on top of each other when cast into a film, and periodic stacking peaks dominated the XRD pattern as shown in Figure 2.11. D-spacings calculated from XRD patterns were 1.7 nm for $n = 1$ nanoplatelets and 2.2 nm ($n = 2$ bromide) or 2.3 nm ($n = 2$ iodide) for $n = 2$ nanoplatelets. Considering that the lattice constant for the cubic perovskite unit cell is ~ 0.6 nm,[204] it can be deduced that the organic ligand layer is 1 nm thick in stacked nanoplatelet films regardless of the nanoplatelet species.[46]

2.5. Facile Tunability of Bandgap and Surface-Passivating Ligands

2.5.1. Composition-Dependent Bandgap Tunability

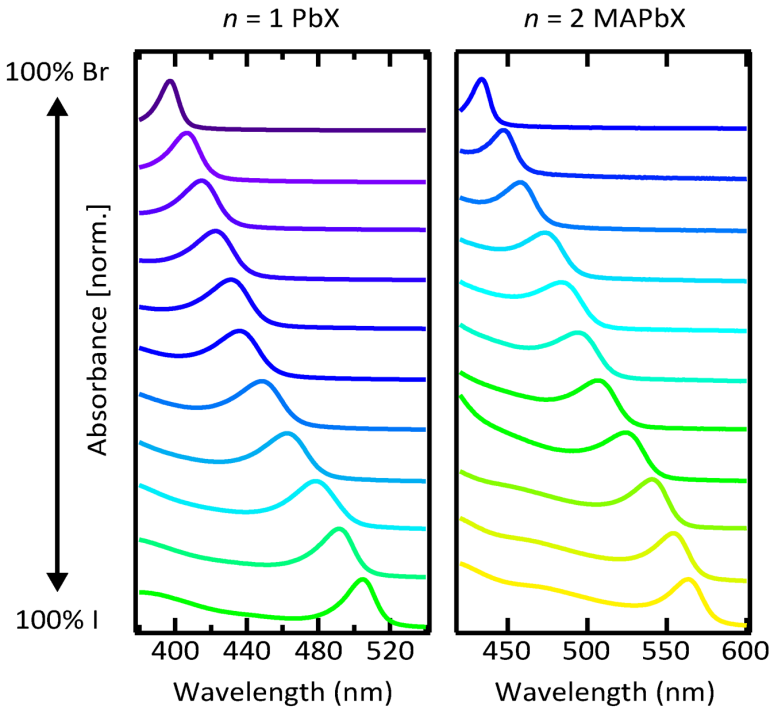

Figure 2.12. Absorption spectra of colloidal perovskite nanoplatelet solutions with mixed halides. Continuous shift of first excitonic absorption features shows bandgap tunability with halide composition.

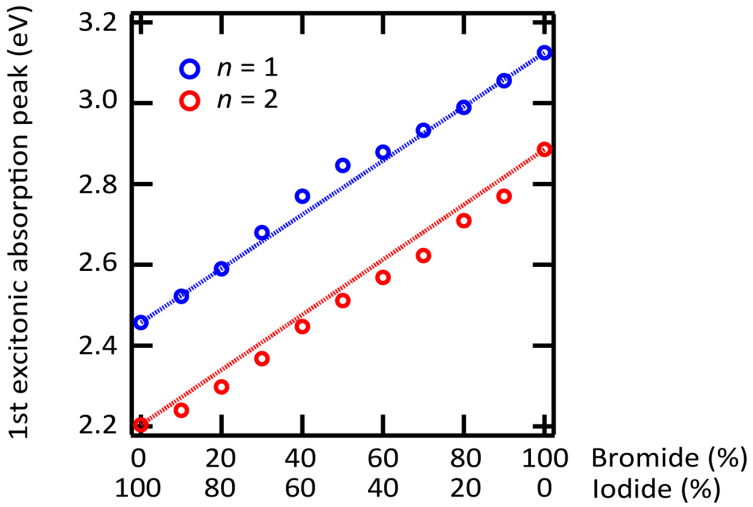

Figure 2.13. First excitonic absorption peak energy as a function of halide composition in the precursor solution for $n = 1$ PbX and $n = 2$ MAPbX nanoplatelets. Dotted lines show the straight line between bromide-only and iodide-only nanoplatelet excitonic absorption energies.

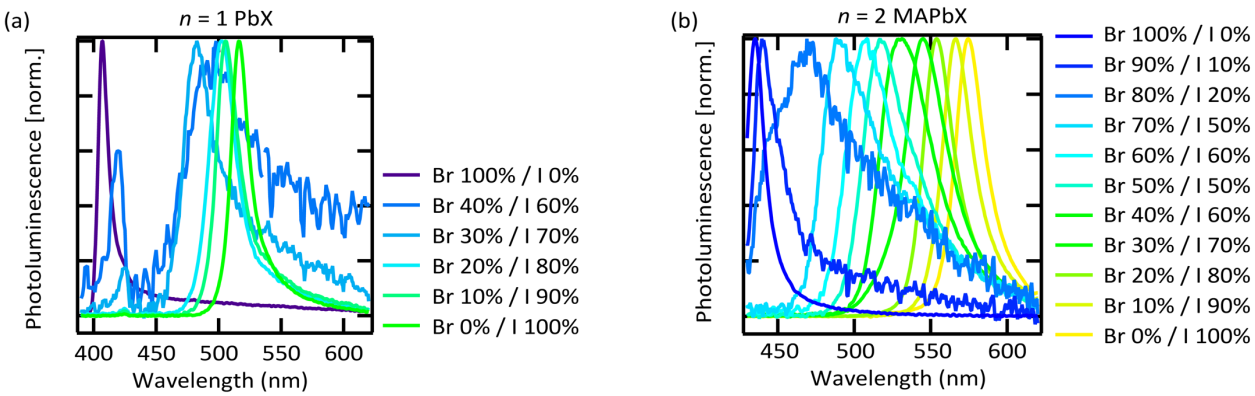

Figure 2.14. Normalized photoluminescence spectra of colloidal (a) n = 1 PbX and (b) n = 2 MAPbX perovskite nanoplatelet solutions with mixed halides.

Next, it is demonstrated that the absorption and emission resonance can be continuously tuned by varying the halide composition. Figure 2.12 shows the normalized absorption spectra of colloidal n = 1 PbX and n = 2 MAPbX nanoplatelet solutions with varying ratios of bromide and iodide. Clear excitonic absorption peaks indicate strong confinement of carriers in nanoplatelets, and continuous shift of those peaks with halide composition demonstrates band gap tunability through halide composition variation (Figure 2.13). However, photoluminescence from mixed-halide nanoplatelet solutions were very weak and exhibited broad or multiple features (Figure 2.14), possibly due to photoinduced halide segregation.[205]

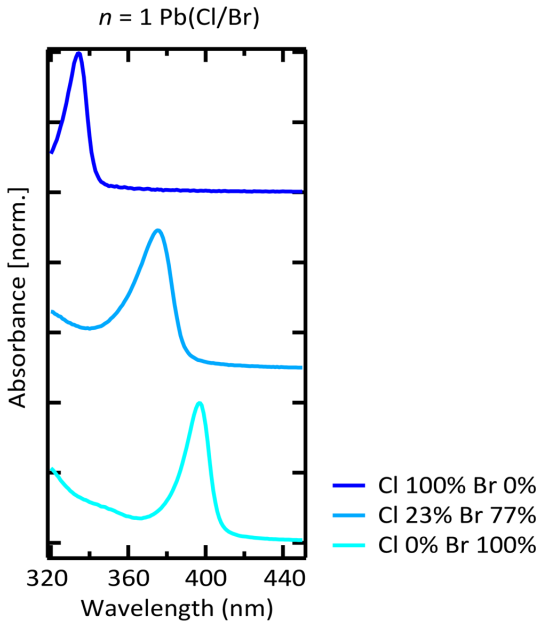

Figure 2.15. Normalized absorption spectra of n = 1 Pb(Cl/Br) nanoplatelet solutions.

Although this work mostly focused on MA- and FA-incorporating bromide/iodide nanoplatelets, chloride- and cesium-incorporating nanoplatelets can also be synthesized by the same approach (Figure 2.15). However, chloride-containing nanoplatelets do not emit in the visible range and the cesium-based nanoplatelets have been reported to suffer from inferior stability as well as thickness homogeneity when synthesized via ligand-assisted reprecipitation.[46]

2.5.2. Surface-Passivating Ligand Tunability

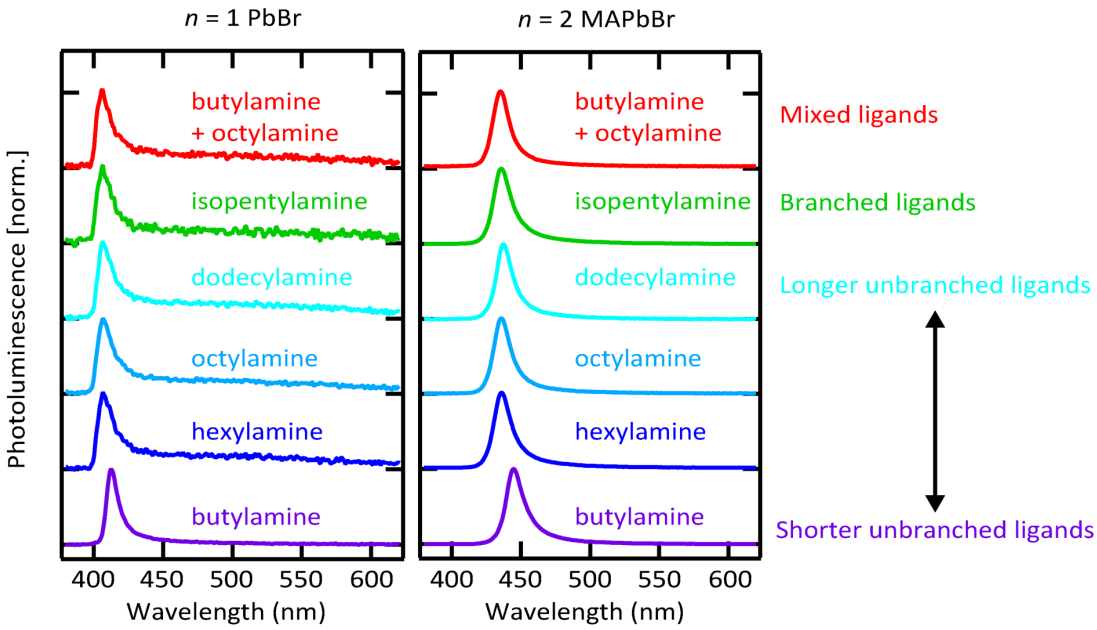

Figure 2.16. Photoluminescence spectra of n = 1 PbBr and n = 2 MAPbBr nanoplatelets synthesized with different ligand species. The reprecipitation method can be easily extended to other ligand chemistries. Longpass filter (Cut-on wavelength: 400 nm) was used to filter out excitation UV light before photoluminescence spectrum collection and it could have slightly altered n = 1 lead bromide nanoplatelet emission spectrum.

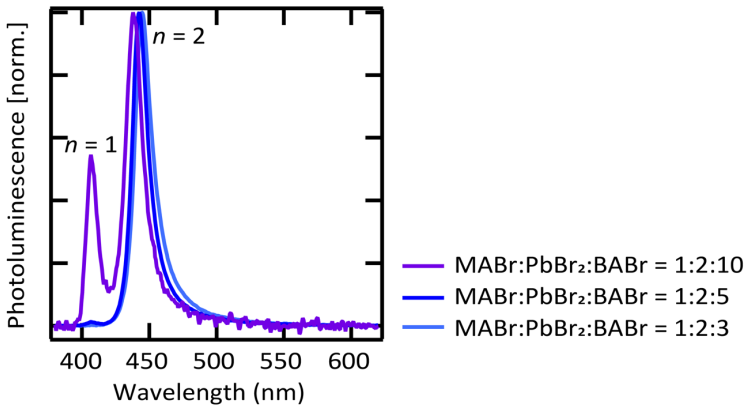

Figure 2.17. Normalized photoluminescence spectra of colloidal lead bromide perovskite nanoplatelet solution with varying amounts of butylammonium bromide ligands added in the precursor solution.

The ligand-assisted reprecipitation method is particularly amenable to changing the identity of the surface-capping ligand, as shown in Figure 2.16, ranging from short unbranched ligands to longer, branched, and even mixed ligands. This opens up the possibility of tuning the nature of the surface-bound organic species for the optimized performance of a specific device or application.[206] However, the ratios between individual precursors needs to be slightly adjusted when employing new ligand species for the best thickness homogeneity of the resulting system. When the mixture of butylammonium and octylammonium were used as ligands, the optimal ratio between MABr, $PbBr_2$, and LBr (L: alkylammonium) in the precursor solution mixture was determined to be 1:2:10 to ensure $n = 2$ nanoplatelet thickness homogeneity (Figure 2.5). However, when butylammonium was employed as the only ligand species in the system, precursor solution formulated with the same ratio resulted in the formation of both $n = 1$ and $n = 2$ nanoplatelets (Figure 2.17). Ratio between MABr, $PbBr_2$, and BABr had to be modified to 1:2:3 to retain the thickness purity of the system. Formulations for the synthesis of nanoplatelets shown in Figure 2.16 is summarized in Table 2.3.

Nanoplatelets	Ligands	MABr	$PbBr_2$	BABr	HABr	OABr	DDABr	i-PABr
n=1 PbBr	*butylamine*	0	1	2	0	0	0	0
n=1 PbBr	*hexylamine*	0	1	0	2	0	0	0
n=1 PbBr	*octylamine*	1	1	0	0	2	0	0
n=1 PbBr	*dodecylamine*	0	1	0	0	0	2	0
n=1 PbBr	*isopentylamine*	0	1	0	0	0	0	2
n=1 PbBr	*butylamine + octylamine*	0	1	1	1	0	0	0
n=2 MAPbBr	*butylamine*	1	2	3	0	0	0	0
n=2 MAPbBr	*hexylamine*	1	2	0	5	0	0	0
n=2 MAPbBr	*octylamine*	1	2	0	0	10	0	0
n=2 MAPbBr	*dodecylamine*	1	2	0	0	0	5	0
n=2 MAPbBr	*isopentylamine*	1	2	0	0	0	0	5
n=2 MAPbBr	*butylamine + octylamine*	1	2	5	5	0	0	0

Table 2.3. Formulation guidelines for perovskite nanoplatelet precursor solutions with different ligand species. Numbers in the table indicate the volumetric equivalents of each precursor solutions (columns) that should be combined to achieve the targeted nanoplatelets (rows), according to the concentration specifications in the Methods section. (Abbreviations: HABr: hexylammonium bromide, DDABr: dodecylammonium bromide, i-PABr: isopentylammonium bromide)

2.6. Practical Tips on the Synthesis and Storage

2.6.1. Effect of Synthetic Variability

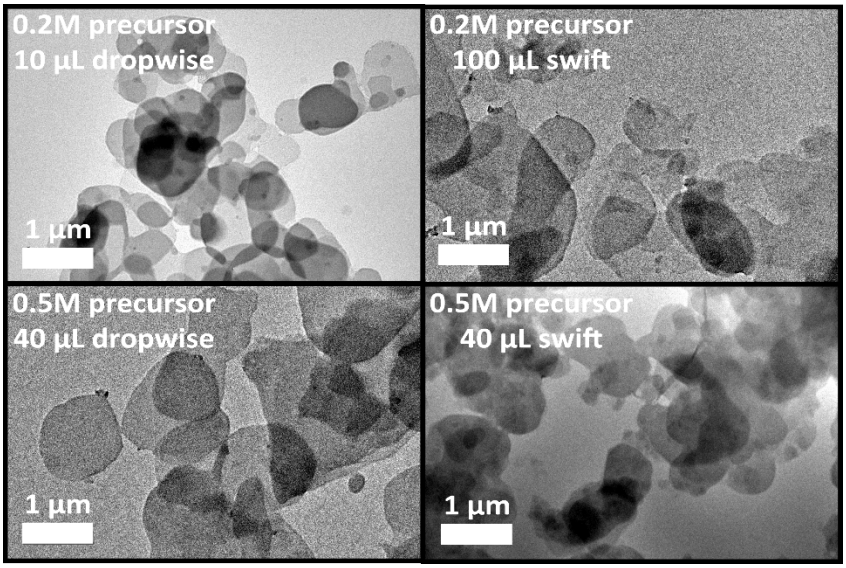

Figure 2.18. Transmission electron microscopy (TEM) images of n = 2 MAPbBr nanoplatelets synthesized by different injection methods with varying amounts of precursor solution.

Figure 2.18 shows TEM images of n = 2 MAPbBr nanoplatelets with BA/OA mixed ligands that were synthesized with several variations in synthetic protocols: precursor solution concentrations (0.2 M vs. 0.5 M), precursor solution volumes (10 μL vs. 40 μL vs. 100 μL), and injection speed (dropwise vs. swift). As-synthesized nanoplatelets did not show noticeable differences in their shape, size and polydispersity. These results suggests that colloidal perovskite nanoplatelet synthesis via ligand-assisted reprecipitation technique can be highly reproducible even with synthetic variabilities.

2.6.2. Nanoplatelet Aggregation and Precipitation

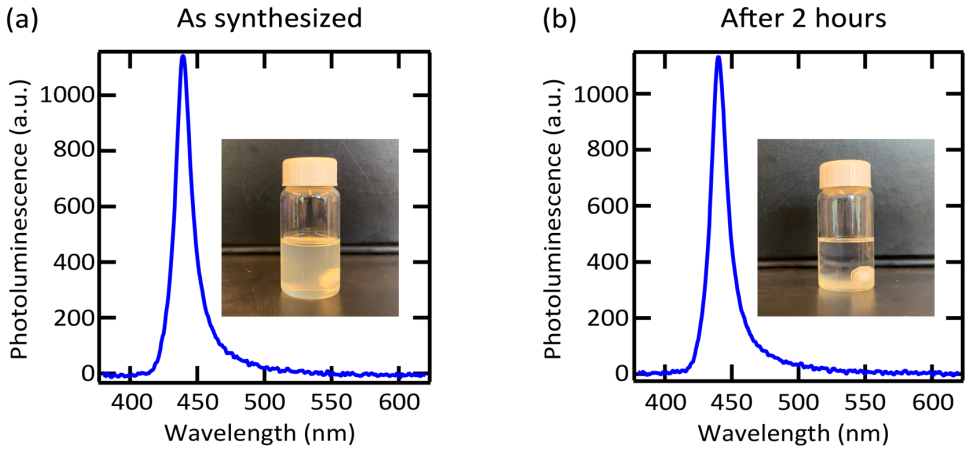

Figure 2.19. Photoluminescence spectra of (a) as-synthesized n = 2 MAPbBr nanoplatelet solution and (b) after nanoplatelet precipitation and redispersion. (Insets: Images of (a) as-synthesized and (b) precipitated perovskite nanoplatelet solutions.) To maximize the visibility of nanoplatelet precipitation, 100 µL of 0.2M precursor solution, instead of standard 10 µL, was injected dropwise into 10 mL toluene for this experiment.

Besides, slow precipitation of colloidal perovskite nanoplatelets was observed, especially when the nanoplatelet concentration was high. In order to determine whether the precipitation originates from the aggregation of nanoplatelets or degradation of nanoplatelets and the formation of unwanted species, PL spectra of nanoplatelets solution before and after precipitation were compared. As shown in Figure 2.19, redispersed nanoplatelets in solution after precipitation still showed quantum-confined n = 2 MAPbBr nanoplatelet emission with the same intensity as before precipitation. This confirmed that precipitation occurred due to the simple aggregation of the nanoplatelets without any change in the structure of nanoplatelets. However, since colloidal perovskite nanoplatelets slowly aggregate and precipitate over time, it is not recommended to store the nanoplatelet solution for a long time. Complete redispersion after precipitation can be difficult when nanoplatelet concentration is high.

2.7. Conclusion

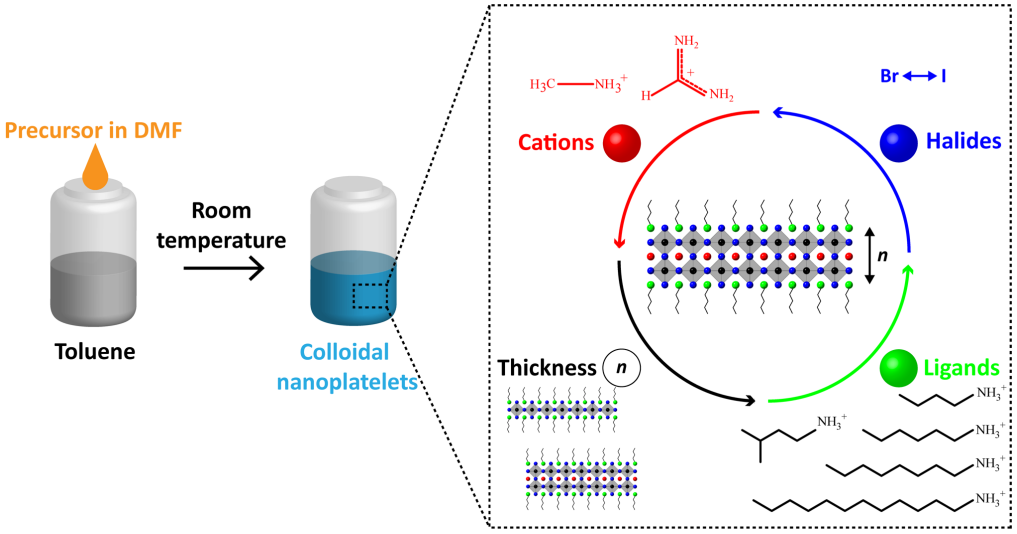

Figure 2.20. Schematic illustration of the synthetic protocol and its universal applicability in synthesizing colloidal lead halide perovskite nanoplatelets with various thicknesses and compositions.

In conclusion, a simple, versatile method for synthesizing colloidal lead halide perovskite nanoplatelets with varying composition has been demonstrated (Figure 2.20). Along with the thickness of the nanoplatelets that governs the extent of quantum-confinement, varying the stoichiometry of the halide ion(s) has been shown to be an effective strategy in tuning the band gap of perovskite nanoplatelets in the visible range. Furthermore, it has been demonstrated that the surface-passivating ligand species can be easily varied while using the same synthetic protocol, which opens up the possibility of further optimizing the surface property of colloidal perovskite nanoplatelets for specific applications. This methodology represents a simple procedure for preparing dispersions of emissive 2D colloidal semiconductors.

The ligand-assisted reprecipitation approach is potentially amenable to high-throughput synthesis and further data-driven analysis. Thickness-, composition- and ligand-tunability can be achieved without any major modifications in the synthetic protocols. Moving forward, it would be desirable to further increase the photoluminescence efficiency to levels commensurate with other perovskite nanocrystals.[66, 200, 207]

2.8. Methods

For better stability and optical properties of resulting perovskite nanoplatelets, it is recommended to complete the whole procedure under inert conditions[35] (i.e., a nitrogen glovebox).

2.8.1. Preparation of Perovskite Nanoplatelet Precursor Solutions

1. Prepare 0.2 M solutions of methylammonium bromide (MABr), formamidinium bromide (FABr), lead bromide ($PbBr_2$), butylammonium bromide (BABr), octylammonium bromide (OABr), methylammonium iodide (MAI), formamidinium iodide (FAI), lead iodide (PbI_2), butylammonium iodide (BAI), and octylammonium iodide (OAI) in N,N-dimethylformamide (DMF) either by dissolving each salt in DMF or by diluting commercially available solutions.

- $PbBr_2$ is not readily soluble in DMF at room temperature. Keep the solution at 80 °C for 10 min for complete dissolution and cool the solution back to room temperature before use.
- Concentration of individual precursor solutions can be increased to synthesize more nanoplatelets.

2. Mix those individual precursor solutions in specific volumetric ratios for each target thickness and composition.

- To synthesize bromide-only or iodide-only nanoplatelets, see Table 2.1, which summarizes the volumetric ratios for $n = 1$ and $n = 2$ bromide and iodide nanoplatelets.
- To synthesize nanoplatelets with mixed halide compositions, combine bromide-only and iodide-only perovskite nanoplatelet precursor solutions of the same thickness at desired volumetric ratio for the target composition. For example, to make 30%-bromide-70%-iodide $n = 2$ perovskite nanoplatelets, mix the precursor solutions of $n = 2$ MAPbBr and $n = 2$ MAPbI at a 3:7 volumetric ratio.
- Changing the organic cation does not significantly affect the optical transition energies.[81] Absorption and luminescence are primarily tuned by changing the halide composition or nanoplatelet thickness.

2.8.2. Synthesis of Perovskite Nanoplatelets

1. Inject 10 μL of mixed precursor solution into 10 mL of toluene under vigorous stirring. Nanoplatelets will instantaneously crystallize due to the abrupt change in the solubility.

- The amount of mixed precursor solution injected into toluene can be increased up to ~100 μL. Total amount of injected precursor solution and injection speed do not seem to significantly affect perovskite nanoplatelet morphology (Figure 2.18). However, injection of too much DMF increases the polarity of the solution and reduces the crystallization.

2. Leave the solution under stirring for 10 min until no further color change is observed from the solution to ensure complete crystallization of perovskite nanoplatelets.

- Freshly synthesized perovskite nanoplatelets from freshly prepared precursor solutions usually show the best photoluminescence quantum yield and photostability.[35] And over time, nanoplatelets will slowly aggregate (Figure 2.19), deteriorating colloidal stability. Thus, it is recommended to use nanoplatelet solutions as soon as possible once synthesized.

3. Centrifuge the solution, discard the supernatant and redisperse the precipitated nanoplatelets in desired amount of solvent.

- Depending on the usage of nanoplatelets, the volume of the redispersing solvent can be freely adjusted and various nonpolar organic solvents such as hexane, octane or chlorobenzene can be used instead of toluene.

2.8.3. Characterization

Photoluminescence spectra: A 365 nm LED was used to excite samples, and PL spectra were collected using an Avantes fiber-coupled spectrometer.

Photoluminescence quantum yield (PLQY): PLQY measurements were performed using an integrating sphere and Avantes fiber-optic spectrometer. A 365 nm LED was used to excite samples. PLQYs were calculated by following a previously reported method.[208]

Absorption spectra: Absorption spectra were taken by a Cary 5000 UV-Vis spectrophotometer.

X-ray diffraction (XRD): XRD was performed using a PANalytical X'Pert Pro operating at 45 kV and 40 mA with a copper radiation source. Background subtraction was done by using HighScore software.

Transmission electron microscopy (TEM): TEM images were taken using a FEI Tecnai G2 Spirit Twin instrument operating at 120 kV.

XRD and TEM sample preparation:

1. Centrifuge the solution at 2050 x *g* for 10 min.
2. Discard the supernatant.
3. Redisperse the nanoplatelets in 1 mL (for TEM) or 30 µL of toluene (for XRD).
4. Drop 1 droplet on a TEM grid (for TEM) for glass slide (for XRD).
5. Dry the sample under vacuum.

Chapter 3. Stability Enhancement of Perovskite Nanoplatelets

The basis of this chapter has been published as:

Ha, S.K.; Mauck, C.M.; Tisdale, W.A. "Toward Stable Deep-Blue Luminescent Colloidal Lead Halide Perovskite Nanoplatelets: Systematic Photostability Investigation" ***Chem. Mater.*** 31 (7), 2486-2496 (2019)

3.1. Project Introduction

One of the most successful commercial applications of semiconductor nanomaterials is in light-emitting technologies.[15] However, achieving efficient deep-blue luminescence – required for a wide color gamut – has been challenging, compared to the state-of-the-art red and green luminescence. Blue-emitting devices fabricated with wide-bandgap semiconductor materials still suffer from limited operational lifetime, efficiency roll-off, low charge carrier mobility, relatively low efficiency compared to green and red analogues, and high manufacturing cost.[12, 209-213]

Recently, lead halide perovskites, with formula ABX_3 (A = small cation, B = Pb, X = Cl, Br, I), have emerged as a promising class of materials for optoelectronic applications. Rapid development of perovskite solar cells[67-69, 214] has demonstrated their fascinating properties such as low-temperature synthesis,[186] long charge carrier diffusion lengths,[76-79] wide compositional tunability[70, 80] and defect tolerance.[81, 82] Furthermore, when prepared as colloidal 3D nanocrystals,[66, 198, 200, 215] lead halide perovskites can achieve large exciton binding energies on the order of hundreds of meV[86, 88] and bright luminescence.[90, 91, 96] Deep-blue luminescence from ABX_3 perovskites has been attempted through chloride incorporation to shift the band gap to higher energies or by reducing the size of quantum dots,[187, 216-218] yet efficient deep-blue luminescence has been elusive. Instead, two-dimensional (2D) lead bromide perovskites ($L_2[ABX_3]BX_4$, where L = butylammonium or octylammonium) have emerged for deep blue luminescent applications due to their strongly quantum- and dielectric-confined nature, leading to thickness-dependent tunability and spectrally narrow emission with small Stokes shifts.[46, 138, 140, 142, 145, 146, 150, 153, 162, 207, 219] Directional light emission, previously observed in other 2D semiconductor nanomaterials,[45, 65] further highlights the possibility of enhancing the outcoupling efficiency of 2D-perovskite-based devices. Multiple methods have been reported on the synthesis of 2D perovskites including ligand-assisted reprecipitation,[46, 142, 153] hot-injection synthesis,[145, 146] and layered perovskite crystal growth.[156, 162, 207] Colloidal 2D perovskites, sometimes referred to as perovskite nanoplatelets, are highly promising for their additional property of solution processability. However, progress in blue light emission from 2D perovskites has lagged behind that of red- and green-emitting materials, and their optoelectronic devices either do not reach the deep-blue region,[148, 190, 220, 221] are low in efficiency,[150, 188] or are unstable under operating conditions.[150, 188]

Many authors have noted that lead bromide perovskite nanoplatelets undergo significant changes to their optical properties when exposed to ultraviolet (UV) light.[46, 134] Poor photostability poses a crucial obstacle to realizing commercial light-emitting technologies, yet comprehensive understanding of the factors influencing photostability in perovskite nanoplatelets is lacking. In this work, colloidal organic-inorganic hybrid lead bromide nanoplatelets, which emit in the deep-blue region (λ_{max} = 437 nm), are synthesized by facile ligand-assisted reprecipitation methods. Then photoinstability of perovskite nanoplatelets is categorized into two aspects: photobleaching, which refers to the decrease in photoluminescence (PL) intensity, and transformation, resulting in the emergence of PL peaks with different wavelengths from the original peak. It is shown that using freshly prepared precursor solutions dramatically enhances the stability, in addition to substituting formamidinium for methylammonium and isolating samples from moisture. Lastly, adding excess alkylammonium bromide surface capping ligands is demonstrated as an effective strategy to further enhance the intrinsic stability of nanoplatelets. Dropcast films of nanoplatelets with excess ligands exhibit impressive stability both under UV and under ambient conditions. These photostability studies on colloidal perovskite nanoplatelets serve as a guide for future fabrication of stable and efficient deep-blue emitting devices.

3.2. Synthesis and Characterization of Perovskite Nanoplatelets

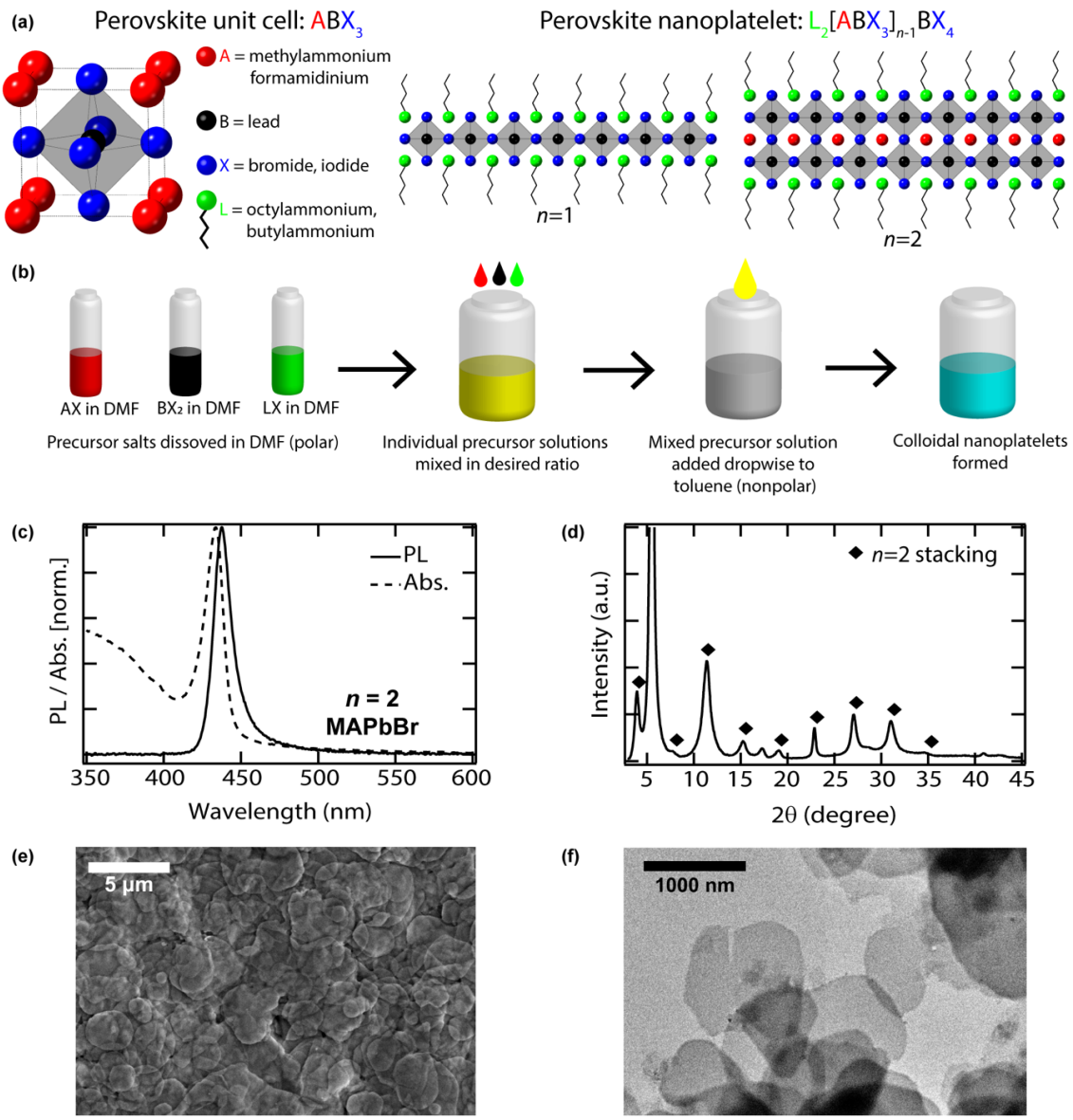

Figure 3.1. Synthesis and characterization of lead halide perovskite nanoplatelets. (a) Structures of perovskite unit cell and perovskite nanoplatelets with the chemical species used in this study. The parameter *n* indicates the number of lead halide octahedral layers in the direction of nanoplatelet thickness. (b) Schematic illustration of nanoplatelet synthesis procedure. (c) Solution phase photoluminescence and absorption spectra of colloidal $n = 2$ MAPbBr nanoplatelets in toluene. (d) X-ray diffraction (XRD) pattern of a drop-cast $n = 2$ MAPbBr nanoplatelet film. (e) Scanning electron microscopy (SEM) image and (f) Transmission electron microscopy (TEM) image of $n = 2$ MAPbBr nanoplatelets.

Colloidal perovskite nanoplatelets (Chemical formula: $L_2[ABX_3]_{n-1}BX_4$ where *n* refers to the number of octahedral $[BX_6]^{4-}$ layers in the direction of confinement) were synthesized by ligand-

assisted reprecipitation method[46, 167] with slight modifications. Methylammonium (MA) and formamidinium (FA) were used as A-site organic cations in this study, with lead (Pb) as B-site metal cation, and bromide (Br) and iodide (I) as halide anions. For better colloidal stability and thickness control of nanoplatelets, a 1:1 mixture of butylammonium (BA) and octylammonium (OA) were incorporated as ligands (Figure 3.1a).[46] Schematic illustration in Figure 3.1b shows the synthesis procedure. First, precursor salts (AX, BX_2 and LX) were dissolved and precursor solutions were mixed in the desired ratio for specific target thickness (Table 3.1). Lastly, this mixed precursor solution was dropped into toluene and perovskite nanoplatelets were crystallized due to the abrupt change in solubility. Further details are included under Methods section.

	MABr	FABr	$PbBr_2$	BABr	OABr	MAI	FAI	PbI_2	BAI	OAI
n=1 PbBr	0	0	2	3	3	0	0	0	0	0
n=2 FAPbBr	0	1	2	5	5	0	0	0	0	0
n=2 MAPbBr (2.5x ligands)	1	0	2	2.5	2.5	0	0	0	0	0
n=2 MAPbBr (5x ligands)	1	0	2	5	5	0	0	0	0	0
n=2 MAPbBr (10x ligands)	1	0	2	10	10	0	0	0	0	0
n=1 PbI	0	0	0	0	0	0	0	2	3	3
n=2 FAPbI	0	0	0	0	0	0	1	2	5	5
n=2 MAPbI	0	0	0	0	0	1	0	2	5	5

Table 3.1. Formulations of mixed precursor solutions for various colloidal perovskite nanoplatelets. Each number indicates the volumetric ratio of individual precursor solutions (0.2M) in mixed precursor solution.

Through this method, colloidal n = 2 methylammonium lead bromide (MAPbBr) nanoplatelets that emit in deep-blue range (λ_{max} = 437 nm) with narrow full-width-at-half-maximum (FWHM = 14 nm) and small Stokes shift (4 nm) (Figure 3.1c) were synthesized. When dropcast, the nanoplatelets preferentially lay flat on the substrate with a stacking periodicity of 2.2 nm, as seen by the periodic stacking peaks[46, 148] at integer multiples of 3.9º observed in the X-ray diffraction (XRD) pattern (Figure 3.1d). The nanoplatelets, which have lateral dimension ranging from 0.5-5 μm (Figure 3.1e-f), appear to be dispersed as individual sheets in the colloidal solution based on contrast in transmission electron microscopy (TEM) images (Figure 3.1f).

3.3. Classifying Types of Photoinstability: Photobleaching and Transformation

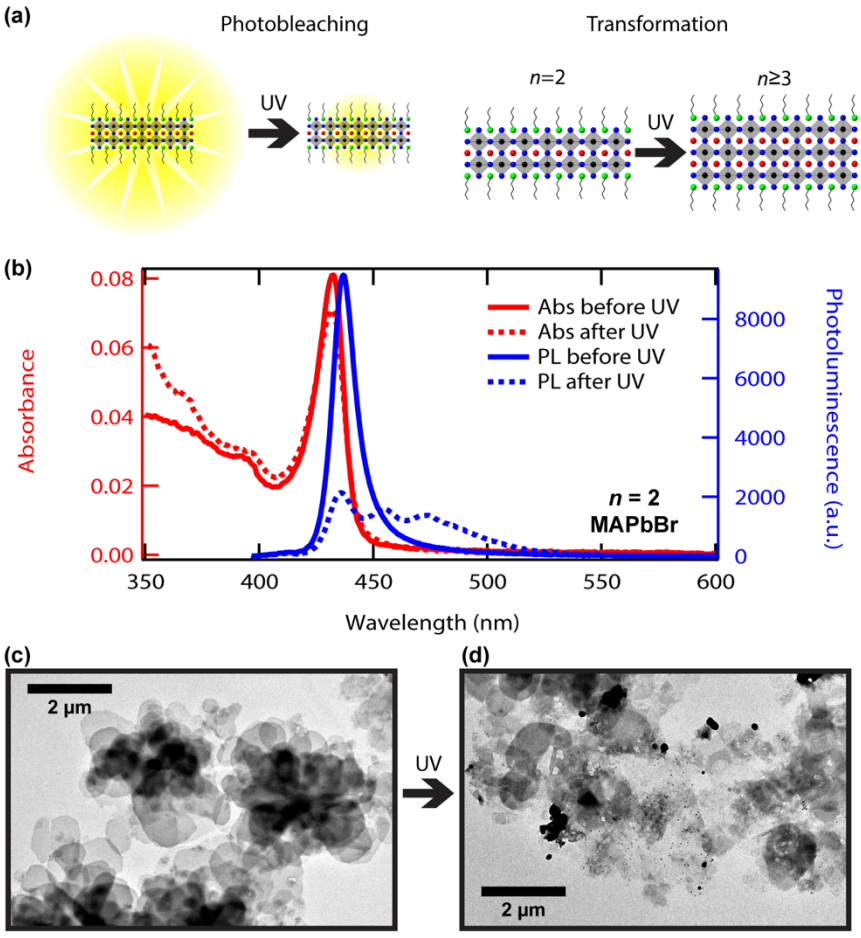

Figure 3.2. Photoinstability of lead halide perovskite nanoplatelets. (a) Schematic illustrations of two changes that nanoplatelets suffer under UV irradiation. (b) Photoluminescence and absorption spectra of colloidal n = 2 MAPbBr nanoplatelets in toluene before and after UV irradiation under air. (365 nm, 180 mW/cm^2, 1 hour) (c-d) TEM image of n = 2 MAPbBr nanoplatelets before and after UV irradiation.

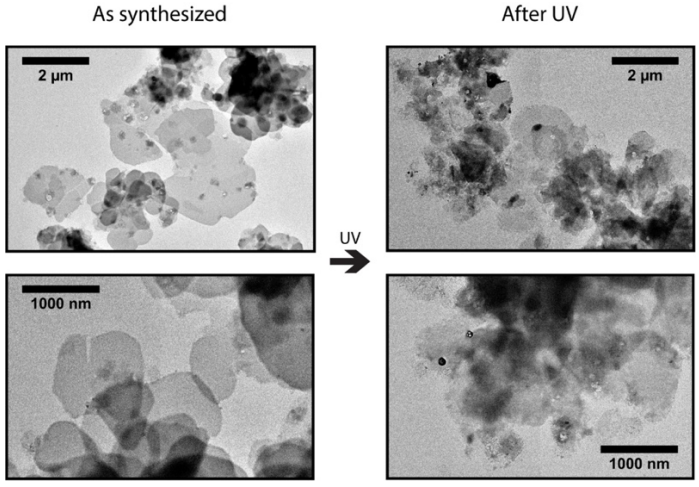

Figure 3.3. TEM images of n = 2 MAPbBr nanoplatelets before and after UV irradiation.

In Figure 3.2a, two photoinstability phenomena that nanoplatelets suffer under UV irradiation are categorized, namely *photobleaching* and *transformation*. As seen in figure 3.2b, PL from n = 2 MAPbBr nanoplatelets at 437 nm was greatly reduced after UV irradiation ("photobleaching"). Additionally, PL emission peaks from thicker perovskite structures appeared at 455 nm and 474 nm, which are believed to come from small amounts of n = 3 and n = 4 structures that were formed during UV irradiation ("transformation").[142] However, the decrease of the excitonic feature at 433 nm in the absorption spectrum was less extensive than the 77% decrease in the n = 2 PL peak intensity after UV irradiation. Furthermore, it is noteworthy that only the n = 2 excitonic feature, but not n = 3 or n = 4 features (which should appear at ~450 nm and ~470 nm respectively),[142] was observed in the absorption spectrum after UV irradiation. Transmission electron microscopy (TEM) images in Figure 3.2c and Figure 3.2d show the structure of nanoplatelets before and after UV exposure. In Figure 3.2c, individual nanoplatelets could be easily distinguished and identified, although they were mostly stacked together presumably due to high surface-to-volume ratio. As shown in Figure 3.2d, it became difficult to distinguish individual nanoplatelets once irradiated; regions of strong TEM contrast were observed which are smaller than the lateral dimension of the nanoplatelets (~1 μm), possibly revealing thickness variations within individual nanoplatelets or degradation products. TEM images shown in Figure 3.2c-d are representative images, and additional images showing nanoplatelet degradation can be found in Figure 3.3.

To test for a change in Pb oxidation state (signifying different chemical bonding in the sample), freshly prepared and irradiated samples were characterized with X-ray photoelectron spectroscopy (XPS, Figure 3.4). However, no significant change in binding energies for species that constitute nanoplatelets (C, N, Pb, Br) was observed after UV illumination. Slight shift (~0.2 eV) in binding energies for C, N, Pb and Br accompanied by the increase in the atomic concentration of oxygen after UV irradiation (From 1.95% to 21.70%, which can also be seen in the enhanced signal-to-noise ratio after UV irradiation.) are believed to be coming from the change in the electronic environment induced by adsorbed water molecules. It is likely that, compared to before-UV-irradiation sample, longer exposure of after-UV-irradiation sample to air during irradiation process resulted in more water molecules being adsorbed onto perovskite nanoplatelets. Similar shift in binding energy was observed when $MAPbI_3$ was dipped into 3-hydroxypyridine.[222] Thus, the chemical nature of n = 2 MAPbBr nanoplatelets did not seem to significantly change after UV irradiation.

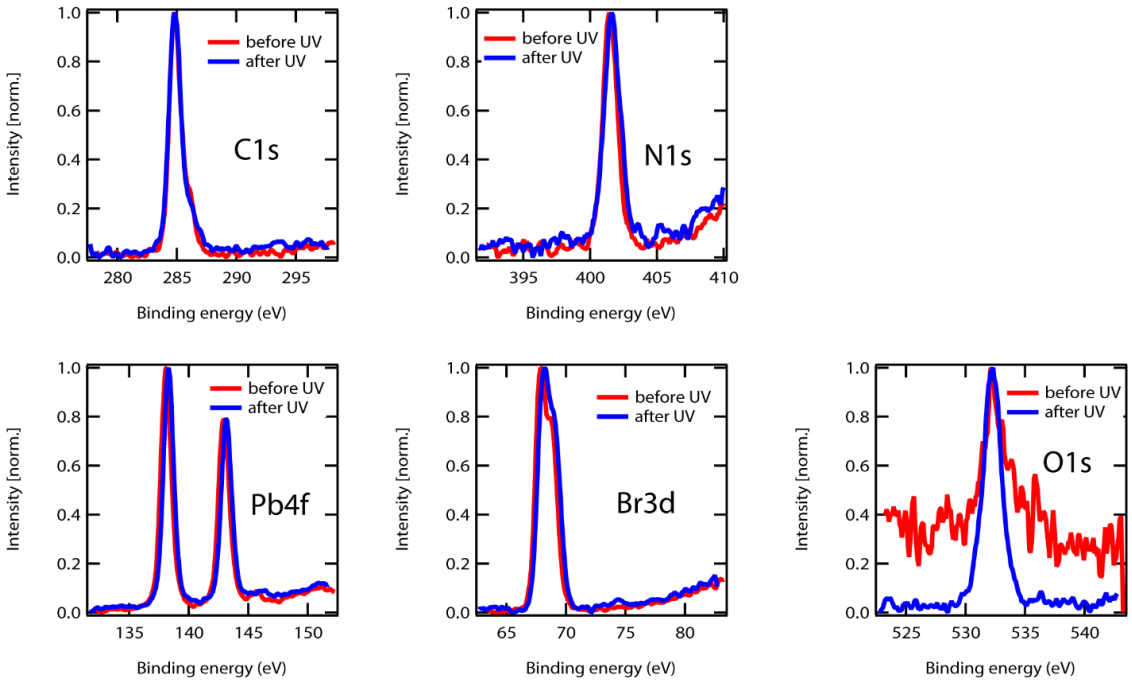

Figure 3.4. X-ray photoelectron spectroscopy (XPS) spectra of the elements constituting $n = 2$ MAPbBr nanoplatelets before and after being irradiated by UV in colloidal solution phase.

On the basis of the observed changes to the absorption and photoluminescence spectra and TEM structural imaging, photobleaching is believed to arise from *both* degradation of a portion of the nanoplatelet dispersion and a reduction in the intrinsic PLQY of the remaining nanoplatelets. Additionally, some of the $n = 2$ nanoplatelet structures are transformed into less-confined ($n = 3$ and $n = 4$ in this case) structures either by structural rearrangement within a single nanoplatelet or by merging of multiple nanoplatelets. Downhill energy transfer from thinner (higher-energy) to thicker (lower-energy) structures combined with higher PLQY of thicker structures can amplify the contribution of redshifted emitters in the ensemble PL spectrum, as observed in Figure 3.2b. Low enthalpy of formation for perovskites[128] combined with facile ionic migration[223] is believed to facilitate the transformation of nanoplatelets into thicker structures in solution. Although slight redshift of PL under UV has already been observed in perovskite quantum dots (QDs),[171] this transformation behavior can be especially problematic for strongly quantum-confined atomically-thin nanoplatelets because slight change in the thickness induce dramatic changes to the ensemble optical properties.

3.4. Effect of Precursor Solution Aging

3.4.1. Effects on Photostability and Photoluminescence Quantum Yield

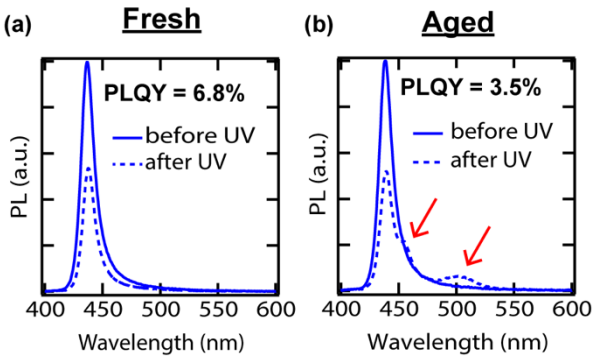

Figure 3.5. Effects of the precursor solution aging. PLQY of as-synthesized colloidal n = 2 MAPbBr nanoplatelets in toluene and solution phase photoluminescence spectra before and after UV irradiation (365 nm, 24 mW/cm^2, 1 hour) under air, when (a) freshly prepared and (b) 2-months-aged precursor solutions were used.

To investigate the role of precursor aging, two batches of n = 2 MAPbBr nanoplatelet species were prepared using two different sets of precursor solutions. One set of precursors was prepared fresh, while the other was stored inside a nitrogen (N_2) glovebox for two months before use. Figure 3.5 shows PLQY and PL spectra of n = 2 MAPbBr nanoplatelet dispersions prepared from fresh and aged precursor solutions. In Figure 3.5a, n = 2 MAPbBr nanoplatelets synthesized from freshly prepared precursor solutions showed solution phase PLQY of 6.8% and did not transform into thicker structures after moderate UV irradiation (24 mW/cm^2) under air for 1 hour. On the other hand, when synthesized from aged precursors, PLQY dropped to 3.5% and PL from n = 3 structures at 455 nm as well as the bulk-like emission around 500 nm appeared, as indicated by the red arrows in Figure 3.5b. Thus, it becomes evident that the aging of individual perovskite precursors even under a N_2 atmosphere affects stability and PLQY of the resultant nanoplatelets.

3.4.2. Fourier Transform Infrared Spectroscopy and ^{1}H Nuclear Magnetic Resonance Analyses

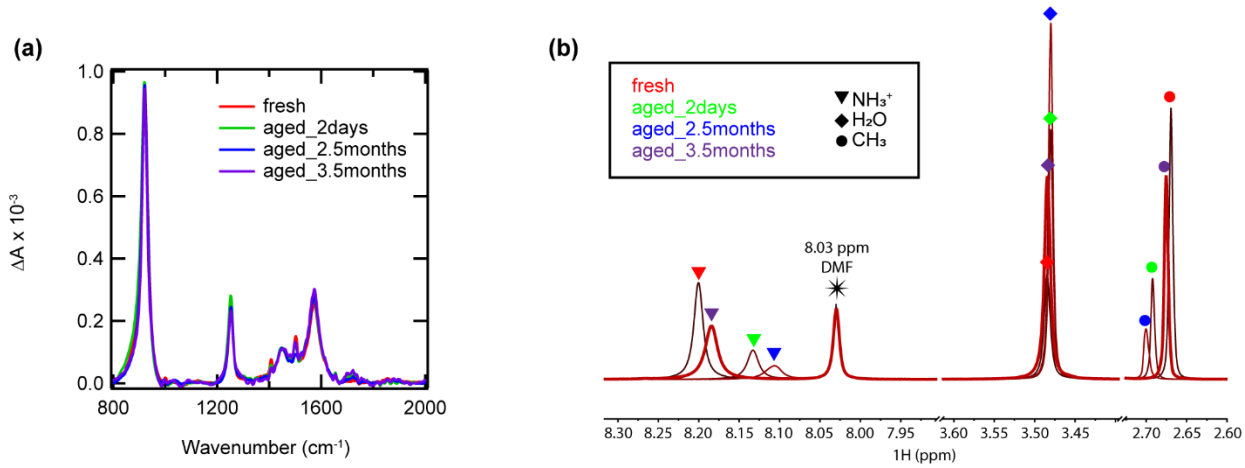

Figure 3.6. (a) Fourier transform infrared spectroscopy (FTIR) and (b) ^{1}H nuclear magnetic resonance (NMR) spectra (400 MHz) of methylammonium bromide dissolved in deuterated DMF ($(CD_3)_2NCDO$) after aging under N_2 for different periods of time.

To elucidate how precursor aging affects the quality of resulting nanoplatelets, first possibility considered was the formation of impurities through slow reaction between alkylammonium bromide and DMF. Among MABr, BABr and OABr, MABr was chosen as a representative of alkylammonium bromide species because of low steric hindrance and high reactivity. First, Fourier-transform infrared (FTIR) spectroscopy was employed to detect the presence of any potential reaction products formed in the MABr/DMF precursor solution after aging in N_2 atmosphere for 0 days (fresh), 2 days, 2.5 months, and 3.5 months. However, no significant difference in the FTIR spectrum was observed (Figure 3.6a). Second, ^{1}H nuclear magnetic resonance (NMR) spectroscopy was employed. Ammonium and methyl proton peaks were observed in the ^{1}H NMR spectrum at 8.11-8.20 ppm and 2.68-2.70 ppm, respectively (Figure 3.6b), as expected from previous studies.[224] Unlike FTIR, NMR spectra revealed slight shifts of ammonium and methyl hydrogen peaks accompanied by a peak at 3.48 ppm were observed in ^{1}H NMR spectra of the fresh and aged precursor solutions dried completely under a steady nitrogen flow and dissolved in deuterated DMF ($(CD_3)_2NCDO$). However, the extent of the NH_3^+ and CH_3 proton chemical shifts was proportional to the integrated area of the 3.48 ppm peak, but these shifts showed no trend with aging period. It is believed that these shifts arise from differing concentrations of water present during NMR sample preparation. Although MABr precursor

solutions were stored inside the glovebox (N_2 atmosphere) during aging periods, the solutions were exposed to air during NMR sample preparation and it is likely that hygroscopic MABr readily adsorbed water molecules during air exposure. Thus, the 3.48 ppm peak was concluded to be a water peak, similar to the chemical shift of water in DMSO at 3.30 ppm.[225] Therefore slight shifts (< 0.07 ppm) in ammonium and methyl hydrogen peaks were found to arise from the change of surrounding solvent environment in the presence of water, and not from any reaction between MABr and DMF, which should lead to the appearance of new peaks whose intensity increases with precursor aging time. Consequently, the presence of side products from alkylammonium salts reacting with DMF was ruled out.

3.4.3. Dynamic Light Scattering Analysis

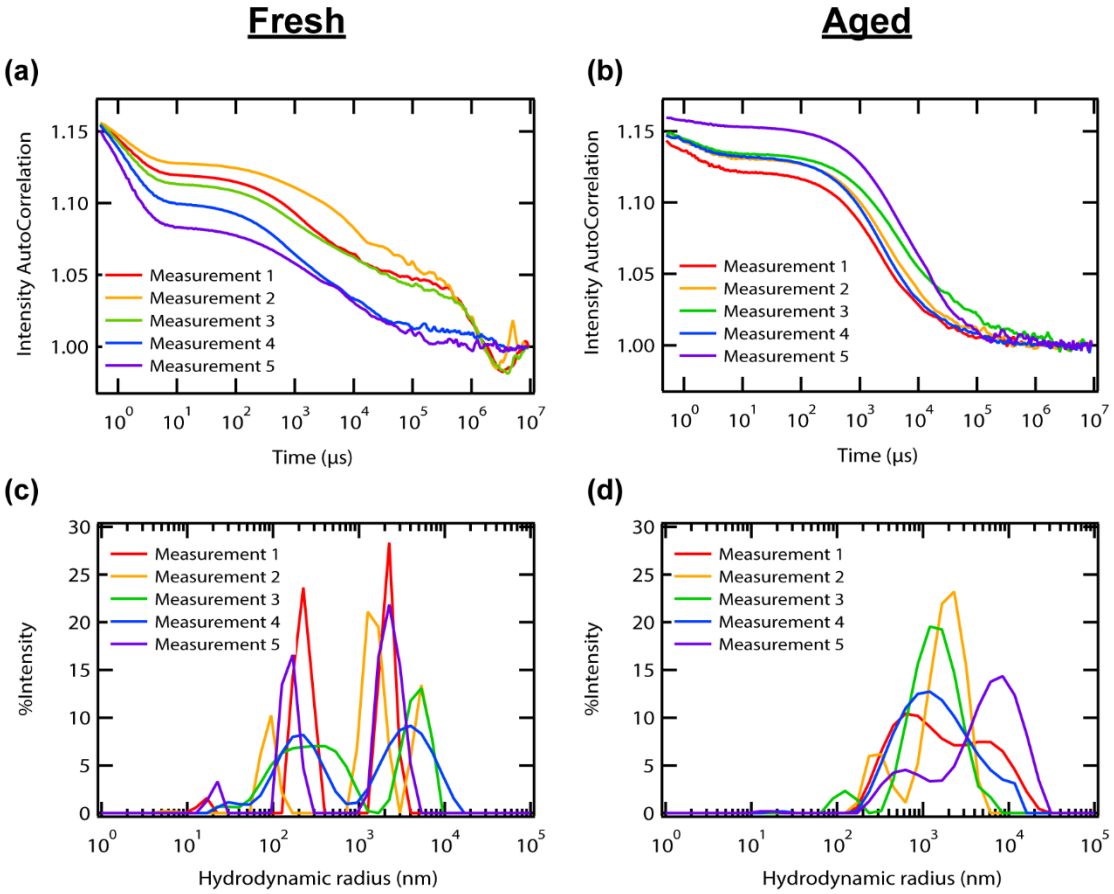

Figure 3.7. Scattered light intensity autocorrelation curves and calculated colloidal size distributions of (a, c) fresh and (b, d) 2-months-aged $PbBr_2$ precursor solution in DMF.

Change in the size distribution of lead polyhalide colloids in DMF was considered as a second possible origin of the precursor aging effect. It has been reported that lead halide exists as lead polyhalide colloids in DMF[226-228] (i.e. $[PbX_3]^-$, $[PbX_4]^{2-}$, $[PbX_5]^{3-}$ and $[PbX_6]^{4-}$) and the size distribution affects crystallization kinetics during spin-coating perovskite precursor solutions in DMF, further affecting the quality of spin-coated perovskite crystal film.[229] To test whether similar behavior might be occurring in this reprecipitation synthesis, dynamic light scattering (DLS) measurements were performed to compare the colloidal size distribution of freshly prepared and 2-month-old $PbBr_2$ solutions in DMF. Scattered light intensity autocorrelation curves and calculated colloidal size distribution data from five different measurements from the same sample are plotted in Figure 3.7. In Figure 3.7a and 3.7b, it could be clearly seen that there were qualitative differences in intensity autocorrelation curves of fresh and aged $PbBr_2$ solutions. In particular, there is a fast decay component in the fresh solution that is missing from the aged solution which correspond to small colloids. Intensity autocorrelation decay of fresh $PbBr_2$ solution showed multi-exponential feature with significant amount of early-time decay ($10^0 \sim 10^1$ μs), while that of aged $PbBr_2$ solution showed more mono-exponential-like decay at later times ($10^3 \sim 10^4$ μs). These results suggest clear changes to the size distribution before and after aging (Figure 3.7c-d). However, large scan-to-scan variation made a quantitative analysis difficult. Considering that large colloids may act as nucleation sites and affect the crystallization kinetics,[229] further study will be needed on the evolution of lead polyhalide colloidal size distribution and how it can be related to the crystallization, stability and PLQY of nanoplatelets.

3.5. Effect of Composition

3.5.1. Effects on Photostability Under Air

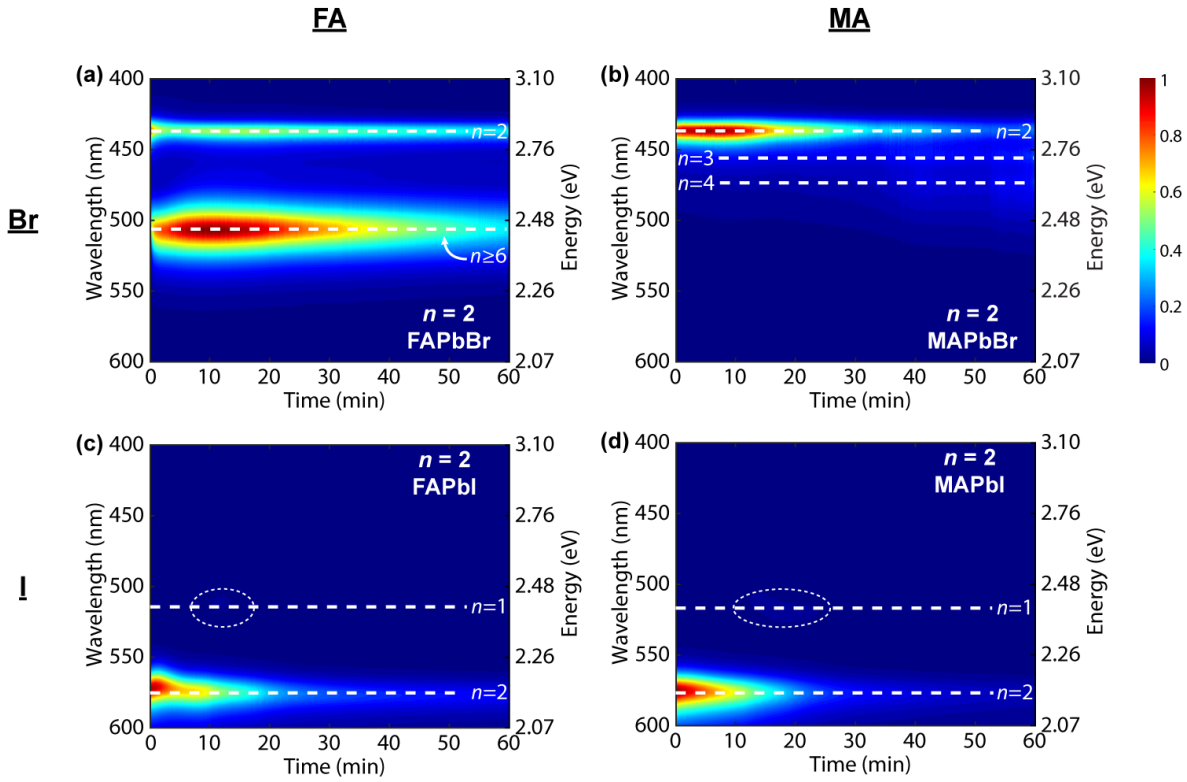

Figure 3.8. Photoluminescence stability under air. (a-d) Evolution of photoluminescence spectra under UV irradiation (365 nm, 180 mW/cm^2) for colloidal n = 2 FAPbBr, n = 2 MAPbBr, n = 2 FAPbI and n = 2 MAPbI nanoplatelets in toluene under air. (White dotted lines indicate the peak positions for nanoplatelets with corresponding compositions and thicknesses.)

In Figure 3.8, it is presented how composition of nanoplatelets affects photostability under air. Four different colloidal nanoplatelet solutions, n = 2 FAPbBr, n = 2 MAPbBr, n = 2 FAPbI and n = 2 MAPbI, were synthesized and UV-irradiated under air while stirring in toluene. To induce fast and dramatic change, extreme UV power density (λ = 365 nm, 180 mW/cm^2) was used. Because lead and halide ions mainly contribute to the formation of band edge electronic states,[81] both MAPbX and FAPbX nanoplatelets have similar PL emission at 437 nm for X=Br and at 575 nm for X=I. In the n = 2 FAPbBr solution (Figure 3.8a), PL from bulk-like ($n \geq 6$) structures appeared immediately upon UV exposure, along with photobleaching of the n = 2 PL peak at 437 nm. On the other hand, photobleaching of the primary n = 2 peak was mainly observed for the first 20 minutes of UV irradiation in n = 2 MAPbBr nanoplatelets, followed eventually by the slow

appearance of PL peaks from $n = 3$ and $n = 4$ structures (Figure 3.8b). The iodide $n = 2$ analogues showed similar photobleaching behavior as their bromide counterparts, as shown in Figure 3.8c and Figure 3.8d. Interestingly, weak blue-shifted PL at 512 nm ($n = 1$) appeared between 10 and 20 minutes of UV irradiation for both MAPbI and FAPbI, but no emission from thicker structures was observed. However, no absorption features associated with $n \neq 2$ structures were observed (Figure 3.9). Slight changes in the solution absorption spectra were observed from both bromide and iodide nanoplatelets when irradiated with UV in air, but the exact mechanism is not yet fully understood and need further investigation.

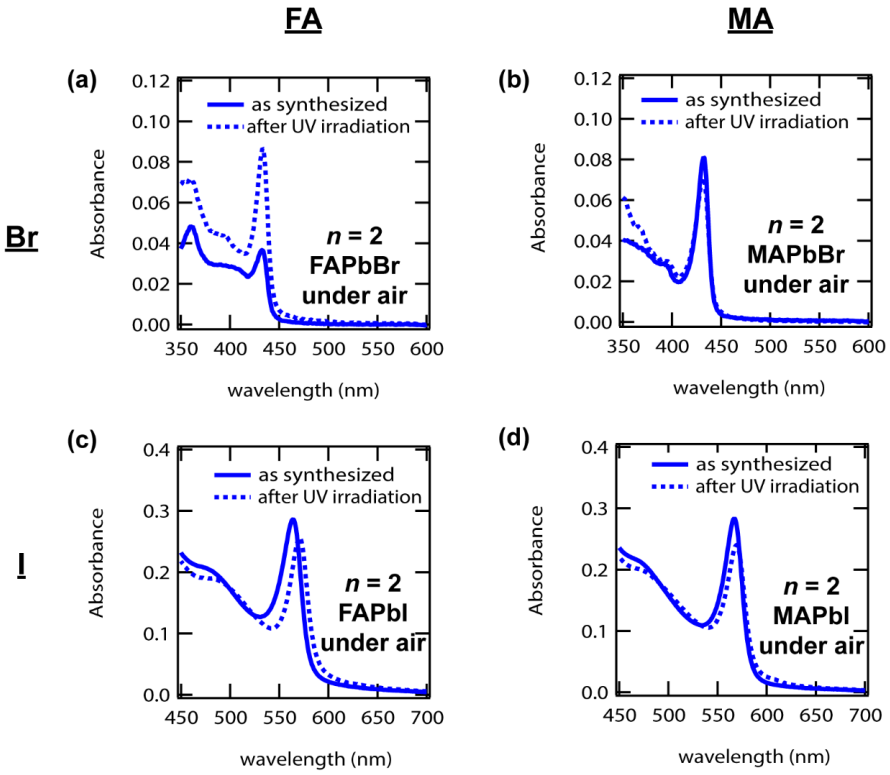

Figure 3.9. (a-d) Absorption spectra before and after UV irradiation (365 nm, 180 mW/cm^2) for colloidal solutions of $n = 2$ FAPbBr, $n = 2$ MAPbBr, $n = 2$ FAPbI and $n = 2$ MAPbI under air.

3.5.2. Effects on Photostability Under N_2

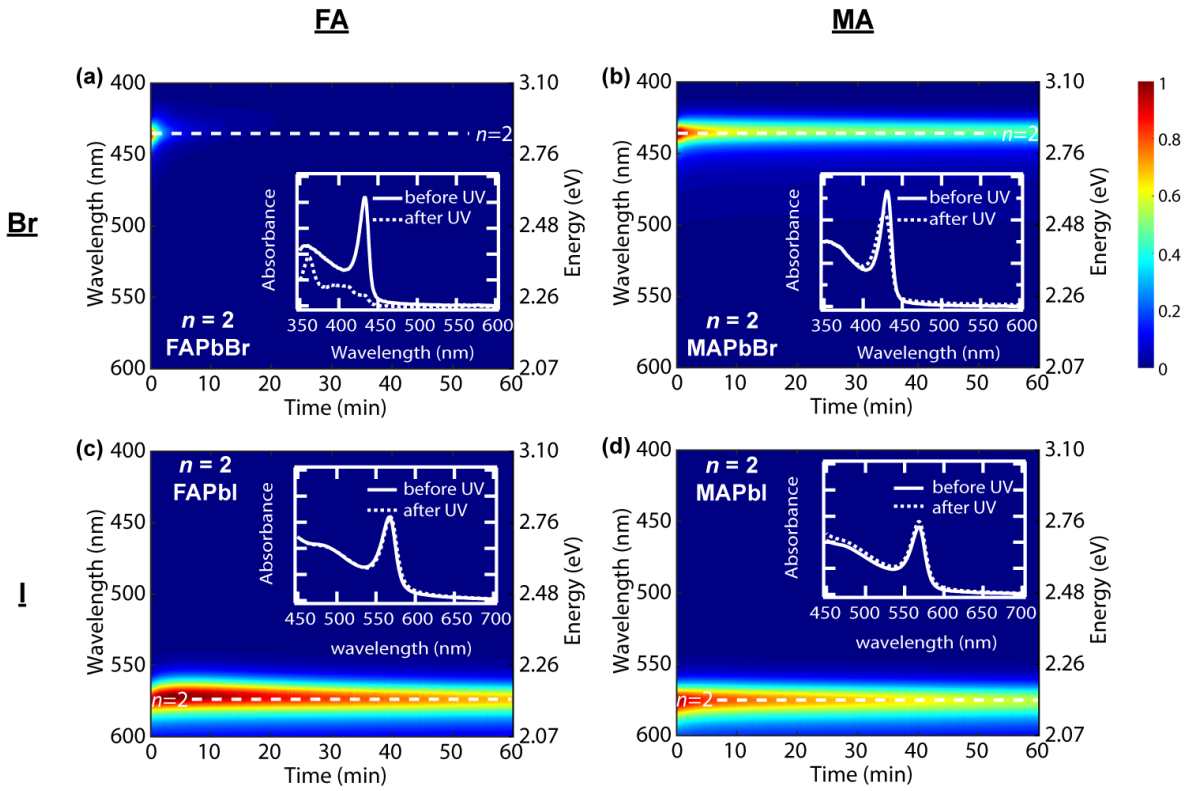

Figure 3.10. Photoluminescence stability under N_2. (a-d) Evolution of photoluminescence spectra under UV irradiation (365 nm, 180 mW/cm^2) for colloidal n = 2 FAPbBr, n = 2 MAPbBr, n = 2 FAPbI and n = 2 MAPbI nanoplatelets in toluene under N_2. (Insets: Absorption spectra before and after UV irradiation. White dotted lines indicate the peak positions for nanoplatelets with corresponding compositions.)

In Figure 3.10, effect of UV irradiation on colloidal nanoplatelet solutions under N_2 atmosphere is shown. Whereas n = 2 MAPbBr nanoplatelets partially maintained their PL intensity after 1 hour of exposure to UV (Figure 3.10b), n = 2 FAPbBr nanoplatelets completely lost PL intensity in a few minutes under UV irradiation (Figure 3.10a). However, photobleaching behaviors of n = 2 MAPbI and n = 2 FAPbI nanoplatelets under N_2 were similar (Figure 3.10c-d), as they also were under air (Figure 3.8c-d). Furthermore, transformation to n = 1 or n > 2 structures was not observed in any of the four colloidal nanoplatelet dispersions irradiated under N_2, although they each demonstrated varying degrees of photobleaching. Note that in Figure 3.10b-d, while nanoplatelet PL intensity significantly dropped, corresponding excitonic features in the absorption spectra did not decrease nearly as much. This again demonstrates that photobleaching is not solely due to a drop in PLQY nor degradation of nanoplatelets, but rather a combination of the two.

Comparing the changes during UV irradiation under air (Figure 3.8 & Figure 3.9) and under N_2 (Figure 3.10), it is concluded that transformation of nanoplatelets to thicker or thinner structures requires the participation of an extrinsic chemical species present in air while photobleaching results from an intrinsic instability of the perovskite nanoplatelet against photoexcitation. No change in the PL spectrum were observed when the nanoplatelet solution was irradiated with sub-bandgap light of similar intensity at 785 nm (Figure 3.11) and it confirms that the observed photobleaching is associated with the absorption of light and consequent excitation of the material. PL enhancement shown in Figure 3.11 is believed to be coming from additional nanoplatelets being formed in the first few minutes after dropping the mixed precursor solution into toluene, which is consistent with the slight redshift in peak positions that are believed to be coming from reabsorption.

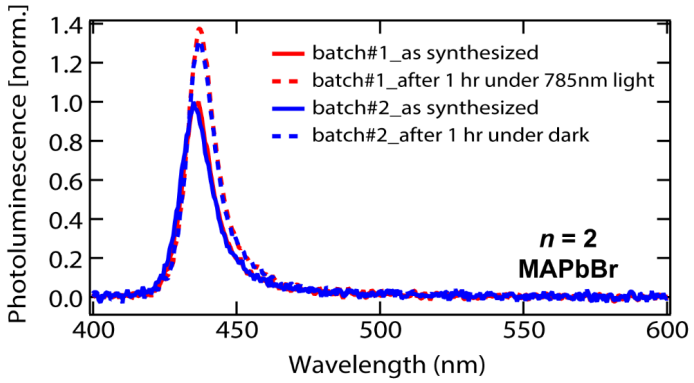

Figure 3.11. Photoluminescence spectra of two colloidal n = 2 MAPbBr nanoplatelet solutions under N_2 before and after being exposed to 785nm light (180 mW/cm^2) for 1 hour and left under dark for 1 hour, respectively.

3.5.3. Correlating Photostability with Structural Stability

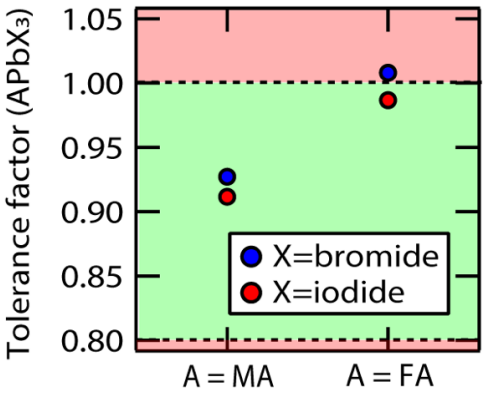

Figure 3.12. Tolerance factors of lead halide perovskites.

I hypothesize that the intrinsic instability of perovskite nanoplatelets under UV photoexcitation can be correlated with the structural stability of the underlying perovskite lattice. Goldschmidt's tolerance factor, defined as $\frac{r_A+r_X}{\sqrt{2}(r_B+r_X)}$ where r_A, r_B and r_X denotes ionic radii of A, B and X ions, respectively, is one parametrization of the structural stability of the perovskite lattice.[230] A stable perovskite structure is predicted to form when the tolerance factor lies between 0.8 and 1,[231] and tuning the tolerance factor to enhance the stability is a popular technique in the field of perovskite solar cells.[71, 80, 232, 233] Figure 3.12 shows the tolerance factors of relevant bulk lead halide perovskites calculated from ionic radii values reported by Kieslich *et al*.[234] Although it has been reported that slight lattice relaxation occurs for two-dimensional nanoplatelets[182] compared to bulk perovskites, I expect tolerance factors of nanoplatelets to be similar to bulk perovskites. From Figures 3.8 and 3.10, it was observed that n = 2 FAPbBr nanoplatelets were least stable compared to n = 2 MAPbBr, n = 2 FAPbI and n = 2 MAPbI. As shown in Figure 3.12, n = 2 FAPbBr has the largest tolerance factor, at the limit of the stable range for the perovskite structure. Considering that perovskites with large tolerance factors tend to relieve strain by forming defect vacancies[232] and defects in perovskite crystal can propagate,[235] I believe that structural instability of n = 2 FAPbBr nanoplatelets may be one of the main causes of such instability under UV irradiation. Also, it has been reported that larger dipole moment of MA compared to FA (2.3D for MA, 0.2D for FA) enables MA to more readily respond to the presence of charge carriers upon electronic excitations.[236] In those systems, less facile reorientation of FA within nanoplatelets, compared to MA, may result in less effective charge carrier screening and enhanced distortion of crystal lattices. This can also contribute to the inferior stability of n = 2 FAPbBr nanoplatelets. On the other hand, both n = 2 MAPbI and n = 2 FAPbI nanoplatelets have tolerance factors within the range where perovskite structures are stable and this could explain why substituting A-site cation from FA to MA does not significantly affect the photostability of iodide nanoplatelets, unlike bromide counterparts.

3.6. Effects of Oxygen and Water

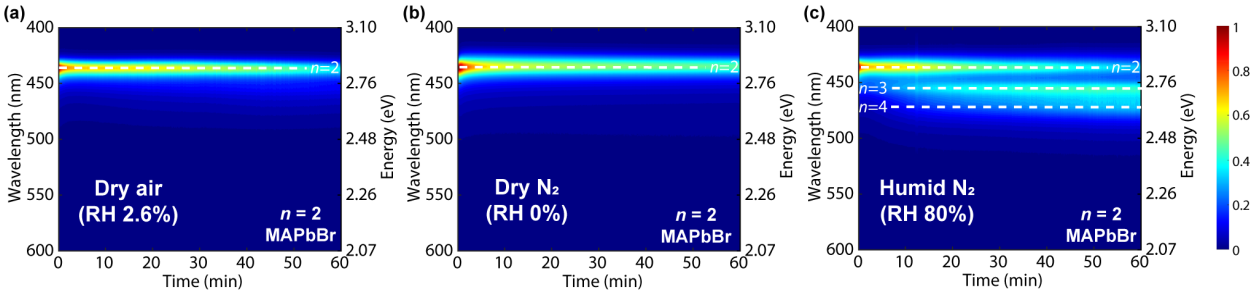

Figure 3.13. Separating the effects of oxygen and moisture. (a-c) Evolution of photoluminescence spectra under UV irradiation (365 nm, 180 mW/cm^2) for colloidal n = 2 MAPbBr nanoplatelets in toluene under dry air, dry N_2 and humid N_2. (White dotted lines indicate the peak positions for nanoplatelets with corresponding thicknesses.)

To identify the external chemical species responsible for the transformation of nanoplatelets into thicker or thinner structures under UV irradiation, I performed the same experiments shown in Figure 3.8 and Figure 3.10 under three different controlled environments: *dry air*, *dry nitrogen*, and *humid nitrogen*. In Figure 3.13a and Figure 3.13b, colloidal n = 2 MAPbBr solutions in toluene were irradiated with UV light (λ = 365 nm, 180 mW/cm^2) while kept under either dry air with 2.6% relative humidity (RH) or dry N_2 with < 0.3 ppm H_2O, respectively. Both data sets show similar photobleaching behavior without significant redshifted emission from thicker structures. In contrast, when the nanoplatelet solution was irradiated under humid N_2 (RH 80%), n = 3 and n = 4 emission appeared within 10 minutes and 20 minutes, respectively (Figure 3.13c). These results confirm that moisture participates in the transformation of nanoplatelets to different-thickness structures, whereas photobleaching occurs regardless of the presence of oxygen or water.

It should be noted that the equilibrium solubility of H_2O in toluene is low (0.0270 mol/L at 25ºC)[237] but its effect, shown in Figure 3.13, is clear. Perovskites are dissolvable in polar solvents, including water, so it is not unexpected that H_2O could assist ion rearrangement within the lattice. Photoexcitation shifts charge density from halide anions to Pb cations,[238] which is believed to weaken hydrogen bonds between halide and alkylammonium ions. Together with deprotonation of alkylammonium ions by water molecules,[239] light and H_2O can act synergistically to accelerate structural transformation in perovskite nanoplatelets.

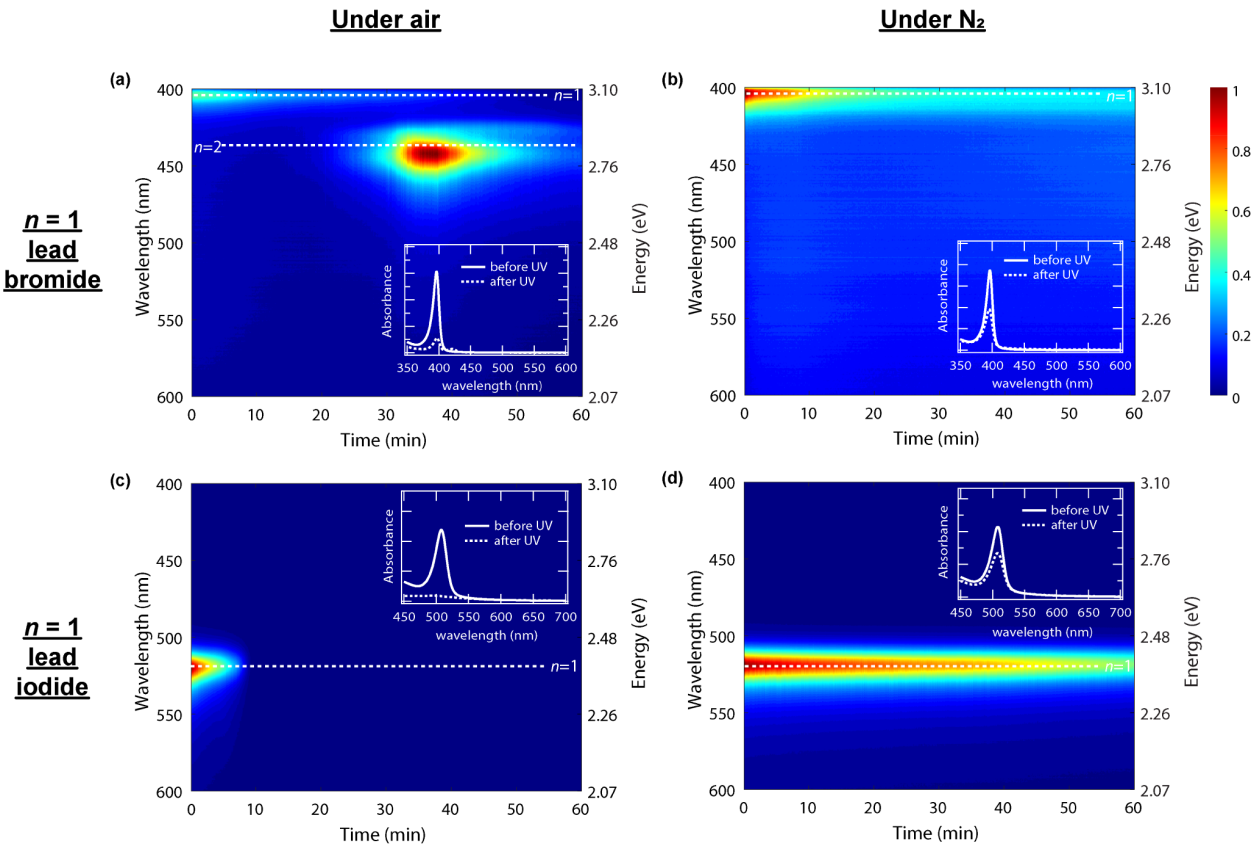

Figure 3.14. (a-d) Evolution of photoluminescence spectra under UV irradiation (365 nm, 180 mW/cm^2) under air and N_2, for colloidal solutions of n = 1 lead bromide and lead iodide nanoplatelets. (White dotted lines indicate the peak positions for nanoplatelets with corresponding thickness and composition.)

n = 1 nanoplatelets also exhibited dramatically enhanced photostability under N_2 atmosphere (Figure 3.14). Although its origin is still unclear, red-shifted emission feature appeared from n = 1 PbBr nanoplatelets when irradiated in air and it was completely suppressed when irradiated in N_2. Photobleaching of both n = 1 PbBr and n = 1 PbI nanoplatelets in solution were also significantly reduced when irradiated under N_2.

3.7. Enhancing the Stability by Adding Excess Ligands

3.7.1. Stability of Colloidal Solution

	MABr	$PbBr_2$	BABr	OABr
Stoichiometric ratio ($L_2[MAPbBr_3]PbBr_4$)	1	2	1	1
'2.5x ligands'	1	2	2.5	2.5
'5x ligands' (Standard procedure for *n* = 2 NPLs)	1	2	5	5
'10x ligands'	1	2	10	10

Table 3.2. Formulations for *n* = 2 MAPbBr nanoplatelets (NPLs) with varied amounts of ligands. Numbers indicate the volumetric ratios of individual precursor solutions (0.2M) in the mixed precursor solutions.

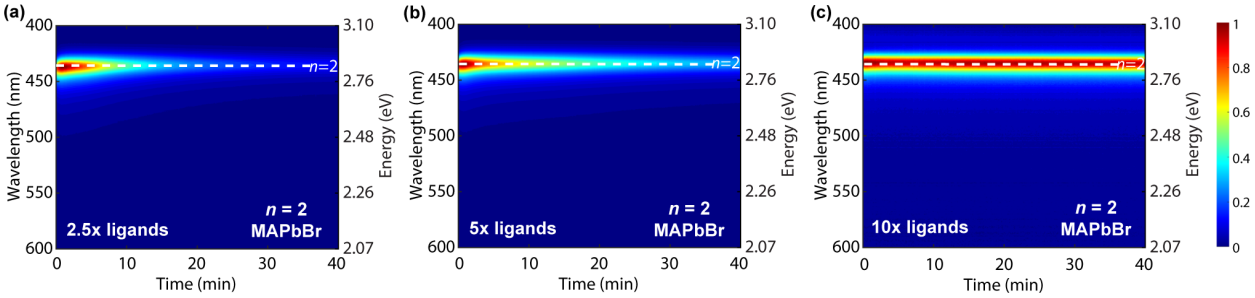

Figure 3.15. Excess ligands improve intrinsic photostability in solution. (a-c) Evolution of photoluminescence spectra under UV irradiation (365 nm, 180 mW/cm^2) for colloidal *n* = 2 MAPbBr nanoplatelets in toluene with varied amounts of excess ligands under N_2. (White dotted lines indicate the peak positions for *n* = 2 MAPbBr nanoplatelets.)

The effect of adding excess alkylammonium ligands was investigated as a strategy for improving nanoplatelet photostability.[142] Three *n* = 2 MAPbBr nanoplatelet solutions were prepared with different relative amounts of alkylammonium bromide ligands in mixed precursor solutions (Table 3.2). As shown in Figure 3.15, the extent of photobleaching was reduced as greater ligand excess was added to the mixed precursor solution (Figure 3.15a-c) without causing any noticeable change in two-dimensional nanoplatelet morphology (Figure 3.1f & Figure 3.16). Furthermore, colloidal *n* = 2 MAPbBr nanoplatelets synthesized with 10x ligands showed remarkable photostability, preserving 95% of PL intensity even after 40 minutes of intense UV irradiation under N_2. This effect is attributed to two factors: 1) more saturated surface coverage in the presence of excess alkylammonium ligands, given the dynamic nature of ligand binding in perovskite nanocrystals,[240] and 2) increased structural robustness of perovskite layers in the presence of excess bromide ions,[142, 148] which prevents the formation of harmful bromide defect

vacancies.[241] Interestingly, no significant enhancement in PLQY was observed with ligand excess (Figure 3.17), unlike several previous reports[142, 148] where stability enhancement was accompanied by PLQY increase.

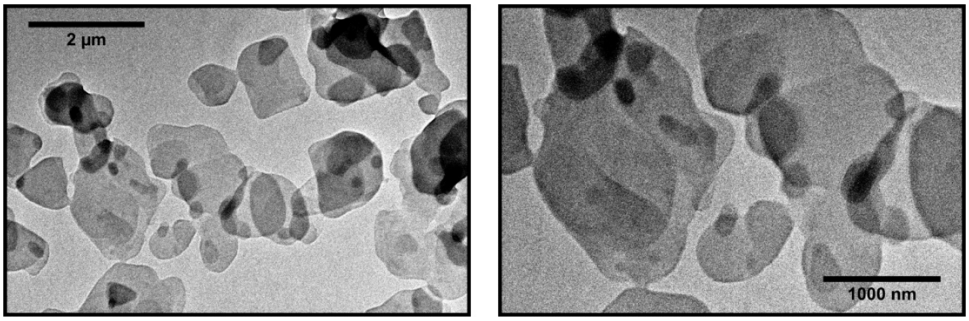

Figure 3.16. TEM images of n = 2 MAPbBr 10x ligands nanoplatelets.

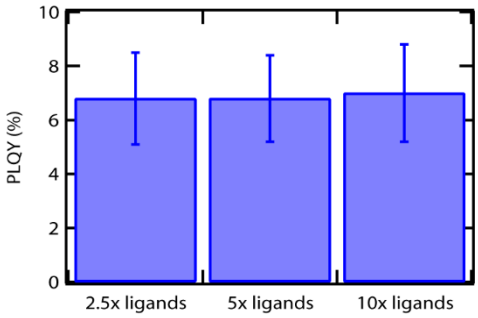

Figure 3.17. Photoluminescence quantum yield (PLQY) of as-synthesized n = 2 MAPbBr nanoplatelet solutions with different amount of ligands.

3.7.2. Stability of Dropcast Film

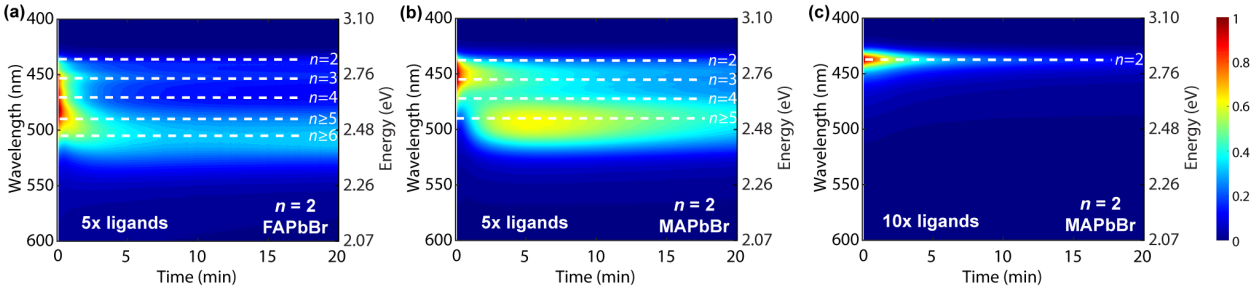

Figure 3.18. Excess ligands suppress transformation in thin films. Evolution of photoluminescence spectra under UV irradiation (365 nm, 120 mW/cm^2) in air for (a) n = 2 FAPbBr 5x ligands film (b) n = 2 MAPbBr 5x ligands film (c) n = 2 MAPbBr 10x ligands film (White dotted lines indicate the peak positions for nanoplatelets with corresponding thicknesses.)

Ligand excess was also found to improve the stability of dropcast nanoplatelet films. Obtaining pure n = 2 deep-blue emission from dropcast n = 2 MAPbBr nanoplatelets synthesized by the reprecipitation method is challenging in general. To prepare dropcast nanoplatelet films, the colloidal nanoplatelet dispersion is centrifuged, redispersed, dropcasted and dried – processes that can induce transformation and degradation. Furthermore, efficient energy transfer within nanoplatelet films along with higher PLQY of thicker nanoplatelets can amplify the contribution of minority red-shifted structures to the overall photoluminescence spectrum. As shown in Figure 3.18a-b, dropcast films of n = 2 FAPbBr (5x ligands) and n = 2 MAPbBr (5x ligands) showed not only n = 2 emission at 437 nm, but also emission from n = 3 and thicker structures in the initial PL spectrum. Upon further UV irradiation, redshifted emission from bulk-like structures at $\lambda >$ 500 nm dominated the PL spectrum and eventual photobleaching was observed. On the other hand, n = 2 MAPbBr 10x ligand films showed pure n = 2 deep-blue luminescence when dropcast and the PL spectrum did not red-shift over time under UV in air, though photobleaching did occur (Figure 3.18c).

XRD patterns of n = 2 MAPbBr (2.5x ligands) and n = 2 MAPbBr (5x ligands) showed no noticeable change (Figure 3.19) even after irradiation and the appearance of red-shifted emission features. It suggests that thicker structures exist in small amounts and n = 2 nanoplatelets are still the majority, but downhill energy funneling and higher emission efficiency of thicker nanoplatelets make red-shifted emission pronounced.

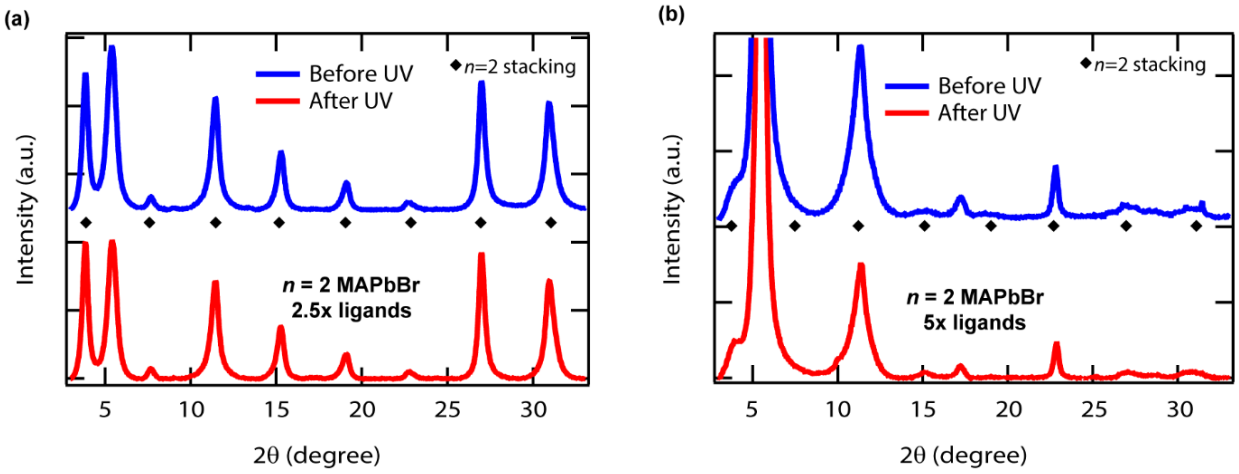

Figure 3.19. X-ray diffraction (XRD) patterns of (a) 2.5x ligands and (b) 5x ligands n = 2 MAPbBr nanoplatelet film before and after UV irradiation in air (180mW/cm^2).

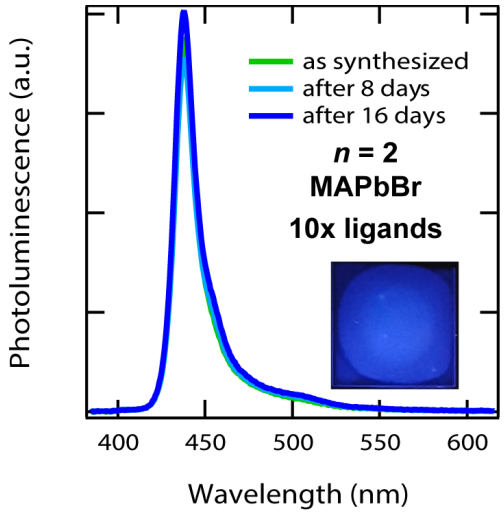

Figure 3.20. Stability of n = 2 MAPbBr 10x ligands film under ambient conditions. (Inset: Image showing deep-blue luminescence from dropcast n = 2 MAPbBr 10x ligands film.)

In addition to improved solution photostability, the dropcast n = 2 MAPbBr 10x ligand film also showed superior stability under ambient conditions as shown in Figure 3.20. Despite small fluctuations between the measurements, deep-blue luminescence from the film essentially maintained its PL intensity for more than two weeks when the film was stored under ambient conditions. Enhanced robustness of the nanoplatelets and a stronger barrier to moisture diffusion through the surface ligand layer are believed to be the key factors for this dramatic stability enhancement. Also, it partially recovered its PL intensity under dark even after intense UV irradiation (Figure 3.21). Although its physical origin is yet not fully understood,[242] self-healing of perovskite nanoplatelets can be highly beneficial to the device lifetime.

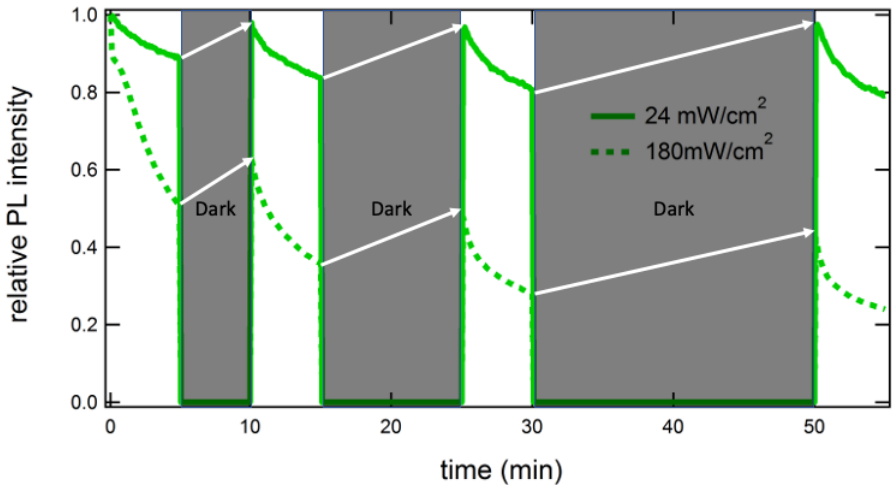

Figure 3.21. Self-healing of n = 2 MAPbBr 10x ligands film under dark after UV (365 nm) irradiation in air.

3.8. Comments on Literatures of Varying Degrees of Nanoplatelet Stability

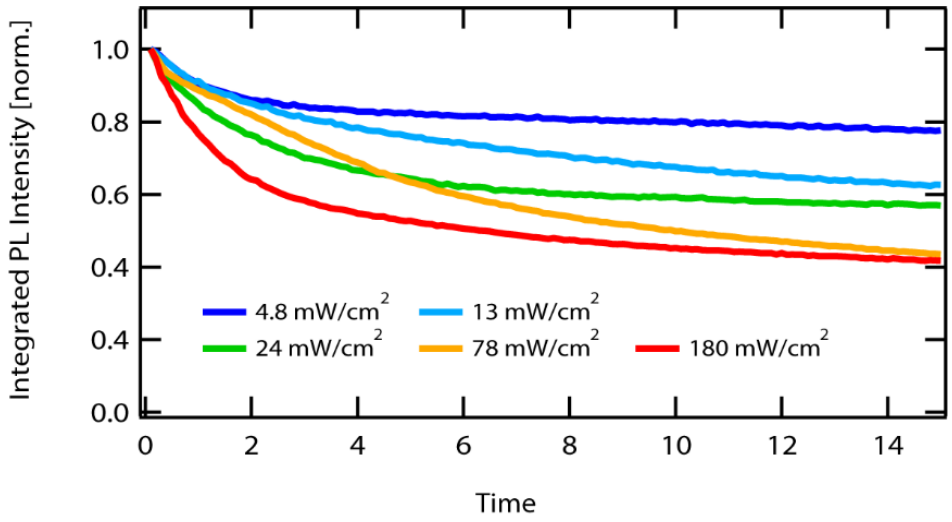

Figure 3.22. Excitation intensity-dependent photobleaching behaviors of n = 2 MAPbBr nanoplatelets (5x ligands) in toluene under N_2 under UV irradiation.

There has been several reports on varying degrees of nanoplatelet stability.[46, 134, 142, 148, 150] As discussed so far, nanoplatelet stability depends not only on intrinsic material properties (cation species, structural robustness, surface ligands coverage, etc.) but also on external factors such as irradiation power density (Figure 3.22), presence of air and relative humidity (Figure 3.8 & 3.10 & 3.13 & 3.14), and synthetic details (Figure 3.15 & 3.18). Lack of those information in the reports can make direct comparison between literatures difficult and I believe collective efforts on reporting those details will accelerate the development of the field.

3.9. Conclusion

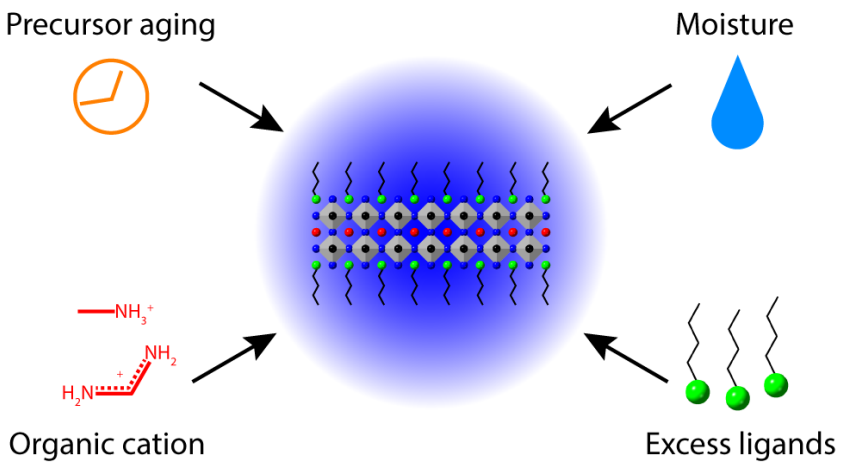

Figure 3.23. Schematic illustration of project summary.

In this work, photostability of colloidal n = 2 methylammonium and formamidinium lead bromide nanoplatelets in toluene solution and in thin film were characterized. Signatures of nanoplatelet degradation, PLQY loss, and transformation into different-thickness structures were identified. Furthermore, it was demonstrated that the usage of freshly prepared precursor solutions, substitution of organic cations, complete isolation from moisture, and the addition of excess alkylammonium bromide ligands can be effective strategies to enhance the photostability of n = 2 lead bromide perovskite nanoplatelets (Figure 3.23). By applying those tactics, a deep-blue luminescent perovskite nanoplatelet film was prepared which was stable under ambient conditions and did not transform under air and UV exposure. This study expands the understanding of the factors that affect perovskite nanoplatelet photostability and opens up new possibilities for the fabrication of stable perovskite-nanoplatelet-based optoelectronic devices. In future studies, the chemical pathways of nanoplatelet degradation and mechanisms of structural transformation will need to be addressed, along with detailed investigation on how precursor solution aging affects nanoplatelet properties. While I have identified some strategies for improving nanoplatelet stability, further improvement is needed before these materials will become viable in commercial technologies. Several recent reports may shed light on the potential strategies for future studies. 1) Incorporating ligand species that can bind to the nanoplatelet surface more strongly than simple alkylammonium ligands — such as alkylphosphonate ligands[36] or zwitterionic ligands[243] — could

be an effective strategy in thermodynamically stabilizing perovskite nanoplatelets. 2) Post-treatment with $PbBr_2$-ligand solution may repair bromide- or lead-vacancy defects[142] — which can act as degradation centers[235] — and further boost the stability. 3) Providing additional bromide ions during the synthesis (e.g. HBr complex) and driving the reaction equilibrium to intact $PbBr_6^{4-}$ octahedra[148] could be another methodology to construct defect-free perovskite nanoplatelets with improved stability. Meanwhile, it needs to be noted that changing the ligand species or providing additional perovskite constituent species (e.g., $PbBr_2$ or HBr) might potentially disrupt the well-established synthetic protocol and subsequent re-optimization of the protocol may be needed to ensure nanoplatelet monodispersity and tunability.

3.10. Methods

3.10.1. Colloidal Perovskite Nanoplatelet Synthesis

Colloidal perovskite nanoplatelets were synthesized using ligand-assisted reprecipitation method under N_2 atmosphere in a glovebox. Individual precursor solutions were prepared by dissolving precursor salts (AX, BX_2, LX) in anhydrous N,N-dimethylformamide (DMF) at the concentration of 0.2M. $PbBr_2$ was not readily soluble in DMF at room temperature and was heated to 80°C for complete dissolution. 0.55M PbI_2 solution in DMF was commercially available from Sigma-Aldrich, and was diluted to 0.2M for nanoplatelet synthesis. Then individual precursor solutions were mixed in specific ratios for $n = 1$ or $n = 2$ nanoplatelets (Table 3.1). As the ligands, 1:1 mixture of butylammonium and octylammonium was used. Excess of ligands, compared to the stoichiometric ratio ($AX:BX_2:LX=0:1:2$ for $n = 1$ nanoplatelets and $AX:BX_2:LX=1:2:2$ for $n = 2$ nanoplatelets), were used for better surface passivation and thickness control. Finally, 10 µL of mixed precursor solution (To prepare XRD samples, SEM samples and film samples for photostability tests, 100 µL of mixed precursor solution instead of 10 µL was used.) was dropped into 10 mL of toluene under stirring. Although colloidal nanoplatelets started to form instantaneously as evidenced by the change in the colors of the solutions and the emergence of photoluminescence, solution colors kept slightly changing for the next few minutes. Thus, to ensure complete crystallization, solutions were left under stirring for 5 minutes for bromide nanoplatelet solution and 10 minutes for iodide nanoplatelet solutions until no significant change in the colors of the solutions were observed.

3.10.2. Photostability Experiment

Solution: 2.5 mL of as-synthesized colloidal perovskite nanoplatelet solutions were transferred into quartz cuvettes under specified atmospheric conditions and irradiated with continuous-wave UV light from a 365 nm fiber-coupled LED (Thorlabs) at specified intensity, while stirring, with photoluminescence spectra taken every 6 seconds. Absorption spectrum of the solution was measured before and after UV irradiation.

Film: For thin film studies, perovskite nanoplatelets were synthesized in larger quantity by dropping 100 µL of precursor solution into 10 mL toluene. Then, nanoplatelets were centrifuged at 4300 rpm for 10 minutes, redispersed in 100 µL toluene, drop-cast onto glass slides and dried under vacuum. Thin film samples were irradiated by continuous-wave UV light from a 365 nm fiber-coupled LED (Thorlabs) at the specified intensity, with photoluminescence spectra taken every 6 seconds.

Atmosphere control: A vacuum pump and N_2 feed were used to control the atmosphere inside Aldrich AtmosBag, with a water bath and the desiccant (MiniPax absorbent packets) controlling the relative humidity.

3.10.3. Characterization

Photoluminescence spectra (PL): PL spectra were collected using an Avantes fiber-optic spectrometer. 365 nm fiber-coupled LED (Thorlabs) was used to excite samples.

Absorption spectra: Absorption spectra were taken using Cary 5000 UV-vis spectrophotometer.

Photoluminescence quantum yield (PLQY): PLQY measurements were performed using an integrating sphere and Avantes fiber-optic spectrometer.[208] 405 nm laser diode (Thorlabs) was used to excite samples.

Fourier transform infrared spectroscopy (FTIR): FTIR was performed using a Thermo Fisher 6700 FTIR spectrometer. FTIR samples were drop cast onto NaCl (Real Crystal IR samples cards, International Crystal Laboratories). Spectra were background subtracted, normalized and smoothed with 5-point adjacent averaging for comparison.

^{1}H nuclear magnetic resonance (NMR): NMR spectroscopy was performed on a Bruker AVANCE III – 400 NMR spectrometer. NMR samples were prepared by drying aged MABr-DMF solutions

under N_2, then redissolving the residue in deuterated DMF. NMR spectra were normalized with respect to DMF CH peak intensity and analyzed in MNova (v. 12.0.0, Mestrelab Research.)

Transmission electron microscopy (TEM): TEM images were taken using FEI Tecnai G2 Spirit Twin instrument operating at 120kV. TEM samples were prepared by centrifuging nanoplatelets, redispersing in small amounts of toluene (~ 300 μL) and drop-casting onto TEM grids.

Scanning electron microscopy (SEM): SEM images were taken using Zeiss Merlin instrument operating at 5kV. SEM samples were prepared by making large quantity of nanoplatelets by dropping 100 μL of precursor solution into 10 mL toluene, centrifuging nanoplatelets, redispersing in 100 μL toluene and then drop-casting onto silicon wafer substrates.

X-ray diffraction (XRD): XRD was performed using a PANalytical X'Pert Pro operating at 45 kV and 40 mA with a copper radiation source. HighScore Plus software was used to subtract the background. XRD samples were prepared by making large quantity of nanoplatelets by dropping 100 μL of precursor solution into 10 mL toluene, centrifuging nanoplatelets, redispersing in 100 μL toluene and then drop-casting onto glass slides.

X-ray photoelectron spectroscopy (XPS): XPS was performed using a Physical Electronics Versaprobe II. Spectra were charge corrected to put principal C1s peak at 284.8 eV, smoothed and normalized. XPS samples were prepared by centrifuging nanoplatelets, redispersing in small amounts of toluene (~ 30 μL) and drop-casting onto glass slides.

Dynamic light scattering (DLS): DLS was performed using a Wyatt Mobius with a 532nm laser. Measurements averaged 5 acquisitions of 10 seconds each, and autocorrelation curves were fitted using Wyatt Dynamics V7 software. To briefly explain DLS technique, it relates Brownian motion of the colloidal particles to the size of the particles. When light is scattered by the particle, exponential decay profile of scattered intensity autocorrelation depends on the size of the colloidal particle. Smaller particles, which diffuse through solution faster than large particles, show lower correlation between the scattered light intensity at time t and $t+\Delta t$. As a result, intensity autocorrelation decays more rapidly for smaller particles. Thus, exponential decay profile can be

correlated with particle diffusion coefficient, which can then be correlated with particle hydrodynamic radius (Radius of a perfectly spherical particle that diffuses at the same rate as the particle being analyzed.) through Stokes-Einstein equation. The overall colloidal particle size distribution can be obtained by fitting multiple exponential functions to intensity autocorrelation curve.

Chapter 4. Exciton Dynamics in Manganese-Doped Perovskite Nanoplatelets

The basis of this chapter has been submitted for publication as:

Ha, S.K.; Shcherbakov-Wu, W.; Powers, E.R.; Paritmongkol, W.; Tisdale, W.A. "Power-Dependent Photoluminescence Efficiency in Manganese-Doped 2D Hybrid Perovskite Nanoplatelets" *Submitted*

4.1. Project Introduction

Introduction of photoactive dopants – especially manganese (Mn^{2+}) ions with well-defined exciton and spin characteristics – is a widely studied approach for expanding the electronic and optical properties of semiconductor nanocrystal systems.[244-256] Mn-doping in semiconductor nanocrystals introduces photoactive atomic sites into the band structure[250, 252, 253] that can enable novel applications in optoelectronics,[257-260] spintronics,[261-263] and quantum information science.[264] Furthermore, strong quantum-confinement may enhance the coupling between carriers and Mn^{2+} dopants, which can maximize the effect of Mn-doping.[61, 62] Consequently, strongly-confined and brightly emissive semiconductor nanomaterials are desirable host systems for leveraging Mn^{2+} dopant photophysics.

Colloidal perovskite nanoplatelets, which are atomically-thin two-dimensional nanocrystals, are ideal host systems for Mn^{2+} doping. Colloidal perovskite nanoplatelets have a chemical formula of $L_2[ABX_3]_{n-1}BX_4$ (L: alkylammonium (e.g. butylammonium (BA)), A: methylammonium (MA), formamidinium (FA), cesium (Cs), B: lead (Pb), X: chloride (Cl), bromide (Br), iodide (I)) where n indicates the number of BX_6^{4-} octahedral layers in the out-of-plane direction.[138-140, 153] Surface ligands provide colloidal stability as well as confining the growth of the crystal in the out-of-plane direction.[46] Like perovskite quantum dots,[66, 90] perovskite nanoplatelets have been shown to exhibit bright emission without the need for a passivating inorganic shell.[142, 148] Furthermore, perovskite nanoplatelets are very strongly confined in one dimension – in contrast to 0D perovskite nanocrystals, which are typically larger[66, 198, 265] than the exciton Bohr radius[66, 138, 139, 153, 160] and, therefore, weakly confined.[51] Strong quantum- and dielectric-confinement of monodisperse nanoplatelets[46, 60, 138, 140, 142, 167] induces a large blue-shift of the excitonic absorption and emission features by up to 0.7 eV[46, 137] compared to those of bulk perovskites and significant enhancement of the exciton binding energy, reaching magnitudes up to several hundred meV.[86, 137] Since the first reports in 2015,[139, 140, 153, 154] significant improvements in perovskite nanoplatelets have been demonstrated, including PLQY,[142, 148] tunability,[46] and stability.[35, 36] In addition, solution processability combined with anisotropic distribution of dipole moments[63, 172] and large absorption coefficients[266] make colloidal perovskite nanoplatelets even more promising for next-generation applications.

Much progress has already been made on Mn-doping in colloidal perovskite nanoplatelets.[185, 267-271] In 2017, Mir *et al.* demonstrated the synthesis of Mn-doped $CsPbCl_3$ nanoplatelets and observed the enhancement of PLQY from 3% to 20% upon doping.[185] Subsequently, Das Adhikari *et al.* showed that n=1 layered Mn-doped perovskites can be transformed into Mn-doped $CsPbCl_3$ nanoplatelets by thermal treatment in the presence of Cs,[268] and Li *et al*. showed the formation of $CsMnCl_3$ nanoplatelets along with Mn-doped $CsPbCl_3$ nanoplatelets.[270] In addition, Babu *et al*. studied concurrent energy- and electron-transfer dynamics in Mn-doped $CsPbBr_3$ nanoplatelets,[267] while Zhang *et al*.[271] and Gao *et al*.[269] explored the potential of utilizing n=1 Mn-doped nanoplatelets as white light emitters. However, these previous studies exclusively focused on all-inorganic nanoplatelets; Mn-doped nanoplatelets containing an organic A-site cation have not been demonstrated. Furthermore, varying PLQY and relative Mn^{2+} dopant emission intensity across these reports highlights the need for more thorough understanding of Mn-site photophysics and excitonic interactions with the band-edge manifold of states. The synthesis of monodisperse methylammonium- or formamdinium-based hybrid Mn-doped nanoplatelets accompanied by in-depth kinetic studies will provide an opportunity for deeper understanding of intrinsic composition- and thickness-dependent behavior.

In this work, successful synthesis of colloidal two-dimensional Mn-doped organic-inorganic hybrid lead bromide perovskite nanoplatelets $L_2[APb_{1-x}Mn_xBr_3]_{n-1}Pb_{1-x}Mn_xBr_4$ (L: butylammonium (BA), A: methylammonium (MA) or formamidinium (FA), n=1 or 2) by ligand-assisted reprecipitation is demonstrated. Significant enhancement of the photoluminescence quantum yield (PLQY) upon doping is observed, which is attributed to the transfer of excitons from the band edge to the Mn^{2+} dopant state where nonradiative recombination is suppressed. Next, photoluminescence (PL) intensity and PLQY of Mn-doped perovskite nanoplatelets are shown to exhibit strong power dependence, even at low excitation density. I propose a kinetic model that accurately reproduces experimental observations, including transient absorption and emission data. In contrast to other reports of Mn-doped semiconductors, wherein the power-dependent PL has been ascribed to the saturation of the unexcited dopant states[245, 246, 251] or consecutive energy transfer,[244] it is shown that the power dependence observed in Mn-doped perovskite nanoplatelets arises primarily from exciton-exciton annihilation between “free” (band-edge) and Mn-immobilized excitons. Lastly, I show that a concentration-normalized microscopic rate constant for band edge-to-dopant excitation transfer that is ~10x faster in methylammonium-containing

nanoplatelets than in formamidinium-containing nanoplatelets and discuss possible explanations for this phenomenon.

4.2. Synthesis of Colloidal Manganese-Doped Perovskite Nanoplatelets

4.2.1. Synthesis of Mn-doped Perovskite Nanoplatelets with Butylammonium as Ligands

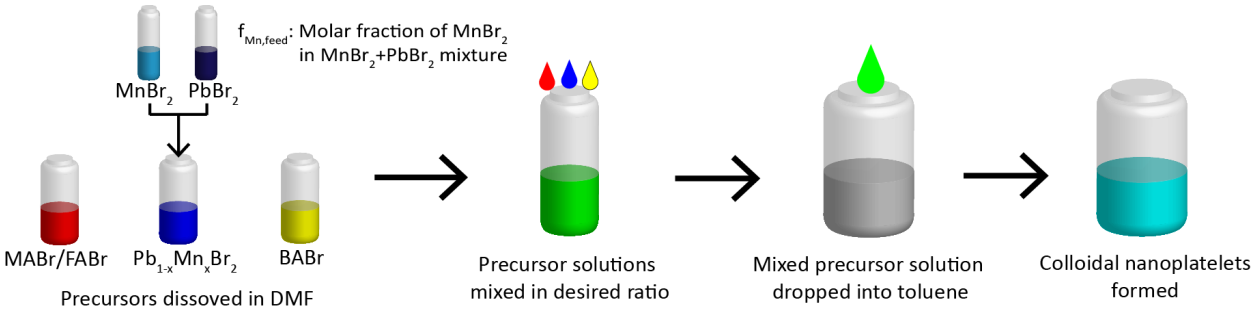

Figure 4.1. Schematic illustration of colloidal Mn-doped perovskite nanoplatelet synthesis.

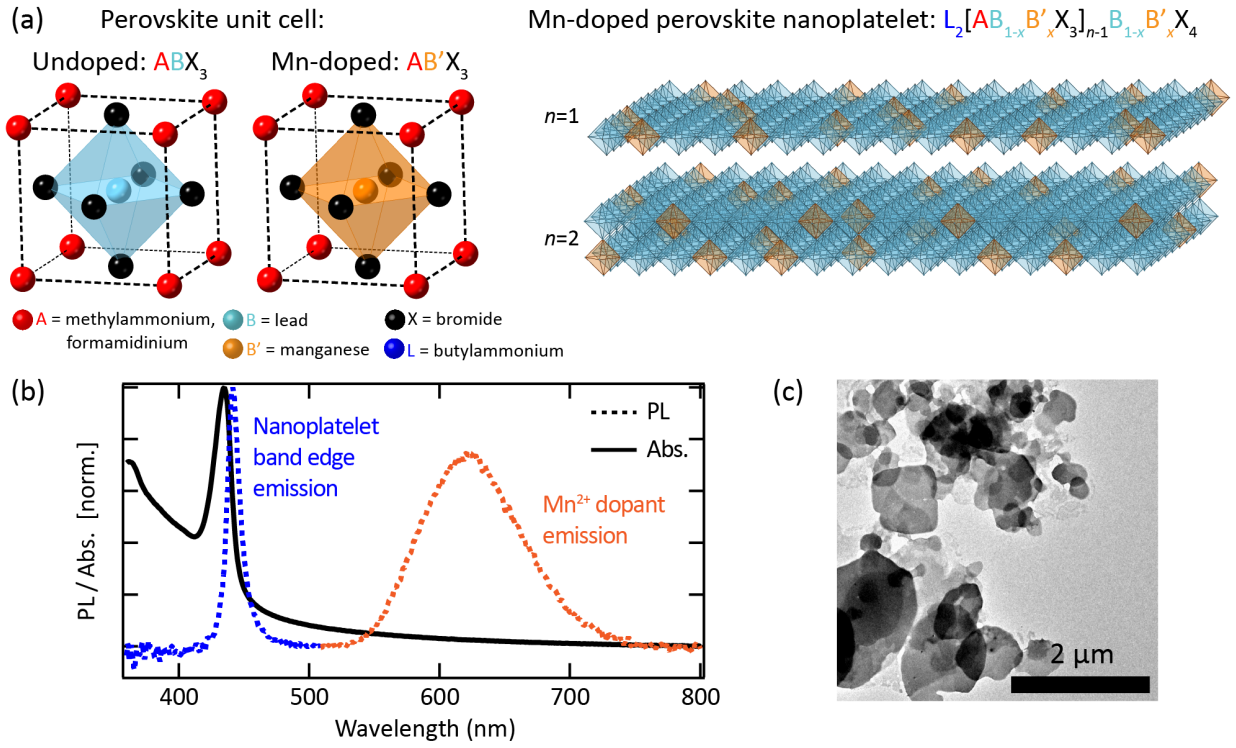

Figure 4.2. Manganese-doped perovskite nanoplatelets. (a) Structures of perovskite unit cell and nanoplatelets. Butylammonium ligands have been omitted for clarity. (b) Photoluminescence and absorption spectra of Mn-doped perovskite nanoplatelets that exhibit simultaneous emission from the nanoplatelet band edge and dopant state. (c) Transmission electron microscopy (TEM) image of Mn-doped perovskite nanoplatelets.

Colloidal Mn-doped organic-inorganic hybrid perovskite nanoplatelets were synthesized via the ligand-assisted reprecipitation method[46, 153, 167] with some modifications (See Figure 4.1 and Methods section for more details). To control the fraction of Mn^{2+} in the resulting nanoplatelets,

the ratio between manganese ions and lead ions in the precursor solution mixture was varied. In this paper, the mole fraction of Mn^{2+} ions in the precursor solution mixture will be referred to as $f_{Mn,feed}$, which differs from the actual mole fraction of Mn^{2+} ions incorporated into the nanoplatelets. Throughout the text, a simplified notation such as n=2 $AB_{1-x}B'_xX$ (x: actual mole fraction of Mn^{2+} in nanoplatelets) will be used to indicate the thickness and composition of the nanoplatelets, rather than the full chemical formula (see Figure 4.2a). In general, it was found that the precursor formulation leading to brightest emission and uniform thickness for Mn-doped nanoplatelets was different from the formulation optimized for non-Mn-containing nanoplatelets (see Chapter 4.2.2). Methylammonium (MA) or formamidinium (FA) were used as A-site organic cations and butylammonium (BA) was used as the surface-bound ligand, as illustrated in Figure 4.2a. A mixture of Pb^{2+} and Mn^{2+} were used as the B-site divalent metal cations and Br^- was used as the halide anion species.

Mn-doping in perovskites occurs as substitutional doping wherein manganese ions replace lead ions.[250] Introduction of the photoactive Mn^{2+} dopant induced a characteristic dopant emission[250, 272-274] centered around $\lambda \approx 610$ nm in addition to the usual band edge emission (Figure 4.2b), and the resulting nanostructures exhibited a 2D shape characteristic of colloidal perovskite nanoplatelets (Figure 4.2c).

4.2.2. Importance of Ligand Choice

(a)

	MABr	$PbBr_2$	$MnBr_2$	BABr	OABr
Formulation 1	1	1	1	2.5	2.5
Formulation 2	1	1	1	4	4
Formulation 3	1	1	1	5	5

(b)

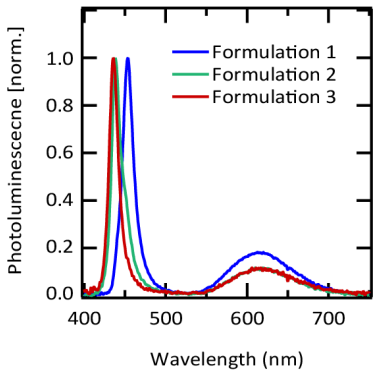

Figure 4.3. Achieving thickness homogeneity of Mn-doped n=2 $MAPb_{1-x}Mn_xBr$ nanoplatelets with 1:1 mixture of butylammonium (BA) and octylammonium (OA) as ligands. (a) Molar ratios between constituent species for the synthesis of Mn-doped perovskite nanoplatelets with BA and OA mixed ligands. (b) Photoluminescence spectra of resulting nanoplatelets.

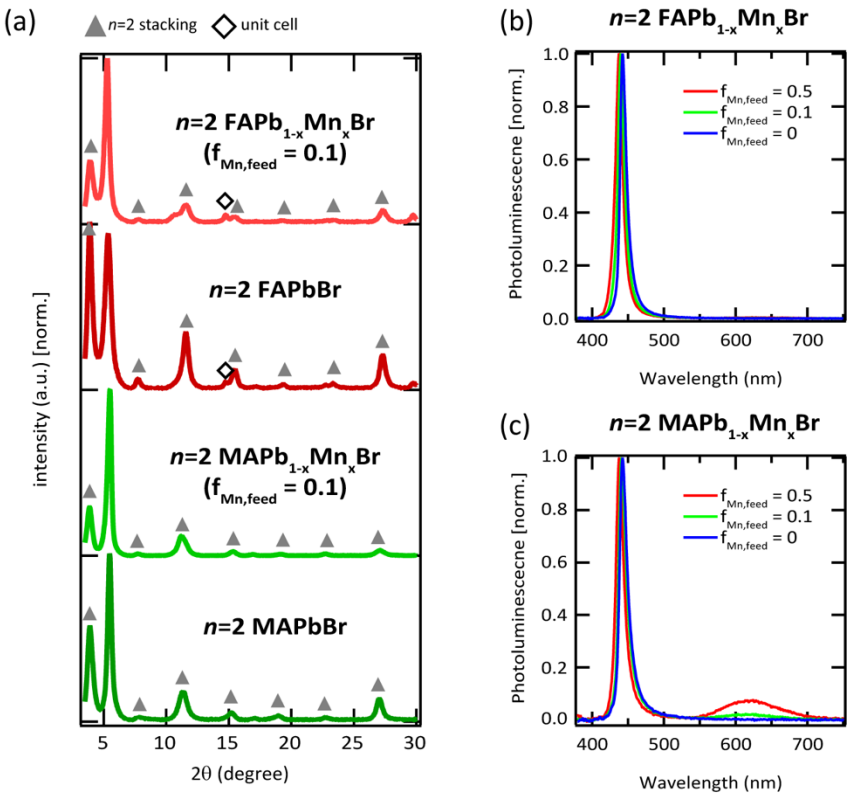

Figure 4.4. Characterization of Mn-doped perovskite nanoplatelets with the mixture of butylammonium (BA) and octylammonium (OA) incorporated as surface ligand species. (a) X-ray diffraction patterns of undoped and doped Mn-doped perovskite nanoplatelets with BA/OA mixture ligands. PL spectra of (b) formamidinium-based and (c) methylammonium-based Mn-doped perovskite nanoplatelets with BA/OA mixed ligands with varying Pb-to-Mn ratio in the precursor solution mixture. Slight shift in emission peak position is believed to be coming from the reabsorption effect.

In this section, the results of Mn-doped perovskite nanoplatelet synthesis with using butylammonium/octylammonium mixture as ligands, instead of pure butylammonium, is shown and the choice of butylammonium as the sole ligand species is justified.

In general, an excess amount of ligand is needed in precursor solution to ensure nanoplatelet thickness homogeneity. For example, as described in the Methods section, AX (MABr or FABr), BX_2 ($Pb_{1-x}Mn_xBr_2$), and LX (BABr) were mixed in 1:2:3 ratio in the precursor solution for the synthesis of n=2 Mn-doped nanoplatelets with butylammonium as ligands. This was because of the formation of $n > 2$ nanoplatelets when the stoichiometric ratio of 1:2:2 was used.[167] When the mixture of butylammonium and octylammonium were incorporated as surface ligands for the synthesis of Mn-doped nanoplatelets, the ratio of AX:BX_2:LX=1:2:10 was needed to suppress the formation of n=3 nanoplatelets (PL emission at ~ 460 nm) as shown in Figure 4.3. However, compared to the PL spectra of butylammonium-capped nanoplatelets shown in Figure 4.2b (and

Figure 4.5 & 4.8 in Chapter 4.3), intensity of the dopant emission from butylammonium/octylammonium-capped nanoplatelets shown in Figure 4.4b-c were significantly less intense. Those results demonstrate that the choice of ligands and the precise engineering of precursor solution formulation is crucial in achieving Mn-doped perovskite nanoplatelet thickness homogeneity and intense dopant emission simultaneously. For this reason, butylammonium was used as the sole ligand species for the rest of this work.

4.3. Characterization of Manganese-doped Perovskite Nanoplatelets

4.3.1. Optical, Structural, and Compositional Characterization

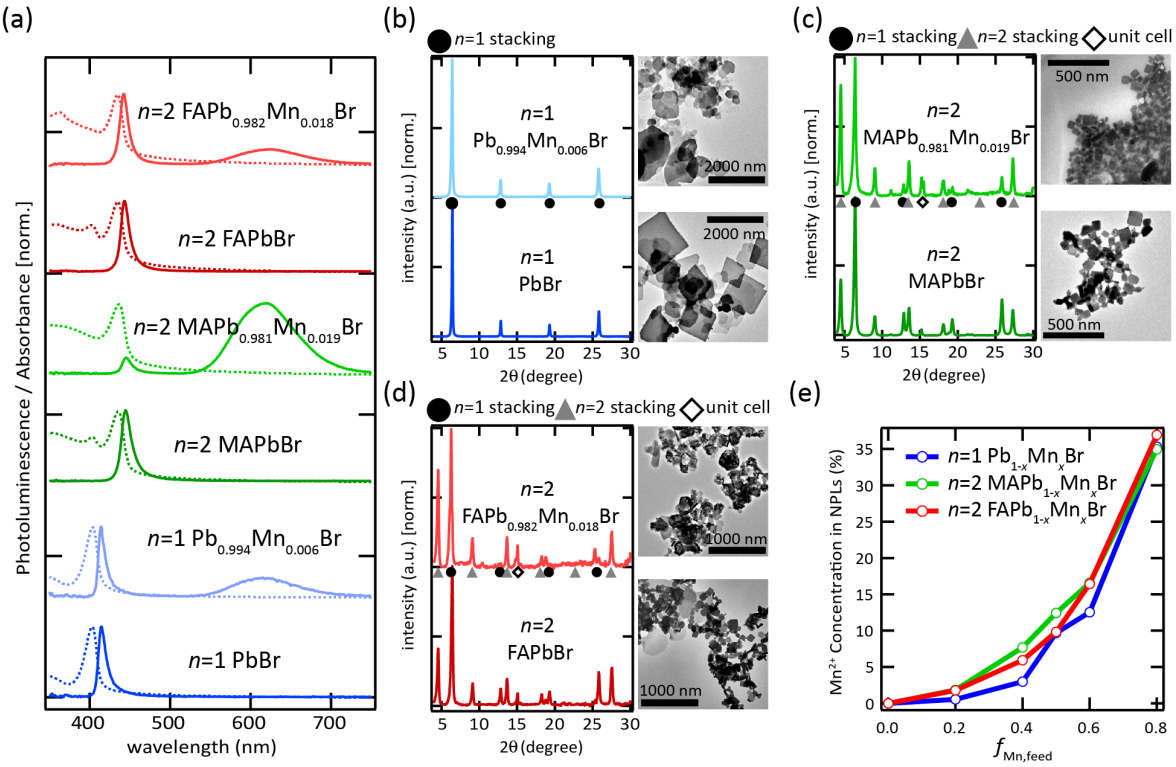

Figure 4.5. Characterization of Mn-doped perovskite nanoplatelets. (a) PL and absorption spectra of undoped and Mn-doped perovskite nanoplatelets. (b-d) X-ray diffraction patterns and transmission electron microscopy images of undoped and doped perovskite nanoplatelets. (e) Experimentally measured dopant fraction in Mn-doped nanoplatelets *vs* Mn fraction in the precursor solution, $f_{\mathrm{Mn,feed}}$.

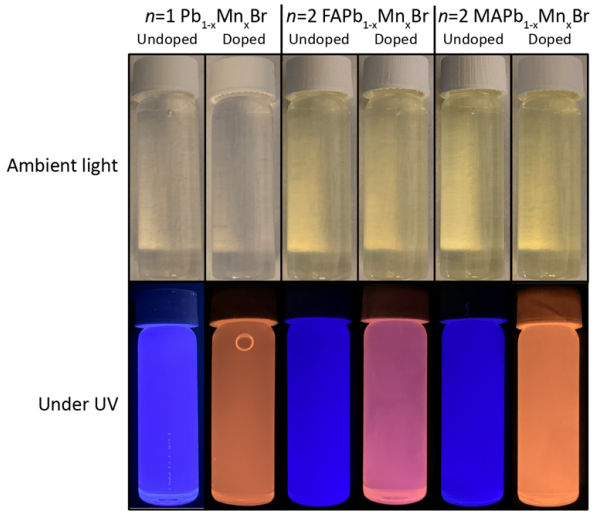

Figure 4.6. Pictures of Mn-doped perovskite nanoplatelet solutions under ambient light and ultraviolet illumination.

3 different families of Mn-doped perovskite nanoplatelets were synthesized for this study: n=1 $Pb_{1-x}Mn_xBr$, n=2 $MAPb_{1-x}Mn_xBr$, and n=2 $FAPb_{1-x}Mn_xBr$. As shown in Figure 4.5a, characteristic broad emission at 610 nm attributed to the Mn^{2+} d-d ($^4T_1 - {}^6A_1$) transition[250] was observed, which changed the overall emission color of the solution from purple or deep blue to orange or pink (Figure 4.6). Mn^{2+} dopant emission has been previously observed between 580-620 nm in different semiconductors,[185, 250, 252, 253, 273, 275-277] with variations attributed to differences in the ligand field environment.[250, 254, 278] No absorption feature associated with the dopant state[272, 273] was observed, presumably due to the low oscillator strength of the spin-forbidden Mn^{2+} d-d transition.[249]

X-ray diffraction (XRD) patterns, shown in Figure 4.5b-d, were dominated by stacking peaks of the two-dimensional (2D) structures. The XRD pattern yielded d-spacings for n=1 and n=2 nanoplatelets of 1.3 nm and 1.9 nm, respectively, which is consistent with the expected perovskite unit cell lattice parameter of 0.6 nm[46, 154, 279] and a butylammonium inter-sheet spacing of approximately 0.7 nm.[46] Randomly overlapping nanoplatelets shown in transmission electron microscopy (TEM) images further confirmed the two-dimensional nature of the particles. XRD patterns indicated the existence of n=1 impurities in n=2 formulations, but n=2 nanoplatelets are expected to be the majority species based on the fact that the n=1 absorption feature at ~ 400 nm is negligible for Mn-doped nanoplatelets, despite a high oscillator strength for the n=1 excitonic resonance.[266]

Sample	$f_{Pb,feed}$	$f_{Mn,feed}$	Pb %	Mn %
n=1 $Pb_{1-x}Mn_xBr$	1	0	100	0
	0.8	0.2	99.4	0.6
	0.6	0.4	97.0	3.0
	0.5	0.5	90.3	9.7
	0.4	0.6	87.5	12.5
	0.2	0.8	64.7	35.3
n=2 $MAPb_{1-x}Mn_xBr$	1	0	100	0
	0.8	0.2	98.1	1.9
	0.6	0.4	92.3	7.7
	0.5	0.5	87.6	12.4
	0.4	0.6	83.4	16.6
	0.2	0.8	65.0	35.0
n=2 $FAPb_{1-x}Mn_xBr$	1	0	100	0
	0.8	0.2	98.2	1.8
	0.6	0.4	94.1	5.9
	0.5	0.5	90.2	9.8
	0.4	0.6	83.6	16.4
	0.2	0.8	63.0	37.0

Table 4.1. Metal cation composition of Mn-doped perovskite nanoplatelets as measured by ICP-OES.

The actual Mn^{2+} dopant fraction in the nanoplatelets, x, was obtained using inductively coupled plasma optical emission spectroscopy (ICP-OES). In Figure 4.5e and Table 4.1, experimentally measured Mn^{2+} fraction is compared to the Mn mole fraction present in the precursor solution, $f_{Mn,feed}$. The Mn^{2+} fraction in the nanoplatelets monotonically increased with $f_{Mn,feed}$, and the trend was similar across all three nanoplatelet families. In general, there was a nonlinear relationship between the feed concentration and the actual dopant concentration in the nanoplatelets. The conversion yield of Pb^{2+} in the nanoplatelet synthesis reaction was above 70% while that of Mn^{2+} ion was 10% or less (Figure 4.7). These observations are consistent with most previous reports that excess Mn^{2+} is needed to achieve Mn-doping in perovskite nanocrystals.[248]

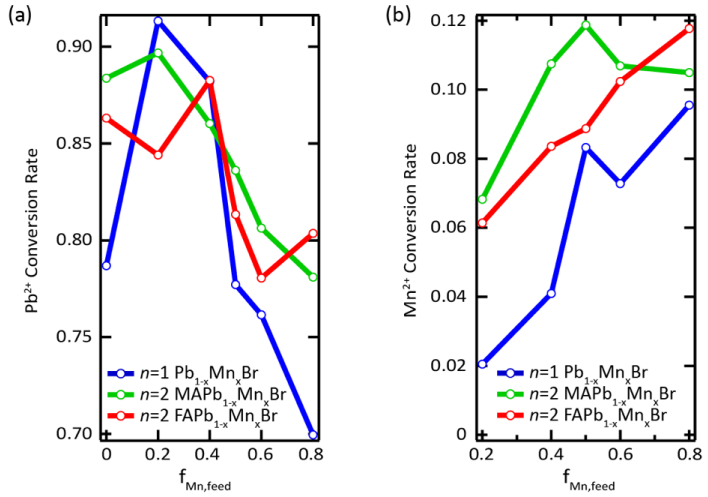

Figure 4.7. Conversion rate of (a) Pb^{2+} and (B) Mn^{2+} calculated by comparing the number of moles added to the precursor solution to the number of moles present in the synthesized nanoplatelets measured by ICP-OES.

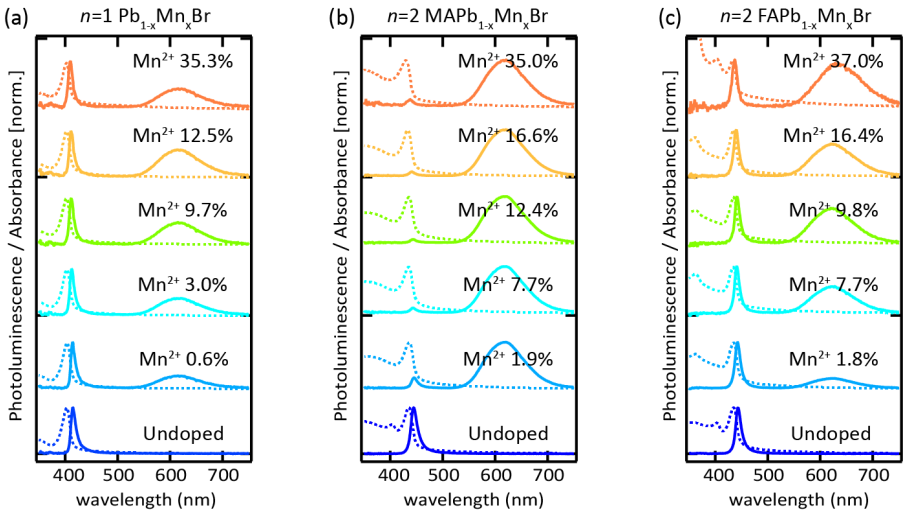

Figure 4.8. Normalized photoluminescence spectra of Mn-doped (a) n=1 $Pb_{1-x}Mn_xBr$, (b) n=2 $MAPb_{1-x}Mn_xBr$, and (c) n=2 $FAPb_{1-x}Mn_xBr$ nanoplatelets with varying $f_{Mn,feed}$.

The relative intensity of the Mn^{2+} dopant emission feature (as compared to the band edge emission) generally increased with increasing dopant fraction in the system (Figure 4.8). Interestingly, the relative intensity of the Mn^{2+} dopant emission was significantly higher in the methylammonium-containing n=2 $MAPb_{1-x}Mn_xBr$ nanoplatelets than in the formamididninum-containing n=2 $FAPb_{1-x}Mn_xBr$ nanoplatelets (Figure 4.5a) at similar dopant fractions (Figure 4.5e). These observations will be addressed in-depth in the later part of Chapter 4.

4.3.2. Photoluminescence Quantum Yields

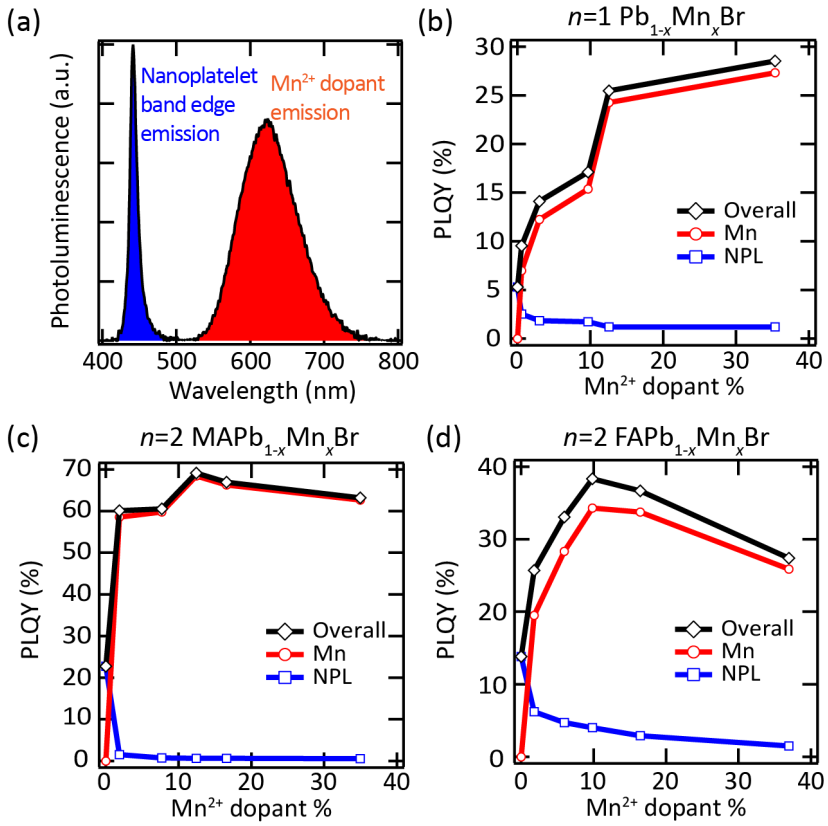

Figure 4.9. Spectrally-resolved photoluminescence quantum yield (PLQY). (a) Exemplary photoluminescence spectrum where nanoplatelet band edge emission and dopant emission can be separately quantified. (b-d) PLQY of the Mn emission feature, nanoplatelet band edge emission feature (NPL), and the overall spectrally-integrated emission of (b) n=1 $Pb_{1-x}Mn_xBr$, (c) n=2 $MAPb_{1-x}Mn_xBr$, and (d) n=2 $FAPb_{1-x}Mn_xBr$ colloidal nanoplatelet dispersions in toluene. All data collected under 365 nm CW (continuous wave) photoexcitation at an incident excitation power of 1.5 mW/cm^2.

Mn-doped nanoplatelets of all compositions exhibited a sharp increase in the overall photoluminescence quantum yield (PLQY) compared to undoped nanoplatelets (Figure 4.9). PLQY was determined using an integrating sphere and a fiber-coupled spectrograph.[208] Since the band edge and dopant emission is spectrally well-resolved (Figure 4.9a), each feature could be separately integrated and quantified. As shown in Figure 4.9b-d, the PLQYs of undoped nanoplatelets were 5%, 23%, and 14% for n=1 PbBr, n=2 MAPbBr, and n=2 FAPbBr nanoplatelets, respectively. Upon Mn-doping, Mn^{2+} dopant PLQY increased dramatically, and the total PLQY of n=2 $MAPb_{0.876}Mn_{0.124}Br$ nanoplatelets ($f_{Mn,feed}$ = 0.5) was observed to be as high as 69% under the same incident excitation intensity of 1.5 mW/cm^2 (PLQY approaching 100% was observed at even lower excitation intensity, see Figure 4.11g-i). Concurrent with the increase in Mn^{2+} emission, a decrease in the band edge emission was observed. This phenomenon was especially pronounced in n=2 $MAPb_{1-x}Mn_xBr$ nanoplatelets (Figure 4.9c), and is the subject of extensive discussion later in this report. For the observed n=1 $Pb_{1-x}Mn_xBr$ nanoplatelets the PLQY increased monotonically with increasing dopant concentration over the entire range studied (Figure 4.9b). However, for n=2 $MAPb_{1-x}Mn_xBr$ and n=2 $FAPb_{1-x}Mn_xBr$ nanoplatelets the PLQY peaked at Mn doping fractions of 12.4% and 9.8%, respectively, then decreased as Mn doping increased (Figure 4.9c-d).

4.3.3. Discussions on Dopant-Induced Strain in Mn-doped Perovskite Nanoplatelets

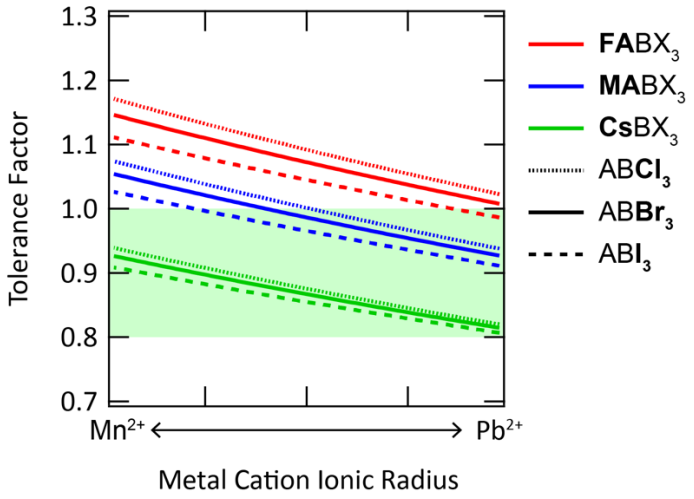

Figure 4.10. Tolerance factor of Mn-doped perovskites with varying organic cations and halide anions. Calculation was performed assuming that Vegard's law[280] holds.

Doping perovskite nanoplatelets with Mn^{2+} ions, which are smaller than Pb^{2+} ions,[250] is expected to induce significant strain in the perovskite structure. The Goldschmidt tolerance factor, defined as $\frac{r_{A-site\ cation}+r_{Halide}}{\sqrt{2}(r_{Metal}+r_{Halide})}$, where r_i indicates the ionic radius of constituent species i, is a commonly used method to predict the structural stability of perovskites.[230] Perovskite structures are preferred when the tolerance factor is between 0.8 and 1, and non-perovskite structures are formed otherwise.[281] Doping lead halide perovskites with Mn^{2+} ions is predicted to eventually destabilize the perovskite structure, depending on the size of the A-site cation (Figure 4.10). This structural destabilization effect is predicted to be most severe in FA-based perovskites (the largest cation) and less severe in perovskites based on the smaller Cs^+ cation (Figure 4.10). While there are multiple reports of Mn-doping in Cs-based perovskite nanomaterials,[185, 257, 267, 270, 272, 273, 277, 282] I am not aware of any reports of Mn-doping in FA-based perovskites. Considering that strain relaxation mostly occurs through the particle surface,[283] 2D perovskites – with intrinsically large surface-to-volume ratio – may be more tolerant to Mn-doping than other topologies.[284] These factors may contribute to the success of Mn-doping in FA-containing perovskite nanoplatelets demonstrated in this work.

Also, I hypothesize that the occurrence of a peak and subsequent decrease in PLQY (Figure 4.9) may be coming from the accumulation of strain and defect formation at higher dopant concentrations. Figure 4.9 shows that PLQY decrease was most significant in n=2 $FAPb_{1-x}Mn_xBr$, less significant in n=2 $FAPb_{1-x}Mn_xBr$ and not observed n=1 $Pb_{1-x}Mn_xBr$ nanoplatelets. This order is consistent with the fact that Mn-doping-induced structural destabilization is expected to be most significant in FA-based perovskites, less significant in MA-based perovskite, and can be insignificant in n=1 nanoplatelets where A-site cations do not exist.

4.4. Excitation Power-Dependent Photoluminescence and Quantum Efficiency

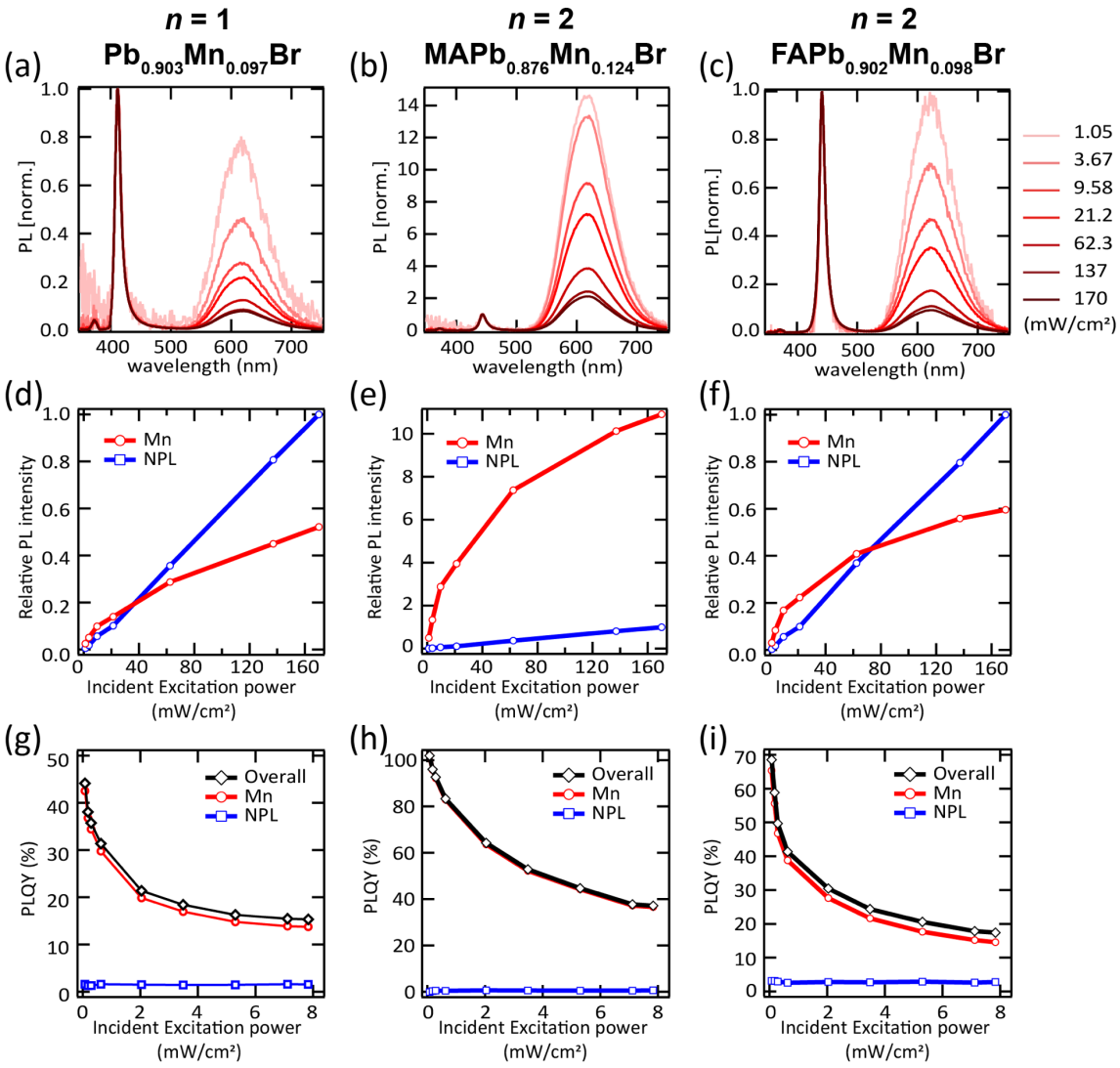

Figure 4.11. Excitation power dependence. (a-c) Photoluminescence spectra; (d-f) separately integrated intensity of nanoplatelet band-edge emission (blue) and Mn^{2+} dopant site emission (red); (g-i) photoluminescence quantum yields (PLQY) of n=1 $Pb_{0.903}Mn_{0.097}Br$, n=2 $MAPb_{0.876}Mn_{0.124}Br$, and n=2 $FAPb_{0.902}Mn_{0.098}Br$ nanoplatelets, respectively.

The overall photoluminescence spectrum was observed to depend strongly on the incident excitation power used (Figure 4.11a-c & 4.12a-c). Relative to the band edge emission, the dopant emission was most intense at low excitation intensities. When the spectrally-integrated steady-state PL intensity is plotted against excitation power, it was observed that the band edge emission increases nearly linearly, while the dopant emission increases sub-linearly (Figure 4.11d-f & Figure 4.12d-f). In other words, the rate of exciton recombination events at the band edge is

proportional to the laser excitation rate, whereas exciton recombination at Mn^{2+} dopant sites is not. This phenomenon can be quantified through the power-dependent PLQY (Figure 4.11g-i). As shown by the blue curve in Figure 4.11g-i, the band edge PLQY stayed constant at a value <5% throughout the excitation power range explored, while the dopant PLQY decreased monotonically with increasing excitation power. This power dependence of dopant emission efficiency persisted down to the lowest incident powers that were experimentally accessible, ~100 μW/cm^2. At these lowest excitation powers, the Mn^{2+} dopant emission feature reached nearly 100% PLQY in *n*=2 $MAPb_{0.876}Mn_{0.124}Br$ nanoplatelets, indicating that the intrinsic internal quantum efficiency of dopant emission is near unity.

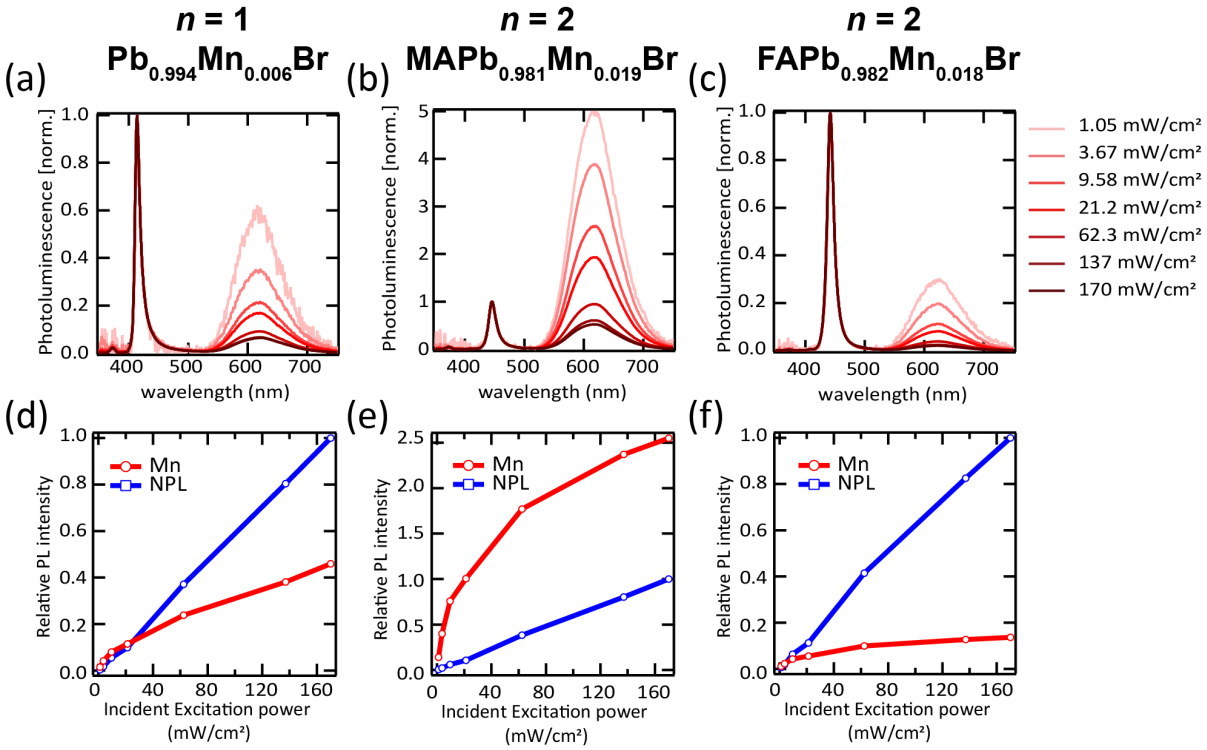

Figure 4.12. Excitation power dependence. (a-c) Photoluminescence spectra; (d-f) separately integrated intensity of nanoplatelet band-edge emission (blue) and Mn^{2+} dopant site emission (red) of *n*=1 $Pb_{0.994}Mn_{0.006}Br$, *n*=2 $MAPb_{0.981}Mn_{0.019}Br$, and *n*=2 $FAPb_{0.982}Mn_{0.018}Br$ nanoplatelets, respectively.

4.5. Kinetic Studies Using Time-Resolved Spectroscopy

4.5.1. Overview of Kinetic Studies

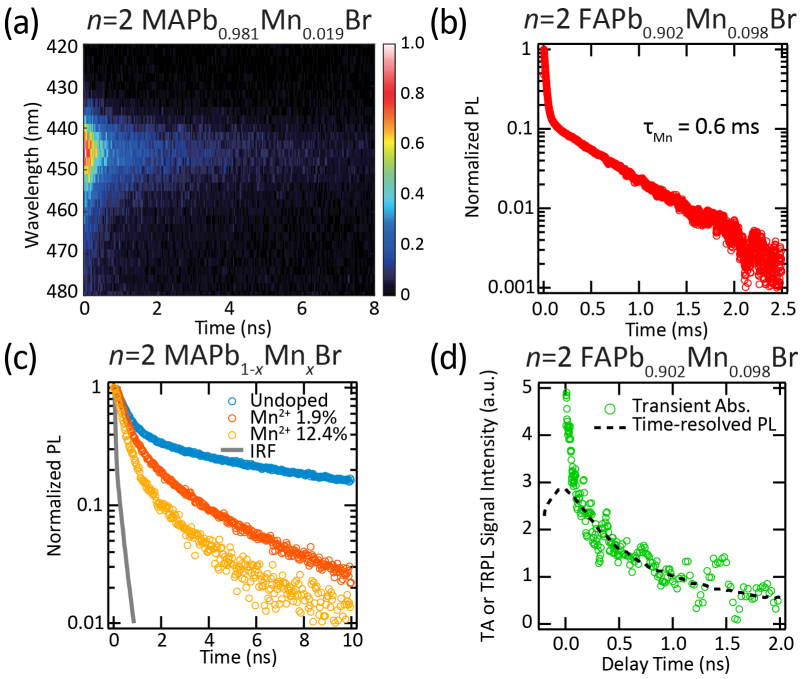

Figure 4.13. Excited state dynamics of Mn-doped perovskite nanoplatelets. (a) Spectrally-resolved photoluminescence (PL) decay of n=2 $MAPb_{0.981}Mn_{0.019}Br$ nanoplatelet band edge emission. (b) Mn-dopant emission dynamics of n=2 $FAPb_{0.902}Mn_{0.098}Br$ nanoplatelets, revealing a ~0.6 ms intrinsic decay time constant for dopant (Mn^{2+}) emission. Early-time fast decay dynamics (< 0.1 ms) are attributed to band-edge emission and multiexciton interactions. (c) Comparison of time-resolved PL (TRPL) dynamics for n=2 $MAPb_{1-x}Mn_xBr$ nanoplatelet band edge emission with different Mn-doping fraction. Instrument response function (IRF) is shown for comparison. (d) Comparison of the band edge bleach transient absorption (TA) signal to the band edge TRPL signal for n=2 $FAPb_{0.902}Mn_{0.098}Br$ nanoplatelets. The two measurements show excellent agreement beyond ~200 ps.

To avoid getting lost in the details of various time-resolved spectroscopic techniques and associated thought processes, I will devote this Chapter 4.5.1 to provide a wider overview of the time-resolved kinetic studies, while occasionally referring to further details presented in Chapter 4.5.2 when necessary.

To obtain an understanding of the fundamental physics behind the observed power dependence, the decay dynamics of band edge and dopant emission were measured using time-resolved photoluminescence (TRPL) and transient absorption (TA) spectroscopy (Figure 4.13). Spectrally-resolved TRPL (Figure 4.13a & 4.14) of Mn-doped nanoplatelets showed notable decay of band edge emission in less than 10 ns (Figure 4.13a), while the dopant emission feature did not show

any appreciable decay in hundreds of nanoseconds (Figure 4.14). Extending the TRPL time window much farther, a 0.6 ms dopant emission lifetime (Figure 4.13b) was resolved, which did not depend on either the nanoplatelet composition or dopant concentration (Figure 4.15). The long dopant emission lifetime is attributed to the spin-forbidden $^4T_1$ – $^6A_1$ atomic transition, in agreement with previous reports.[185, 267, 271, 273]

In undoped nanoplatelets (Figure 4.13c, blue markers), the band edge emission was bi-exponential: approximately 60% of the overall emission intensity decayed within the first 1.5 ns, while the remaining 40% decayed slowly over tens of ns. This behavior is qualitatively similar to observations of prompt and delayed emission in CdSe nanoplatelets.[285] In agreement with the CdSe nanoplatelet literature[285] and in accordance with expectations based on a strongly confined 2D excitonic resonance with strong oscillator strength,[286-288] the initial fast decay is attributed to prompt emission from the band edge exciton and the slower residual decay dynamics to delayed emission by an uncharacterized mechanism (most likely entropically-driven dissociation of band-edge excitons into free carriers[289]). Upon introduction of Mn^{2+} dopants, the prompt emission became faster and the delayed emission became weaker as Mn-doping fraction increased (Figure 4.13c & 4.16). Based on the concurrent observation of decreasing band edge luminescence yield with increasing Mn-doping fraction (Figure 4.9), faster prompt emission decay in doped nanoplatelets is assigned to direct excitation transfer from the band edge to the dopant site – a process that competes kinetically with band edge emission, thereby reducing the overall band edge exciton lifetime. Fitted prompt emission lifetimes of n=2 $MAPb_{1-x}Mn_xBr$ nanoplatelets were 1.35 ns (undoped), 0.95 ns (doped, x = 0.019), and 0.53 ns (doped, x = 0.124). Similarly, prompt emission lifetimes of n=2 $FAPb_{1-x}Mn_xBr$ nanoplatelets were 1.61 ns (undoped), 1.50 ns (doped, x = 0.018), and 1.03 ns (doped, x = 0.098) (Figure 4.16).

The assignment of PL emission dynamics was corroborated using transient absorption (TA) spectroscopy (Figure 4.13d and Figure 4.17). Following initial (< 200 ps) fast multiexciton dynamics in the TA signal (due to higher laser power – see Chapter 4.5.2 for more discussion), the subsequent decay of the band edge TA bleach signal closely matched the decay dynamics measured by TRPL (Figure 4.13d).

Time-resolved spectroscopy results are summarized in Table 4.2. First, all of the change in prompt emission decay upon doping is assigned to excitation transfer from the nanoplatelet band edge to the dopant site, $\Delta k_{prompt} = k_{prompt,doped} - k_{prompt,undoped}$. Subsequently, intrinsic energy transfer

rate constant *per Mn^{2+} site*, k_{trans}, is calculated using the equation $\Delta k_{prompt} = x * k_{trans}$, where x is the Mn-doping fraction. This procedure adjusts the measured dynamics for any differences in the actual dopant concentration, allowing for the comparison of intrinsic rate constants in different material classes. Following this procedure, an intrinsic excitation energy transfer rate constant of ≤ 100 ps in n=2 $MAPb_{1-x}Mn_xBr$ nanoplatelets and ≥ 300 ps in n=2 $FAPb_{1-x}Mn_xBr$ nanoplatelets is extracted. By comparison, inferred intrinsic energy transfer time constants from the band edge to Mn sites in $CsPbCl_3$ quantum dots (QDs) have ranged from ~1 ps to ~15 ps[273, 277, 290] (Table 4.3), which are comparable in magnitude but generally smaller. It is ascribed to the 2D shape of nanoplatelets where the average distance between the dopants must be longer compared to the QDs with the same dopant fractions. In II-VI QDs, intrinsic time constants were mostly < 1 ps,[247, 252, 291] suggesting potentially weaker coupling between the excitons and the dopant in perovskites compared to II-VI hosts.[273, 292]

Sample	**Technique**	$f_{Mn,feed}$	**x**	τ_{prompt} **(ns)**	k_{prompt} **(1/ns)**	Δk_{prompt} **(1/ns)**	k_{trans} **(1/ns)**	τ_{trans} **(ps)**
***n*=2 $MAPb_{1-x}Mn_xBr$**	TRPL	0	0	1.35	0.74	N/A	N/A	N/A
	TRPL	0.2	0.019	0.95	1.05	0.31	16.70	59.89
	TRPL	0.5	0.124	0.53	1.90	1.16	9.36	106.83
***n*=2 $FAPb_{1-x}Mn_xBr$**	TRPL	0	0	1.61	0.62	N/A	N/A	N/A
	TRPL	0.2	0.018	1.50	0.67	0.05	2.73	366.42
	TRPL	0.5	0.098	1.03	0.97	0.35	3.59	278.21
	TA	0.5	0.098	1.29	0.77	0.15	1.57	635.80

Table 4.2. Summary of measured band edge prompt decay constants (k_{prompt}) and the extracted intrinsic rate constant for excitation transfer to Mn^{2+} dopant sites (k_{trans}), based on differences between the prompt decay dynamics in doped and undoped perovskite nanoplatelets.

Host system	**Apparent transfer time const. (ps) (=τ_{trans}/x)**	**Dopant fraction (x)**	**Intrinsic transfer time const. (ps) (=τ_{trans})**	**Ref.**
$CsPb_{1-x}Mn_xCl_3$ QD	380	0.004	1.52	277
$CsPb_{1-x}Mn_xCl_3$ QD	303	0.04	12.12	290
$CsPb_{1-x}Mn_xCl_3$ QD	3600	0.002	7.2	273
$Zn_{1-x}Mn_xSe$/ZnS/CdS/ZnS QD	29	0.0045	0.1305	247
$Zn_{1-x}Mn_xSe$/ZnCdSe QD	< 20	0.01	< 0.2	252

Table 4.3. Examples of previously reported host-to-dopant (Mn^{2+}) excitation transfer time constants.

4.5.2. Details and Interpretation of Time-Resolved Spectroscopy Data

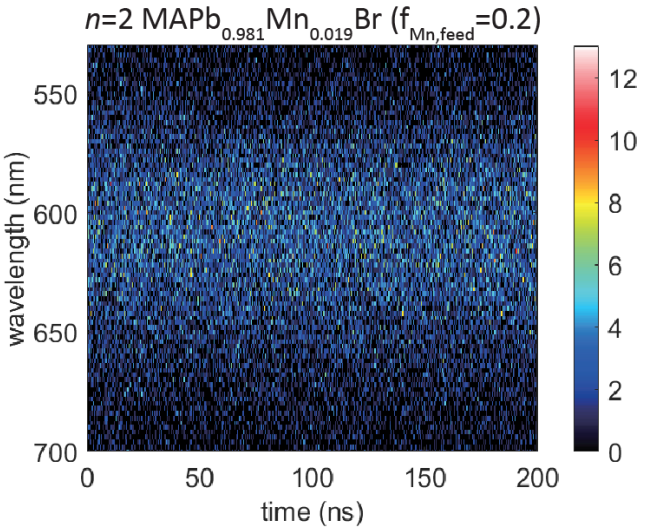

Figure 4.14. Spectrally-resolved time-resolved photoluminescence (TRPL) measurement of dopant emission from *n*=2 $MAPb_{0.981}Mn_{0.019}Br$ nanoplatelets.

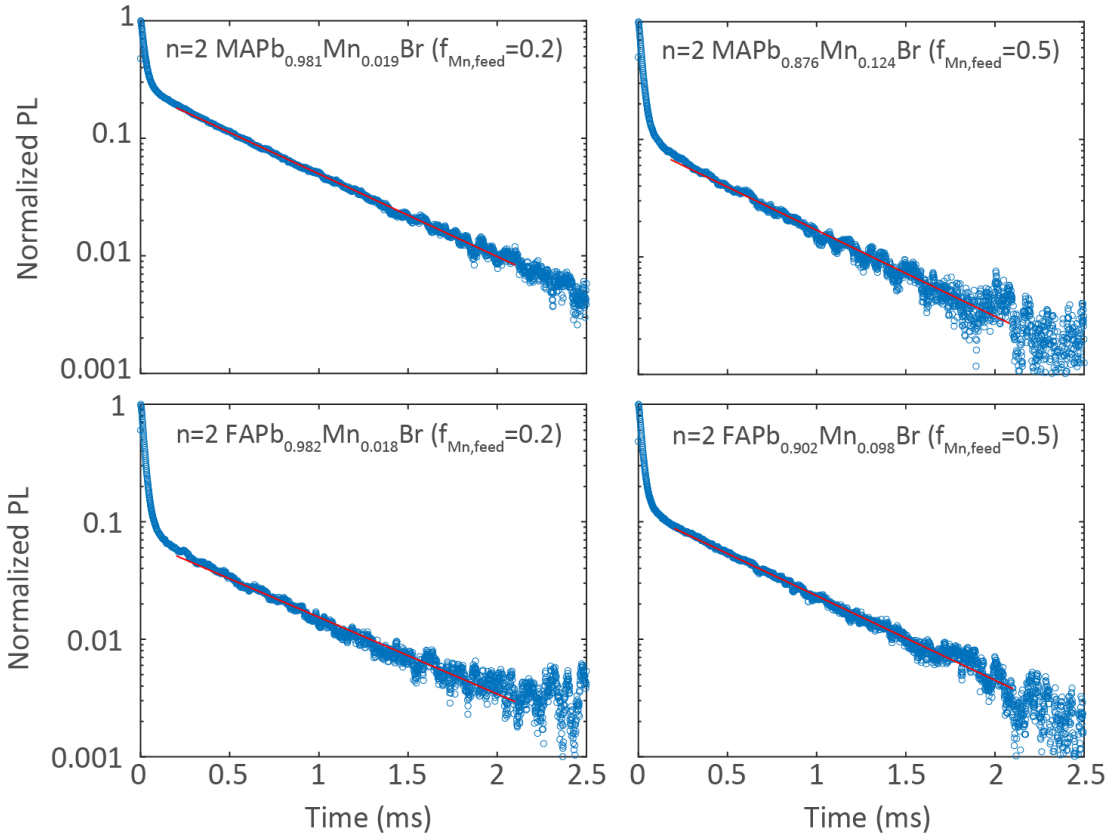

Figure 4.15. PL decay of the dopant (Mn^{2+}) emission. Due to the incapability of spectrally resolving the dopant emission from the band edge emission, initial fast dynamics is attributed to nanoplatelet band edge emission and multiexciton interactions convolved with instrument response function. Red solid lines show the fitted monoexponential curve in t > 0.2 ms regime which were used to obtain the dopant emission lifetime.

TRPL measurements of dopant emission was performed at intense excitation density (Table 4.4). Thus, multiexciton interactions (exciton-exciton annihilation) may have also contributed to the initial fast decay component shown in Figure 4.15 in addition to the band edge emission. Instrument response function must have also contributed to the apparent dynamics of the initial decay.

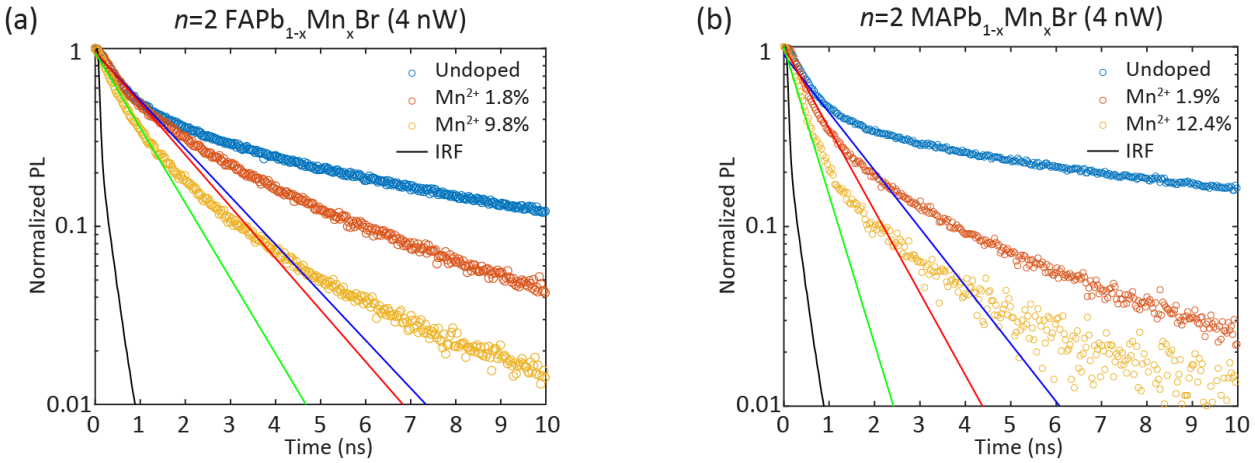

Figure 4.16. Decay dynamics Mn-doped nanoplatelets with varying dopant fractions. (a) n=2 $FAPb_{1-x}Mn_xBr$ and (b) n=2 $MAPb_{1-x}Mn_xBr$ nanoplatelets. Solid curves show monoexponential curves fitted in 0 – 2 ns time window. Instrument Response Function (IRF) curve is drawn for comparison.

Figure 4.16a-b shows multiexponential PL decay in Mn-doped perovskite nanoplatelets. As mentioned in Chapter 4.5.1, monoexponential curve was fitted to the initial decay (0 – 2 ns) to obtain decay rate constants which were used for kinetic model analysis. Among all six species of n=2 $MAPb_{1-x}Mn_xBr$ and n=2 $FAPb_{1-x}Mn_xBr$ nanoplatelets in Figure 4.16, n=2 $MAPb_{0.876}Mn_{0.124}Br$ nanoplatelets exhibited fast band edge decay which is comparable to IRF (Figure 4.16b). Thus, IRF deconvolution was performed on n=2 $MAPb_{1-x}Mn_xBr$ nanoplatelet PL decay curves and solid lines in Figure 4.16 were drawn based on extracted IRF-deconvoluted lifetimes. IRF deconvolution was done using a fluorescence data analysis package called ChiSurf.[293]

Instrument Response Function (IRF) curve in Figure 4.16 were obtained using allura red fluorophore with emission wavelengths ranging from 550 nm to 750 nm.[294] IRF deconvolution is a curve fitting process which can potentially introduce additional errors in extracting PL lifetime. Considering that IRF was also not collected at the exact wavelength of band edge emission (440 nm), I tried to minimize the potential uncertainty that IRF deconvolution process can introduce and decided not to perform IRF deconvolution on n=2 $FAPb_{1-x}Mn_xBr$ PL decay data (Figure 4.16a).

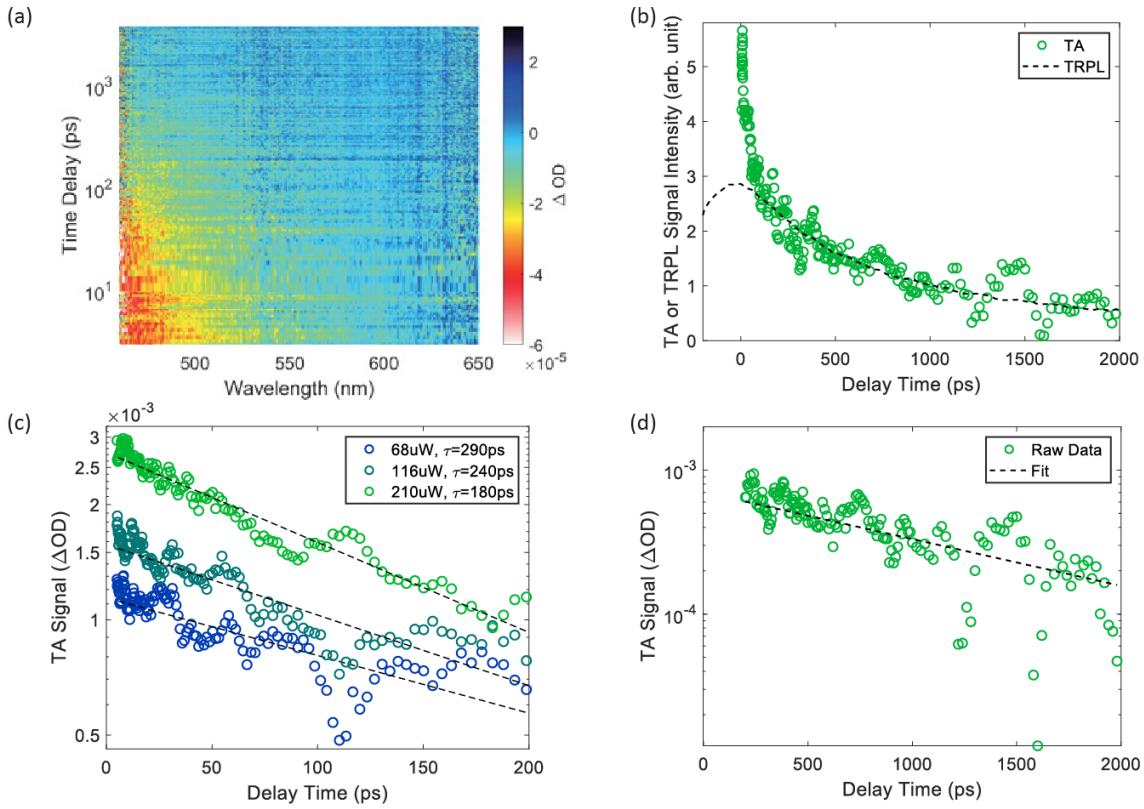

Figure 4.17. Transient absorption (TA) spectroscopy of n=2 $FAPb_{0.902}Mn_{0.098}Br$ nanoplatelets. All TA data were collected using a 425nm pump pulse at a fluence of 200μW unless otherwise noted. The TA decay traces in panels (b), (c), and (d) are averaged over a probe wavelength range of 485-535nm. Decay traces are smoothed using a 5-point rolling average to improve visual clarity; fits were performed on raw (unsmoothed) data. (a) Two-dimensional TA plot showing the decay dynamics of the low-energy tail of the band edge bleach peak. (b) Comparison of the band edge bleach TA signal and TRPL signal decay dynamics showing excellent agreement in decay dynamics after ~200ps where any multi-excitonic interactions and Instrument Response Function (IRF) effect are to be negligible. (c) Fluence-dependent early time TA results showing faster decay dynamics at higher fluences, likely as a result of increased rates of Auger recombination at higher excitation densities. Fits shown are a best-fit single exponential over a 5-200ps time window. (d) TA decay dynamics from panel b fitted with a single exponential decay over a 200-2000ps time window.

TA signal and TRPL of the band edge deviate in 0 – 200 ps region where TA signal exhibit intense fast decay (Figure 4.17b). Figure 4.17c shows that initial fast decay component is fluence-dependent which is an indication that multiexciton interaction is the dominant contributor for the initial decay.

As summarized in Table 4.4 below, excitation photon density per pulse for band edge TRPL was 8 times lower than that for TA measurements. Considering that the absorbance is ~ 1.5 times higher at 425 nm (TA excitation wavelength) than at 405 nm (TRPL excitation wavelength), it is expected that the actual excitation density during TRPL measurement must have been an order-

of-magnitude lower than TA measurements. Thus, fast initial decay observed in TA measurement (Figure 4.17b), which is believed to be coming from multiexciton interactions, is not expected to be an important factor in TRPL measurement. Even though the effect of multiexciton interaction was not completely negligible for band edge TRPL measurements, it must have been buried under IRF and not affected the obtained PL lifetime. Also, time-averaged photon density for power-dependent PL and PLQY measurements were orders-of-magnitude lower as shown in Table 4.4. Thus, the effect of multiexciton interaction that can results in band edge exciton annihilation must have been negligible for those measurements.

Technique	**TRPL (Band edge; ns)**	**TRPL (Dopant; ms)**	**TA**	**Power-dep. PL**	**Power-dep. PLQY**
Power (W)	$4.00*10^{-9}$	$3.00*10^{-3}$	$3.72*10^{-5}$	$5.60*10^{-2}$	$1.20*10^{-3}$
Rep. rate (Hz)	$1.00*10^{6}$	20	$2.00*10^{5}$	Continuous Wave	Continuous Wave
Excitation Wavelength (nm)	405	337	425	365	365
(Effective) Spot size (cm^2)	$> 7.85*10^{-9}$	$> 7.85*10^{-9}$	$5.00*10^{-5}$	1.66 (fitted)	0.3 (fitted)
Pulse energy (J/pulse)	$4.00*10^{-15}$	$1.50*10^{-4}$	$1.86*10^{-10}$	N/A	N/A
Pulse fluence ($J/pulse/cm^2$)	$5.09*10^{-7}$	$1.91*10^{4}$	$3.72*10^{-6}$	N/A	N/A
# photon/pulse	$8.15*10^{3}$	$2.54*10^{14}$	$3.98*10^{8}$	N/A	N/A
Photon density per pulse (#/pulse/cm2)	$1.04*10^{12}$	$3.24*10^{22}$	$7.95*10^{12}$	N/A	N/A
Time-averaged photon density (#/s/cm2)	$1.04*10^{18}$	$6.48*10^{23}$	$1.59*10^{18}$	$6.19*10^{16}$	$7.34*10^{15}$

Table 4.4. Comparison of excitation photon densities between different techniques. Pump overlap fraction for TA measurements were taken into account when calculating power. For fluence dependent TA in panel Figure 4.17c, conditions were slightly different compared to other TA measurements: Their photon densities per pulse was calculated to be 7.7E12, 13E12, 24E12 [photon/cm^2] for 68, 116, 210 μW, respectively. Effective spot size will be explained in Chapter 4.6.2.

4.6. Kinetic Model Analysis

4.6.1. Model without Multiexciton Interaction

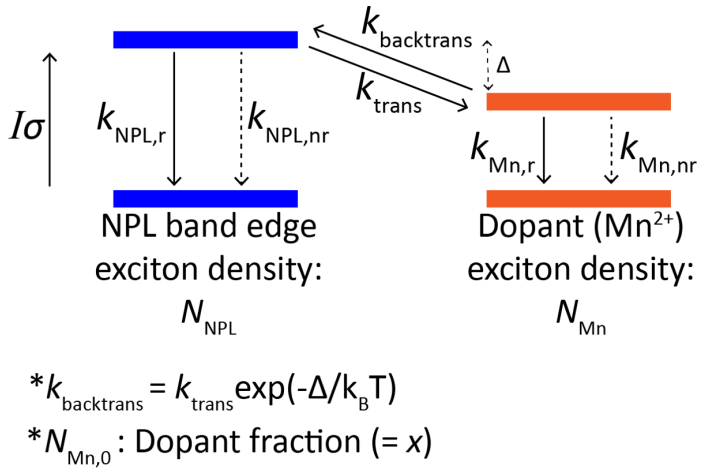

Figure 4.18. Excitonic energy diagram of Mn-doped perovskite nanoplatelets. (N: exciton density; k_r & k_{nr}: radiative and nonradiative recombination rate constants; k_{trans} & $k_{backtrans}$: excitation transfer and back-transfer rate constants; I: effective photon flux; σ: absorption cross section; Δ: energy gap)

Because recombination at dopant sites is ~ 10^6 times slower than recombination at the band edge (Figure 4.13), Mn^{2+} dopants sites may become saturated under CW (continuous wave = not pulsed) excitation, leading to a sub-linear growth in Mn^{2+} emission with increasing excitation power (Figure 4.11 & 4.12).[245, 246, 251] To test this hypothesis, a kinetic model was built to describe the dynamics of band edge and Mn-site excitons and the interaction between these two manifolds of states under steady-state CW excitation (Figure 4.18):

$$\frac{dN_{NPL}}{dt} = 0 = I\sigma - (k_{NPL,r} + k_{NPL,nr})N_{NPL} - k_{trans}N_{Mn,0}(1 - \frac{N_{Mn}}{N_{Mn,0}})N_{NPL} + k_{backtrans}N_{Mn} \quad \dots \quad (4.1a)$$

$$\frac{dN_{Mn}}{dt} = 0 = -(k_{Mn,r} + k_{Mn,nr})N_{Mn} + k_{trans}N_{Mn,0}(1 - \frac{N_{Mn}}{N_{Mn,0}})N_{NPL} - k_{backtrans}N_{Mn} \quad \dots \quad (4.1a)$$

Here, N refers to an excitation density [*per unit cell*]; k_r and k_{nr} are radiative and nonradiative recombination rate constants, respectively [s^{-1}]; k_{trans} is the band edge-to-dopant excitation transfer

rate constant [s^{-1}]; $k_{backtrans}$ is the back-transfer rate constant [s^{-1}]; I is the effective excitation photon flux [cm^{-2} s^{-1}]; σ is absorption cross section [cm^2], and Δ is energy difference between band edge and Mn-site excitations. $N_{Mn,0}$ is the number of dopant sites per unit cell (= x), N_{Mn} is the number of occupied Mn sites [per unit cell], and N_{NPL} is the number of nanoplatelet band edge excitons [per unit cell]. Accordingly, the term $(1 - \frac{N_{Mn}}{N_{Mn,0}})$ represents the fraction of dopant sites that are *unoccupied*, allowing saturation effects to be considered. Eq. 4.1 assumes that all rate constants are independent of dopant fraction and that multiexciton interactions are not important. Key parameters in the model were obtained experimentally using time-resolved spectroscopy, linear absorption, and ICP-OES (See Methods section and Table 4.5 & 4.6). The only unknown parameter in Eq. 4.1 is k_{trans}; all other terms could be independently measured.

The steady-state populations N_{NPL} and N_{Mn} were obtained by solving Eq. 4.1, and the relative PL intensities of the band edge and the dopant emission were predicted by calculating the quantities $k_{NPL,r}N_{NPL}$ and $k_{Mn,r}N_{Mn}$, respectively, and normalizing each by the maximum band edge emission rate (see, for example, Figure 4.11d-f & 4.12d-f). Similarly, band edge and dopant PLQY were predicted by computing $\frac{k_{NPL,r}N_{NPL}}{I\sigma}$ and $\frac{k_{Mn,r}N_{Mn}}{I\sigma}$ (see, for example, Figure 4.11g-i).

The strongest dopant site saturation effects will be observed when the rate of excitation transfer from the band edge to Mn^{2+} sites is much faster than the rate of prompt recombination at the band edge – such that all excitons are transferred to Mn2+ sites with 100% efficiency. In this limit, Eq. 4.1 reduces simply to $I\sigma = k_{Mn,r}N_{Mn}$. This intuitively simple expression states that, at steady state, the occupied Mn site density reaches a value such that the photoexcitation rate is balanced exactly by Mn-site exciton recombination, $N_{Mn} = I\sigma/k_{Mn,r}$. In the experiments, $I < 10^{17}$ cm^{-2} s^{-1}, $\sigma \approx 10^{-17}$ cm^2 (per unit cell, see Table 4.6), and $k_{Mn,r} \approx 10^3$ s^{-1}, leading to the condition $N_{Mn} < 10^{-3}$. For 10% doping, this means that the fraction of occupied Mn sites is 1% *at most*. The vast majority of the data were collected under orders of magnitude lower excitation intensity, such that the fraction of occupied Mn^{2+} sites is always much less than 1%. This simple estimate is supported by the full numerical simulations (Figure 4.19), which show that the excitation laser power would need to be ~ 400 times larger to account for the PL intensity roll-off observed in Figure 4.11 & 4.12. Consequently, it is concluded that the power-dependent photoluminescence efficiency trend (Figure 4.11) *cannot* be explained by saturation of Mn^{2+} sites; some other power-dependent efficiency loss mechanism must be responsible.

Sample (undoped)	PLQY (%)	τ_{prompt} (ns)	$\tau_{NPL,r}$ (ns)	$\tau_{NPL,nr}$ (ns)
***n*=2 MAPbBr**	23	1.35	5.94	1.75
***n*=2 FAPbBr**	14	1.61	11.64	1.87

Table 4.5. PLQY and radiative/nonradiative lifetimes of undoped *n*=2 nanoplatelets.

Sample	$f_{Mn,feed}$	*x*	Abs. Cross Section (cm^2) per unit cell @ 365nm	Abs. Cross Section (cm^2) per particle @ 365nm (Assuming 50nm lateral dimension)
***n*=2 $MAPb_{1-x}Mn_xBr$**	0	0	1.07E-17	1.48E-13
	0.2	0.019	6.42E-18	8.92E-14
	0.5	0.124	8.58E-18	1.19E-13
n=2 $FAPb_{1-x}Mn_xBr$	0	0	1.17E-17	1.63E-13
	0.2	0.018	1.25E-17	1.73E-13
	0.5	0.098	1.61E-17	2.24E-13

Table 4.6. Experimentally obtained absorption cross sections of Mn-doped perovskite nanoplatelets. Due to the polydispersity of nanoplatelet lateral dimensions, absorption cross section per unit cell was used for downstream analysis. Absorption cross section per particle was calculated under the rough estimate of 50 nm lateral dimension and 0.6 nm lattice parameter, for the purpose of comparison with the existing report.[60]

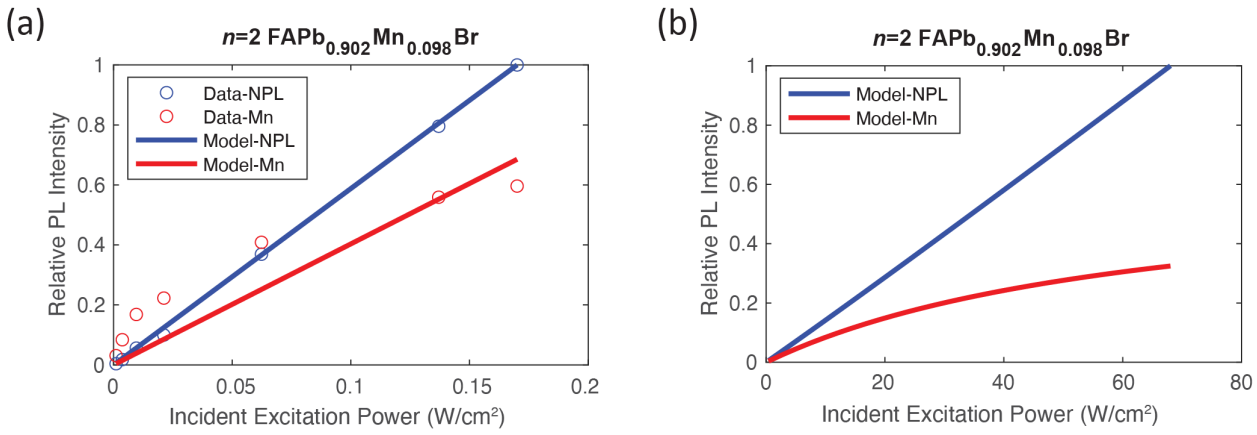

Figure 4.19. Failure of the kinetic model based on the dopant state saturation effect without considering exciton-exciton annihilation. (a) Model simulation under actual experimental conditions. (b) Model simulation under hypothetical 400x higher incident excitation intensity.

4.6.2. Model with Multiexciton Interaction

In Eq. 4.1, it was assumed that multiexciton interactions were negligible. However, this may not always be a valid assumption.[247] To account for this possibility, two types of exciton-exciton annihilation (EEA) interactions were considered: 1) interaction between two mobile excitons at the nanoplatelet band edge ('NPL-NPL EEA'), and 2) interaction between a mobile exciton at the band edge with an immobile exciton at the dopant state ('NPL-Mn EEA'). NPL-NPL EEA is not expected to be a dominant mechanism because of significantly lower steady-state exciton density at the band edge, N_{NPL}, compared to the dopant sites, N_{Mn}, which is explained by the orders-of-magnitude shorter lifetime of band edge excitons compared to Mn-site excitons. NPL-NPL EEA would also lead to power-dependent band edge PLQY, which is not observed experimentally (Figure 4.11g-i). For annihilation events occurring between NPL band edge excitons and Mn-site excitons ('NPL-Mn EEA'), it is expected that the surviving species to be a band-edge exciton due to the much higher density of electronically excited final states that can satisfy momentum conservation during the annihilation event. Annihilation of dopant site excitons, but not band edge excitons, can also rationalize respective linear and sub-linear relationship between excitation power and the band edge and dopant emission intensity (Figure 4.11d-f), respectively. To account for multiexciton interactions, the kinetic model is modified as follows:

$$\frac{dN_{NPL}}{dt} = 0 = I\sigma - (k_{NPL,r} + k_{NPL,nr})N_{NPL} - k_{trans}N_{Mn,0}(1 - \frac{N_{Mn}}{N_{Mn,0}})N_{NPL} + k_{backtrans}N_{Mn} \quad \ldots \quad (4.2a)$$

$$\frac{dN_{Mn}}{dt} = 0 = -(k_{Mn,r} + k_{Mn,nr})N_{Mn} + k_{trans}N_{Mn,0}(1 - \frac{N_{Mn}}{N_{Mn,0}})N_{NPL} - k_{backtrans}N_{Mn} - k_{EEA}N_{Mn}N_{NPL} \quad \ldots \quad (4.2b)$$

The annihilation term appears only in Eq. 4.2b because band edge excitons are neither created nor destroyed during a NPL-Mn EEA event as described in the preceding paragraph. There are two unknown parameters in Eq. 4.2: the excitation transfer rate constant, k_{trans}, and the exciton-exciton annihilation rate constant, k_{EEA}. In practice, more consistent results were obtained if the

effective spot size (which is subsequently used to calculate the effective photon flux *I*) was treated as an additional fitting parameter. Although the incident excitation powers reported in Figure 4.11 & 4.12 were calculated using the measured beam size, an "effective photon flux (*I*)" was used for model analysis for the following reasons. In PLQY measurements, transmitted excitation light can be reflected inside the integrating sphere and hit the sample again. This process is repeated until excitation light gets absorbed by the sample or collected by the detector. Hence the excitation beam can pass through the sample multiple times, which corresponds to the longer beam path length with associated beam attenuation. Thus, a continuous distribution of beam spot sizes exists along this long beam path length and effective spot size in the model equation has to be different from the measured spot size of the excitation beam. In PL measurements, sample was excited inside a 20 mL vial with a relatively long beam path length of ~ 2 cm. Also, its emission spectrum was measured by a detector at 90º angle with the excitation light. This configuration posed a potential complication of penetration-depth-correlated collection efficiency. For example, photons emitted from the center of the vial might have been more effectively collected and contributed more to the measured spectrum than the photons emitted from the edge of the vial, where excitation light first hit the sample. However, photon flux calculated by dividing the measured excitation power with measured spot size reflects the photon flux at the edge of the vial where collection efficiency might have been low. For those reasons, effective spot sizes were treated as fitting parameters. They are expected to be larger than measured spot sizes since they should account for the distribution of spot sizes along the long penetration depth and higher collection efficiency for the photons from less-intensely-excited nanoplatelets. As expected, fitted effective spot sizes (1.6 cm^2 for PL and 0.3 cm^2 for PLQY measurements) were larger than measured spot sizes (0.3 cm^2 for PL and 0.2 cm^2 for PLQY measurements). Also, as shown in Table 4.7, effective spot sizes obtained from fitting were consistent for both PL and PLQY measurements.

As Figure 4.20 shows, modified kinetic model (Eq. 4.2) successfully reproduces the excitation power dependence that was observed experimentally, confirming that NPL-Mn EEA is the primary mechanism responsible for the observed power dependence. Intrinsic excitation transfer time constants obtained through model fitting were 10.1, 8.6, and 16.0 ps for n=2 $MAPb_{1-x}Mn_xBr$ nanoplatelets and 156.0, 264.1, and 398.1 ps for n=2 $FAPb_{1-x}Mn_xBr$ nanoplatelets, respectively (See Table 4.7 for compiled model fitting results). There is variability in the fitted NPL-Mn EEA rate constants (Table 4.7), but they are generally larger than those reported for undoped 2D

perovskites.[266, 295] This makes sense because NPL-NPL EEA occurs between two mobile excitons, whereas the primary multiexciton interaction in Mn-doped perovskite nanoplatelets is the interaction between a free exciton and an immobile exciton. Those EEA rate constants summarized in Table 4.7 are indeed in good agreement with a report on trap-mediated exciton annihilation in 2D transition metal dichalcogenides, which similarly involves the interaction of a freely diffusing exciton in two dimensions with a locally trapped exciton.[296]

Sample	Power-dependent measurement	$f_{Mn,feed}$	$N_{Mn,0}$	k_{trans} (1/ns)	τ_{trans} (ps)	k_{EEA} (cm^2/s) (Assuming 0.6nm lattice constant)	Effective spot size (cm^2)
***n*=2 $MAPb_{1-x}Mn_xBr$**	PLQY	0.5	0.124	55.22	18.11	0.78	0.30
	PL	0.2	0.019	116.57	8.58	0.14	1.52
	PL	0.5	0.124	62.48	16.00	0.23	1.50
***n*=2 $FAPb_{1-x}Mn_xBr$**	PLQY	0.5	0.098	6.41	155.99	0.17	0.30
	PL	0.2	0.018	3.79	264.13	0.03	1.94
	PL	0.5	0.098	2.51	398.13	0.02	1.68

Table 4.7. Summary of model fitting results.

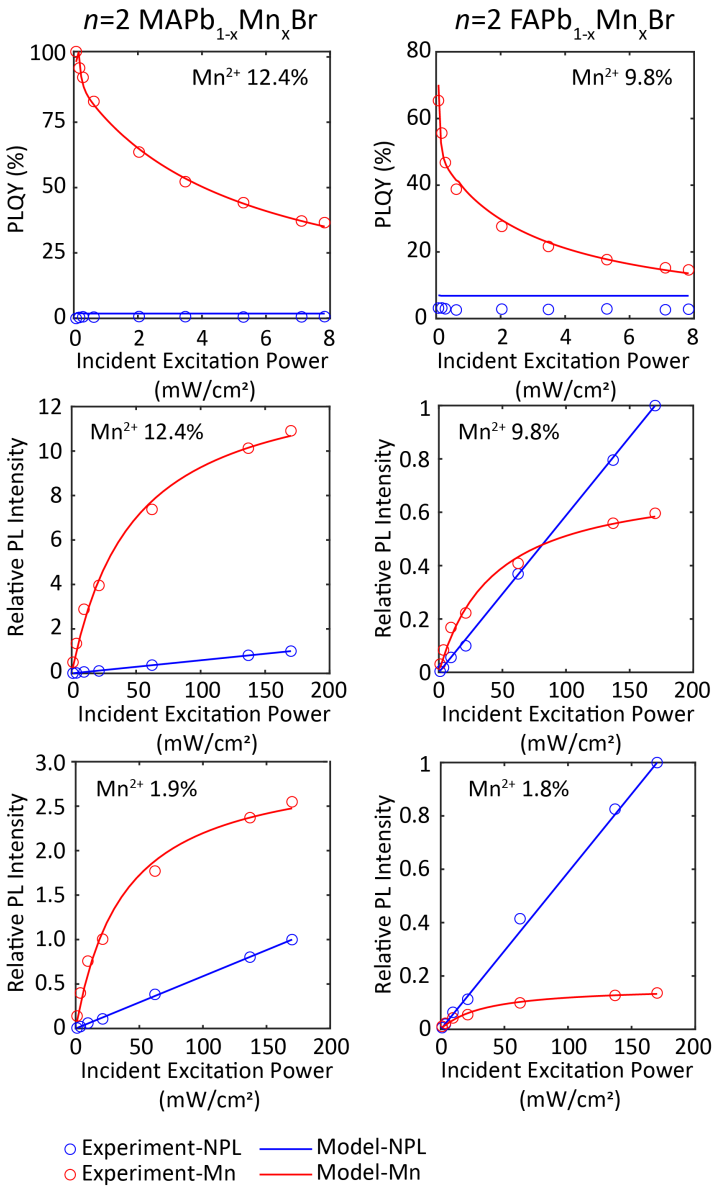

Figure 4.20. Comparison between the experimental data and the model-predicted power dependence when considering exciton-exciton annihilation.

4.7. Comparison of Band Edge-to-Dopant Excitation Transfer Rates

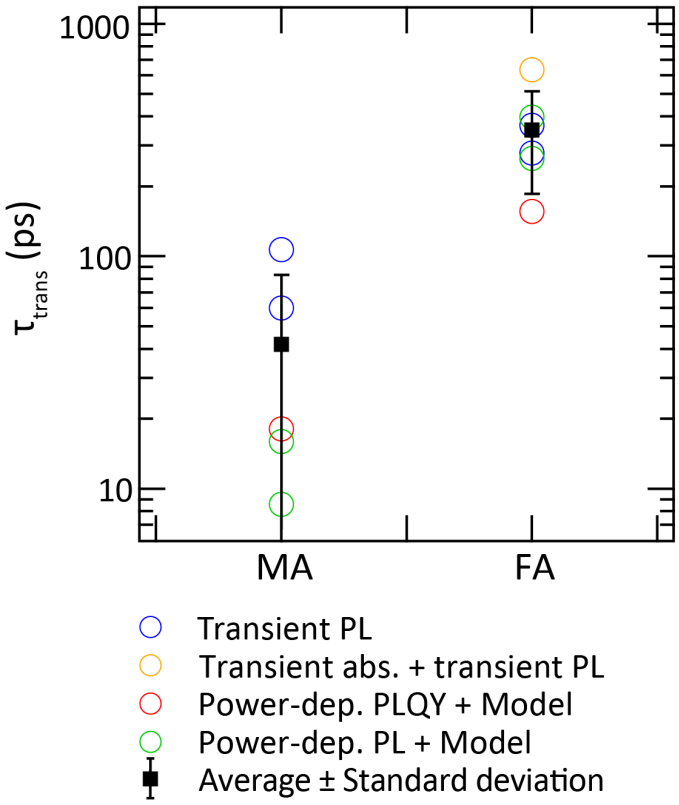

Figure 4.21. Comparison of band edge-to-dopant excitation transfer time constants of n=2 $MAPb_{1-x}Mn_xBr$ nanoplatelets and n=2 $FAPb_{1-x}Mn_xBr$ nanoplatelets obtained by using the methods noted.

Lastly, Figure 4.21 summarizes the obtained excitation transfer time constants and it shows that excitation transfer is noticeably faster in n=2 $MAPb_{1-x}Mn_xBr$ nanoplatelets than in n=2 $FAPb_{1-x}Mn_xBr$ nanoplatelets. This faster excitation transfer explains two previously mentioned observations: 1) more intense dopant emission from n=2 $MAPb_{1-x}Mn_xBr$ nanoplatelets with similar dopant fractions (Figure 4.5), and 2) higher dopant PLQY and lower band edge PLQY of n=2 $MAPb_{1-x}Mn_xBr$ nanoplatelets compared to other nanoplatelet species (Figure 4.9). Although the exact origin of this A-site organic cation-dependent excitation transfer rate is not yet fully understood, a few hypotheses can be proposed. One explanation could be a structural change which is beneficial to band edge-to-dopant excitation transfer. Figure 4.22 compares the XRD peak near $2\theta \approx 15^{\circ}$, which informs on the perovskite unit cell size, in doped and undoped nanoplatelets. A more noticeable lattice contraction upon doping was observed from n=2 $MAPb_{1-x}Mn_xBr$ nanoplatelets, which may be accompanied by octahedral cage rearrangement. Other possible

explanations could include faster excitation transfer through smaller unit cells in *n*=2 $MAPb_{1-x}Mn_xBr$ nanoplatelets or strain-induced dopant segregation[297] in *n*=2 $FAPb_{1-x}Mn_xBr$ nanoplatelets. Understanding the origin of this faster excitation transfer in *n*=2 $MAPb_{1-x}Mn_xBr$ nanoplatelets will be an interesting research direction moving forward.

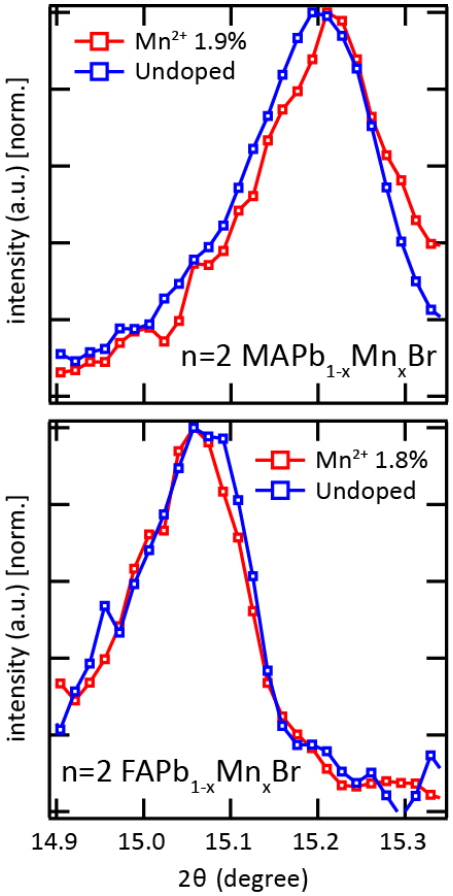

Figure 4.22. Comparison of perovskite unit cell XRD peak shift upon doping in *n*=2 $MAPb_{1-x}Mn_xBr$ and in *n*=2 $FAPb_{1-x}Mn_xBr$ nanoplatelets.

4.8. Power-Dependent Color Tunability and White Light Emission

4.8.1. Excitation Power-Dependent Color Tunability

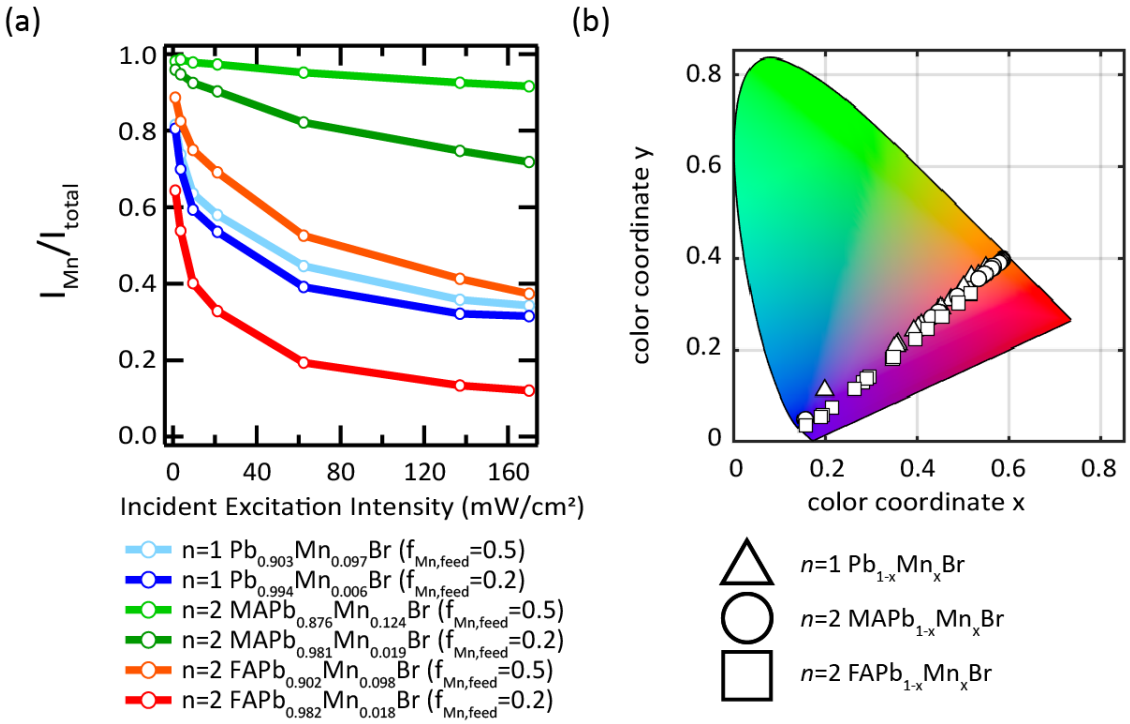

Figure 4.23. Power-dependent color tunability of Mn-doped perovskite nanoplatelets. (a) Fraction of the dopant emission intensity in total emission intensity as a function of excitation power. (b) Color coordinates of Mn-doped perovskite nanoplatelet emissions with varying composition and excitation power.

Change in the relative intensity of Mn^{2+} dopant emission compared to the band edge emission intensity as functions of dopant fraction and excitation power suggests that perceived color of the sample emission also changes accordingly. Figure 4.23a summarized the relative dopant emission intensity and Figure 4.23b shows the color coordinates of the emissions from various Mn-doped perovskite nanoplatelets with varying dopant fractions and excitation powers. Those results clearly demonstrate that the color of the emission from Mn-doped perovskite nanoplatelets can be continuously tuned between deep blue (color of the band edge emission) and orange (color of Mn^{2+} dopant emission).

4.8.2. White Light Emission with a Green Phosphor

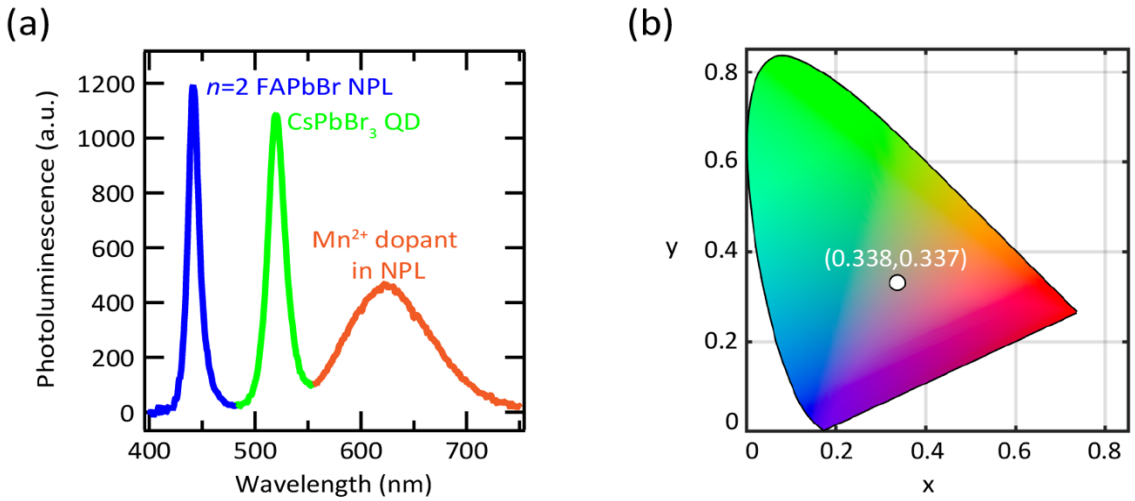

Figure 4.24. Experimental demonstration of ideal white light emission from the solution mixture of Mn-doped perovskite nanoplatelets (n=2 $FAPb_{1-x}Mn_xBr$) and $CsPbBr_3$ quantum dots. (a) Emission spectrum. (b) Color coordinate. (Incident excitation power: 7 mW/cm^2)

Mn-doped perovskite nanoplatelets exhibit deep blue emission from the band edge and orange emission from Mn^{2+} dopant state simultaneously. This dual emission can be utilized to realize white light emission in combination with a green phosphor. Figure 4.24 shows the desirable white light emission from the colloidal solution of Mn-doped perovskite nanoplatelets and $CsPbBr_3$ QD mixture.

4.9. Conclusion

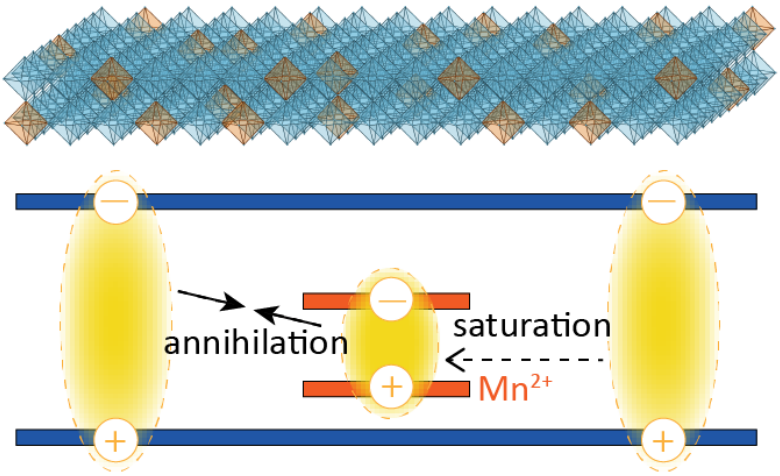

Figure 4.25. Schematic illustration of a Mn-doped perovskite nanoplatelet and its exciton dynamics.

In conclusion, facile synthesis of Mn-doped hybrid perovskite nanoplatelets at room-temperature was demonstrated. Substitutional doping of Mn^{2+} in place of Pb^{2+} introduced a photoactive dopant state in the perovskite nanoplatelet band structure, and band edge-to-dopant excitation transfer resulted in the overall enhancement of PLQY owing to near-unity intrinsic quantum efficiency of the dopant state. It was also demonstrated that emission intensities and PLQYs of Mn-doped perovskite nanoplatelets exhibit strong dependence on excitation power. By combining time-resolved spectroscopy and a kinetic model analysis, the effect of unexcited dopant state saturation was found to be negligible under the given experimental conditions, and that annihilation of Mn-site excitons by band-edge excitons is likely the primary mechanism for the observed power dependence (Figure 4.25). Lastly, it was shown that MA-based nanoplatelets exhibit faster rates of excitation transfer from the band edge to the dopant site than FA-based nanoplatelets. In addition to demonstrating the synthesis of new nanomaterials, this work provides in-depth understanding of exciton dynamics in Mn-doped organic-inorganic hybrid perovskite nanoplatelets, which will be critical to incorporating those materials in next-generation optoelectronic technologies.

4.10. Methods

4.10.1. Mn-Doped Perovskite Nanoplatelet Synthesis

Colloidal Mn-doped perovskite nanoplatelets were synthesized using ligand-assisted reprecipitation method in a glovebox. 0.2M solutions of MABr, FABr, $PbBr_2$, $MnBr_2$, and BABr in N,N-dimethylformamide were prepared. $Pb_{1-x}Mn_xBr_2$ solution was prepared by mixing $PbBr_2$ and $MnBr_2$ solutions with specific ratios (=$f_{Mn,feed}$). Then for n=1 nanoplatelets, $Pb_{1-x}Mn_xBr_2$ and BABr solutions were mixed in a 1:2 ratio. For n=2 nanoplatelets, MABr (or FABr), $Pb_{1-x}Mn_xBr_2$, and BABr solutions were mixed in a 1:2:3 ratio. Then 20 μL of mixed precursor solution was injected into 10 mL toluene under vigorous stirring. Colloidal Mn-doped perovskite nanoplatelets were instantaneously formed.

4.10.2. Characterization

Photoluminescence spectra. A 365 nm fiber-coupled LED (Thorlabs) was used to excite the sample in a 20 mL vial, and PL spectra were collected using an Avantes fiber-coupled spectrometer.

Absorption spectra. Absorption spectra were taken by a Cary 5000 UV-Vis spectrophotometer. A cuvette with a 10-mm path length was used to mount the sample of Mn-doped perovskite nanoplatelets dispersed in toluene.

Photoluminescence quantum yield. PLQY measurements were performed using an integrating sphere and Avantes fiber-optic spectrometer. A 365 nm LED was used to excite samples. PLQYs were calculated by following a previously reported method.[208]

Transmission electron microscopy (TEM). TEM images were taken using a FEI Tecnai G2 Spirit Twin instrument operating at 120 kV.

X-ray diffraction (XRD). XRD was performed using a PANalytical X'Pert Pro operating at 45 kV and 40 mA with a copper radiation source. Background subtraction was done by using HighScore software.

Inductively coupled plasma optical emission spectroscopy (ICP-OES). ICP-OES was performed using Agilent 5100 ICP-OES. Calibration was done using ICP standards from Millipore Sigma. ICP-OES samples were prepared by collecting nanoplatelets after centrifugation and dissolving them in 5 mL of 3% HNO_3 solution.

4.10.3. Time-Resolved Spectroscopy

Band-edge time-resolved photoluminescence (TRPL). Band edge photoluminescence lifetime measurements were performed by time-correlated single-photon counting using a single photon avalanche photodiode (APD) from Micro Photon Devices. The solution sample in a cuvette with a 10-mm path length was placed on the stage of an inverted microscope (Nikon, Ti Eclipse) and excited using a 405 nm pulsed laser diode (LDH-D-C-405M, Picoquant, 1 MHz repetition rate, <0.1 ns pulse duration) with 1 MHz repetition rate. The photoluminescence was collected and passed through a pinhole before being focused onto the APD sensor. Dopant photoluminescence lifetime measurements were performed using a Si Switchable Gain Detector from Thorlabs (PDA36A). The solution sample in a cuvette with 10-mm path length was excited using a 337 nm pulsed laser diode (Stanford NL100 Nitrogen Laser) with 20 Hz repetition rate.

Transient absorption (TA). For the femtosecond transient absorption spectroscopy experiments, 1040 nm fundamental laser pulses were generated using a 200 kHz Spirit 1040-8 laser (Spectra-Physics). Pump pulses centered at 425 nm were generated using a portion of the 1040 nm fundamental directed into a noncollinear optical parametric amplifier (Spectra-Physics Spirit-NOPA). The pump beam was modulated at 5 kHz using a mechanical chopper (Thorlabs), and the pump-probe time delay was controlled using a mechanical delay stage (Newport). Broadband probe pulses were generated by focusing a separate portion of the 1040 nm fundamental into a 4 mm YAG crystal with a 50 mm focal length lens. Pump and probe pulses were spatially overlapped at the sample point using a 200 mm focal length concave mirror. Transmitted probe light was

collected and analyzed using a high speed data acquisition system (Ultrafast Systems). All measurements were taken at room temperature using a vigorously stirred solution phase sample in toluene in a 2mm path length cuvette.

4.10.4. Kinetic Model Analysis

Experimental determination of kinetic model parameters. Radiative and nonradiative recombination rate constants (k_r & k_{nr}) at the nanoplatelet band edge were assumed to be independent of dopant fractions and were obtained by combining PL decay lifetime data of undoped nanoplatelets (Table 4.2) with PLQY data using the following equations.

$$PLQY = \frac{k_r}{k_r + k_{nr}} = \frac{k_r}{k_{prompt}} = \frac{\tau_{prompt}}{\tau_r}$$

$$\tau_r = \frac{\tau_{prompt}}{PLQY} \qquad\qquad \tau_{nr} = \frac{\tau_{prompt}}{1 - PLQY}$$

(k_r & k_{nr}: Radiative and nonradiative rate constants, k_{prompt}: prompt decay rate constant, τ_r & τ_{nr}: Radiative and nonradiative decay lifetimes, τ_{prompt}: prompt decay lifetime)

Energy gap (Δ) was calculated based on the peak positions of the band edge emission and dopant emission. Absorption cross section (σ) at 365 nm was calculated using the absorbance measurements and particle concentrations measured by ICP-OES.

$$\sigma = \frac{Absorbance}{N_A C L} ln\ (10)$$

(N_A: Avogadro's number, C: Unit cell (or particle) concentration, L: beam path length)

Obtained absorption cross section values are summarized in Table 4.6 and showed good agreement with a recent report on absorption cross sections of undoped perovskite nanoplatelets.[60] Dopant fraction $N_{Mn,0}$ (= x) was obtained by ICP-OES. Steady-state incident photon flux was estimated using the measured excitation beam power and beam size at the sample (see relevant discussions in Chapter 4.6). Lastly, due to the large polydispersity of nanoplatelet lateral dimensions, exciton densities were calculated in 'per unit cell' basis instead of the widely used 'per particle' basis.

Chapter 5. Summary and Outlook

The scope of this thesis has been to introduce colloidal lead halide perovskite nanoplatelets, demonstrate a room-temperature synthetic protocol, enhance their stability, and expand their material functionality by doping with photoactive manganese (Mn^{2+}) ions. Including my research, significant progresses have been made in the past few years and the field of colloidal perovskite nanoplatelets is advancing quickly. And I truly believe that perovskite nanoplatelets can be a versatile material platform for the next-generation technologies.

However, I also have to admit that there still is a large room for further improvement. Hence, I'd like to conclude my thesis by pointing out future research directions in relation to my work presented. 1) Photoluminescence quantum yields of perovskite nanoplatelets presented in this thesis are still low and need to be further increased. Minimizing the amounts of excitons recombining nonradiatively can make devices more efficient. 2) Laterally-large nanoplatelets tend to aggregate in solution and this deterioration of colloidal stability makes it difficult to deposit a highly uniform thin film from the colloidal solution. Thus, minimizing the aggregation of nanoplatelets in concentrated colloidal solution and ultimately developing a protocol for the uniform film deposition will be crucial in future device fabrication processes. 3) Perovskite nanoplatelets are still not stable enough to be incorporated into a commercial device with a long lifetime and further enhancement of the stability is needed. 4) More studies on exploring and utilizing optoelectronic and spintronic properties of Mn-doped perovskite nanoplatelets will be needed to accurately assess the potential of Mn-doped perovskite nanoplatelets. 5) In addition to manganese, there are other interesting atomic dopants that have been reported to alter semiconductor nanocrystal properties. Additional studies on how those dopants affect perovskite nanoplatelet characteristics will be interesting.

To conclude, I hope that this thesis will convince other scientists and engineers that colloidal perovskite nanoplatelets can be a leading material platform for next-generation optoelectronics, spintronics, and quantum informatics, and ultimately inspire them to drive further research moving forward.

Bibliography

1. Bukowski, T. J.; Simmons, J. H., Quantum dot research: current state and future prospects. *Crit. Rev. Solid State* **2002,** *27* (3-4), 119-142.
2. Stolle, C. J.; Harvey, T. B.; Korgel, B. A., Nanocrystal photovoltaics: a review of recent progress. *Curr. Opin. Chem. Eng.* **2013,** *2* (2), 160-167.
3. Hetsch, F.; Xu, X.; Wang, H.; Kershaw, S. V.; Rogach, A. L., Semiconductor nanocrystal quantum dots as solar cell components and photosensitizers: material, charge transfer, and separation aspects of some device topologies. *J. Phys. Chem. Lett.* **2011,** *2* (15), 1879-1887.
4. Kramer, I. J.; Sargent, E. H., Colloidal quantum dot photovoltaics: a path forward. *ACS Nano* **2011,** *5* (11), 8506-8514.
5. Kovalenko, M. V., Opportunities and challenges for quantum dot photovoltaics. *Nat. Nanotechnol.* **2015,** *10* (12), 994-997.
6. Snaith, H. J., Present status and future prospects of perovskite photovoltaics. *Nat. Mater.* **2018,** *17* (5), 372-376.
7. Kirmani, A.; Luther, J.; Amassian, A.; Abolhasani, M., Colloidal Quantum Dot Photovoltaics: Current Progress and Path to GW-Scale Enabled by Smart Manufacturing. *ACS Energy Lett.* **2020,** (NREL/JA-5900-77202).
8. Wu, J.; Chen, S.; Seeds, A.; Liu, H., Quantum dot optoelectronic devices: lasers, photodetectors and solar cells. *J. Phys. D Appl. Phys.* **2015,** *48* (36), 363001.
9. Rogach, A. L.; Gaponik, N.; Lupton, J. M.; Bertoni, C.; Gallardo, D. E.; Dunn, S.; Li Pira, N.; Paderi, M.; Repetto, P.; Romanov, S. G.; O'Dwyer, C.; Torres, C. M. S.; Eychmuller, A., Light-emitting diodes with semiconductor nanocrystals. *Angew. Chem. Int. Ed.* **2008,** *47* (35), 6538-6549.
10. Dai, Q.; Duty, C. E.; Hu, M. Z., Semiconductor-Nanocrystals-Based White Light-Emitting Diodes. *Small* **2010,** *6* (15), 1577-1588.
11. Wood, V.; Bulović, V., Colloidal quantum dot light-emitting devices. *Nano Rev.* **2010,** *1* (1), 5202.
12. Shirasaki, Y.; Supran, G. J.; Bawendi, M. G.; Bulović, V., Emergence of colloidal quantum-dot light-emitting technologies. *Nat. Photonics* **2012,** *7* (1), 13-23.
13. Zhang, X.; Liu, H.; Wang, W.; Zhang, J.; Xu, B.; Karen, K. L.; Zheng, Y.; Liu, S.; Chen, S.; Wang, K.; Sun, X. W., Hybrid perovskite light-emitting diodes based on perovskite nanocrystals with organic–inorganic mixed cations. *Adv. Mater.* **2017,** *29* (18), 1606405.
14. Sutherland, B. R.; Sargent, E. H., Perovskite photonic sources. *Nat. Photonics* **2016,** *10* (5), 295-302.
15. Bourzac, K., Quantum dots go on display. *Nat. News* **2013,** *493* (7432), 283.
16. Saran, R.; Curry, R. J., Lead sulphide nanocrystal photodetector technologies. *Nat. Photonics* **2016,** *10* (2), 81-92.
17. Konstantatos, G.; Sargent, E. H., Colloidal quantum dot photodetectors. *Infrared Phys. Technol.* **2011,** *54* (3), 278-282.
18. Ahmadi, M.; Wu, T.; Hu, B., A review on organic–inorganic halide perovskite photodetectors: device engineering and fundamental physics. *Adv. Mater.* **2017,** *29* (41), 1605242.
19. Norman, J. C.; Jung, D.; Zhang, Z.; Wan, Y.; Liu, S.; Shang, C.; Herrick, R. W.; Chow, W. W.; Gossard, A. C.; Bowers, J. E., A review of high-performance quantum dot lasers on silicon. *IEEE J. Quantum Electron.* **2019,** *55* (2), 1-11.

20. Choi, M. K.; Yang, J.; Hyeon, T.; Kim, D.-H., Flexible quantum dot light-emitting diodes for next-generation displays. *npj Flex. Electron.* **2018,** *2* (1), 1-14.
21. Hu, L.; Zhao, Q.; Huang, S.; Zheng, J.; Guan, X.; Patterson, R.; Kim, J.; Shi, L.; Lin, C.-H.; Lei, Q.; Chu, D.; Tao, W.; Cheong, S.; Tilley, R. D.; Ho-Baillie, A. W. Y.; Luther, J. M.; Yuan, J.; Wu, T., Flexible and efficient perovskite quantum dot solar cells via hybrid interfacial architecture. *Nat. Commun.* **2021,** *12* (1), 1-9.
22. Choi, M. K.; Yang, J.; Kang, K.; Kim, D. C.; Choi, C.; Park, C.; Kim, S. J.; Chae, S. I.; Kim, T.-H.; Kim, J. H.; Hyeon, T.; Kim, D.-H., Wearable red–green–blue quantum dot light-emitting diode array using high-resolution intaglio transfer printing. *Nature communications* **2015,** *6* (1), 1-8.
23. Harman, T.; Taylor, P.; Walsh, M.; LaForge, B., Quantum dot superlattice thermoelectric materials and devices. *Science* **2002,** *297* (5590), 2229-2232.
24. Liu, J.; Sun, Q.-f.; Xie, X., Enhancement of the thermoelectric figure of merit in a quantum dot due to the Coulomb blockade effect. *Phys. Rev. B* **2010,** *81* (24), 245323.
25. Sothmann, B.; Sánchez, R.; Jordan, A. N., Thermoelectric energy harvesting with quantum dots. *Nanotechnology* **2014,** *26* (3), 032001.
26. Chang, J.; Waclawik, E. R., Colloidal semiconductor nanocrystals: controlled synthesis and surface chemistry in organic media. *RSC Adv.* **2014,** *4* (45), 23505-23527.
27. Green, M., The nature of quantum dot capping ligands. *J. Meter. Chem.* **2010,** *20* (28), 5797-5809.
28. Wang, R.; Shang, Y.; Kanjanaboos, P.; Zhou, W.; Ning, Z.; Sargent, E. H., Colloidal quantum dot ligand engineering for high performance solar cells. *Energy & Environ. Sci.* **2016,** *9* (4), 1130-1143.
29. Reiss, P.; Protiere, M.; Li, L., Core/shell semiconductor nanocrystals. *Small* **2009,** *5* (2), 154-168.
30. Tamirat, A. G.; Rick, J.; Dubale, A. A.; Su, W.-N.; Hwang, B.-J., Using hematite for photoelectrochemical water splitting: a review of current progress and challenges. *Nanoscale Horiz.* **2016,** *1* (4), 243-267.
31. Klimov, V. I., *Semiconductor and metal nanocrystals: synthesis and electronic and optical properties*. CRC Press: 2003.
32. Alivisatos, A. P., Perspectives on the physical chemistry of semiconductor nanocrystals. *J. Phys. Chem.* **1996,** *100* (31), 13226-13239.
33. Hines, D. A.; Kamat, P. V., Recent advances in quantum dot surface chemistry. *ACS Appl. Mater. Interfaces* **2014,** *6* (5), 3041-3057.
34. Lim, S. J.; Ma, L.; Schleife, A.; Smith, A. M., Quantum dot surface engineering: toward inert fluorophores with compact size and bright, stable emission. *Coord. Chem. Rev.* **2016,** *320*, 216-237.
35. Ha, S. K.; Mauck, C. M.; Tisdale, W. A., Toward Stable Deep-Blue Luminescent Colloidal Lead Halide Perovskite Nanoplatelets: Systematic Photostability Investigation. *Chem. Mater.* **2019,** *31* (7), 2486-2496.
36. Shamsi, J.; Kubicki, D.; Anaya, M.; Liu, Y.; Ji, K.; Frohna, K.; Grey, C. P.; Friend, R. H.; Stranks, S. D., Stable Hexylphosphonate-Capped Blue-Emitting Quantum-Confined CsPbBr3 Nanoplatelets. *ACS Energy Lett.* **2020,** *5* (6), 1900-1907. Link: https://pubs.acs.org/doi/abs/10.1021/acsenergylett.0c00935
37. Moon, H.; Lee, C.; Lee, W.; Kim, J.; Chae, H., Stability of quantum dots, quantum dot films, and quantum dot light-emitting diodes for display applications. *Adv. Mater.* **2019,** *31* (34),

1804294.
38. Liu, Y.; Gibbs, M.; Puthussery, J.; Gaik, S.; Ihly, R.; Hillhouse, H. W.; Law, M., Dependence of carrier mobility on nanocrystal size and ligand length in PbSe nanocrystal solids. *Nano Lett.* **2010,** *10* (5), 1960-1969.
39. Ginsberg, N. S.; Tisdale, W. A., Spatially resolved photogenerated exciton and charge transport in emerging semiconductors. *Annuu. Rev. Phys. Chem.* **2020,** *71*, 1-30.
40. Akselrod, G. M.; Prins, F.; Poulikakos, L. V.; Lee, E. M.; Weidman, M. C.; Mork, A. J.; Willard, A. P.; Bulović, V.; Tisdale, W. A., Subdiffusive exciton transport in quantum dot solids. *Nano Lett.* **2014,** *14* (6), 3556-3562.
41. Weidman, M. C.; Beck, M. E.; Hoffman, R. S.; Prins, F.; Tisdale, W. A., Monodisperse, air-stable PbS nanocrystals via precursor stoichiometry control. *ACS Nano* **2014,** *8* (6), 6363-6371. Link: https://pubs.acs.org/doi/abs/10.1021/nn5018654
42. Guzelturk, B.; Martinez, P. L. H.; Zhang, Q.; Xiong, Q.; Sun, H.; Sun, X. W.; Govorov, A. O.; Demir, H. V., Excitonics of semiconductor quantum dots and wires for lighting and displays. *Laser Photonics Rev.* **2014,** *8* (1), 73-93.
43. Mushonga, P.; Onani, M. O.; Madiehe, A. M.; Meyer, M., Indium phosphide-based semiconductor nanocrystals and their applications. *J. Nanomater.* **2012,** *2012*.
44. Lim, X., The nanolight revolution is coming. *Nat. News* **2016,** *531* (7592), 26.
45. Gao, Y.; Weidman, M. C.; Tisdale, W. A., CdSe Nanoplatelet Films with Controlled Orientation of their Transition Dipole Moment. *Nano Lett.* **2017,** *17* (6), 3837-3843.
46. Weidman, M. C.; Seitz, M.; Stranks, S. D.; Tisdale, W. A., Highly Tunable Colloidal Perovskite Nanoplatelets Through Variable Cation, Metal, and Halide Composition. *ACS Nano* **2016,** *10* (8), 7830-7839. Link: https://pubs.acs.org/doi/abs/10.1021/acsnano.6b03496
47. Ithurria, S.; Tessier, M.; Mahler, B.; Lobo, R.; Dubertret, B.; Efros, A. L., Colloidal nanoplatelets with two-dimensional electronic structure. *Nat. Mater.* **2011,** *10* (12), 936-941.
48. Ji, B.; Rabani, E.; Efros, A. L.; Vaxenburg, R.; Ashkenazi, O.; Azulay, D.; Banin, U.; Millo, O., Dielectric Confinement and Excitonic Effects in Two-Dimensional Nanoplatelets. *ACS Nano* **2020,** *14* (7), 8257-8265.
49. Jana, S.; Phan, T. N.; Bouet, C.; Tessier, M. D.; Davidson, P.; Dubertret, B.; Abécassis, B., Stacking and colloidal stability of CdSe nanoplatelets. *Langmuir* **2015,** *31* (38), 10532-10539.
50. Mahler, B.; Guillemot, L.; Bossard-Giannesini, L.; Ithurria, S.; Pierucci, D.; Ouerghi, A.; Patriarche, G.; Benbalagh, R.; Lacaze, E.; Rochet, F.; Lhuillier, E., Metallic functionalization of CdSe 2D nanoplatelets and its impact on electronic transport. *J. Phys. Chem. C* **2016,** *120* (23), 12351-12361.
51. Kambhampati, P., Nanoparticles, Nanocrystals, and Quantum Dots: What are the Implications of Size in Colloidal Nanoscale Materials? *J. Phys. Chem. Lett.* **2021,** *12*, 4769-4779.
52. Ithurria, S.; Dubertret, B., Quasi 2D colloidal CdSe platelets with thicknesses controlled at the atomic level. *J. Am. Chem. Soc.* **2008,** *130* (49), 16504-16505.
53. Ramvall, P.; Tanaka, S.; Nomura, S.; Riblet, P.; Aoyagi, Y., Observation of confinement-dependent exciton binding energy of GaN quantum dots. *Appl. Phys. Lett.* **1998,** *73* (8), 1104-1106.
54. Elward, J. M.; Chakraborty, A., Effect of dot size on exciton binding energy and electron–hole recombination probability in CdSe quantum dots. *J. Chem. Theory Comput.* **2013,** *9* (10), 4351-4359.
55. Zhitomirsky, D.; Kramer, I. J.; Labelle, A. J.; Fischer, A.; Debnath, R.; Pan, J.; Bakr, O. M.; Sargent, E. H., Colloidal quantum dot photovoltaics: the effect of polydispersity. *Nano Lett.* **2012,** *12* (2), 1007-1012.

56. Liu, Y.; Kim, D.; Morris, O. P.; Zhitomirsky, D.; Grossman, J. C., Origins of the stokes shift in PbS quantum dots: impact of polydispersity, ligands, and defects. *ACS Nano* **2018,** *12* (3), 2838-2845.
57. Gilmore, R. H.; Lee, E. M.; Weidman, M. C.; Willard, A. P.; Tisdale, W. A., Charge carrier hopping dynamics in homogeneously broadened PbS quantum dot solids. *Nano Lett.* **2017,** *17* (2), 893-901.
58. Sigman, M. B.; Ghezelbash, A.; Hanrath, T.; Saunders, A. E.; Lee, F.; Korgel, B. A., Solventless synthesis of monodisperse Cu2S nanorods, nanodisks, and nanoplatelets. *J. Am. Chem. Soc.* **2003,** *125* (51), 16050-16057.
59. Christodoulou, S.; Climente, J. I.; Planelles, J.; Brescia, R.; Prato, M.; Martín-García, B.; Khan, A. H.; Moreels, I., Chloride-induced thickness control in CdSe nanoplatelets. *Nano Lett.* **2018,** *18* (10), 6248-6254.
60. Gramlich, M.; Bohn, B. J.; Tong, Y.; Polavarapu, L.; Feldmann, J.; Urban, A. S., Thickness-Dependence of Exciton-Exciton Annihilation in Halide Perovskite Nanoplatelets. *J. Phys. Chem. Lett.* **2020,** *11* (13), 5361-5366.
61. Yu, J. H.; Liu, X.; Kweon, K. E.; Joo, J.; Park, J.; Ko, K.-T.; Lee, D. W.; Shen, S.; Tivakornsasithorn, K.; Son, J. S., Giant Zeeman splitting in nucleation-controlled doped CdSe: Mn 2+ quantum nanoribbons. *Nat. Mater.* **2010,** *9* (1), 47-53.
62. Rice, W. D.; Liu, W.; Baker, T. A.; Sinitsyn, N. A.; Klimov, V. I.; Crooker, S. A., Revealing giant internal magnetic fields due to spin fluctuations in magnetically doped colloidal nanocrystals. *Nat. Nanotechnol.* **2016,** *11* (2), 137-142.
63. Jurow, M. J.; Morgenstern, T.; Eisler, C.; Kang, J.; Penzo, E.; Do, M. Q.; Engelmayer, M.; Osowiecki, W. T.; Bekenstein, Y.; Tassone, C. J.; Wang, L.-W.; Alivisatos, A. P.; Brutting, W.; Liu, Y., Manipulating the Transition Dipole Moment of CsPbBr3 Perovskite Nanocrystals for Superior Optical Properties. *Nano Lett.* **2019,** *19* (4), 2489-2496.
64. Scott, R.; Heckmann, J.; Prudnikau, A. V.; Antanovich, A.; Mikhailov, A.; Owschimikow, N.; Artemyev, M.; Climente, J. I.; Woggon, U.; Grosse, N. B.; Achtstein, A. W., Directed emission of CdSe nanoplatelets originating from strongly anisotropic 2D electronic structure. *Nat. Nanotechnol.* **2017,** *12* (12), 1155-1160.
65. Schuller, J. A.; Karaveli, S.; Schiros, T.; He, K.; Yang, S.; Kymissis, I.; Shan, J.; Zia, R., Orientation of luminescent excitons in layered nanomaterials. *Nat. Nanotechnol.* **2013,** *8* (4), 271.
66. Protesescu, L.; Yakunin, S.; Bodnarchuk, M. I.; Krieg, F.; Caputo, R.; Hendon, C. H.; Yang, R. X.; Walsh, A.; Kovalenko, M. V., Nanocrystals of Cesium Lead Halide Perovskites (CsPbX(3), X = Cl, Br, and I): Novel Optoelectronic Materials Showing Bright Emission with Wide Color Gamut. *Nano Lett.* **2015,** *15* (6), 3692-3696. Link: https://pubs.acs.org/doi/10.1021/nl5048779
67. Kim, H. S.; Lee, C. R.; Im, J. H.; Lee, K. B.; Moehl, T.; Marchioro, A.; Moon, S. J.; Humphry-Baker, R.; Yum, J. H.; Moser, J. E.; Gratzel, M.; Park, N. G., Lead iodide perovskite sensitized all-solid-state submicron thin film mesoscopic solar cell with efficiency exceeding 9%. *Sci. Rep.* **2012,** *2*, 591.
68. Zhou, H.; Chen, Q.; Li, G.; Luo, S.; Song, T.-b.; Duan, H.-S.; Hong, Z.; You, J.; Liu, Y.; Yang, Y., Interface engineering of highly efficient perovskite solar cells. *Science* **2014,** *345* (6196), 542-546.
69. Yang, W. S.; Park, B.-W.; Jung, E. H.; Jeon, N. J.; Kim, Y. C.; Lee, D. U.; Shin, S. S.; Seo, J.; Kim, E. K.; Noh, J. H.; Seok, S. I., Iodide management in formamidinium-lead-halide–

based perovskite layers for efficient solar cells. *Science* **2017,** *356* (6345), 1376-1379.
70. Saliba, M.; Matsui, T.; Seo, J. Y.; Domanski, K.; Correa-Baena, J. P.; Nazeeruddin, M. K.; Zakeeruddin, S. M.; Tress, W.; Abate, A.; Hagfeldt, A.; Gratzel, M., Cesium-containing triple cation perovskite solar cells: improved stability, reproducibility and high efficiency. *Energy Environ. Sci.* **2016,** *9* (6), 1989-1997.
71. Jeon, N. J.; Noh, J. H.; Yang, W. S.; Kim, Y. C.; Ryu, S.; Seo, J.; Seok, S. I., Compositional engineering of perovskite materials for high-performance solar cells. *Nature* **2015,** *517* (7535), 476-480.
72. Stranks, S. D.; Snaith, H. J., Metal-halide perovskites for photovoltaic and light-emitting devices. *Nat. Nanotechnol.* **2015,** *10* (5), 391-402.
73. Ansari, M. I. H.; Qurashi, A.; Nazeeruddin, M. K., Frontiers, opportunities, and challenges in perovskite solar cells: A critical review. *J. Photochem. Photobiol. C* **2018,** *35*, 1-24.
74. Chen, Y.; Zhang, L.; Zhang, Y.; Gao, H.; Yan, H., Large-area perovskite solar cells–a review of recent progress and issues. *RSC Adv.* **2018,** *8* (19), 10489-10508.
75. Liu, C.; Zeng, Q.; Wei, H.; Yu, Y.; Zhao, Y.; Feng, T.; Yang, B., Metal Halide Perovskite Nanocrystal Solar Cells: Progress and Challenges. *Small Methods* **2020,** *4* (10), 2000419.
76. Ma, L.; Hao, F.; Stoumpos, C. C.; Phelan, B. T.; Wasielewski, M. R.; Kanatzidis, M. G., Carrier diffusion lengths of over 500 nm in lead-free perovskite CH3NH3SnI3 films. *J. Am. Chem. Soc.* **2016,** *138* (44), 14750-14755.
77. Dong, Q.; Fang, Y.; Shao, Y.; Mulligan, P.; Qiu, J.; Cao, L.; Huang, J., Electron-hole diffusion lengths> 175 μm in solution grown CH3NH3PbI3 single crystals. *Science* **2015,** *347* (6225), 967-970.
78. Stranks, S. D.; Eperon, G. E.; Grancini, G.; Menelaou, C.; Alcocer, M. J. P.; Leijtens, T.; Herz, L. M.; Petrozza, A.; Snaith, H. J., Electron-Hole Diffusion Lengths Exceeding 1 Micrometer in an Organometal Trihalide Perovskite Absorber. *Science* **2013,** *342* (6156), 341-344.
79. Shi, D.; Adinolfi, V.; Comin, R.; Yuan, M.; Alarousu, E.; Buin, A.; Chen, Y.; Hoogland, S.; Rothenberger, A.; Katsiev, K.; Losovyj, Y.; Zhang, X.; Dowben, P. A.; Mohammed, O. F.; Sargent, E. H.; Bakr, O. M., Low trap-state density and long carrier diffusion in organolead trihalide perovskite single crystals. *Science* **2015,** *347* (6221), 519-522.
80. McMeekin, D. P.; Sadoughi, G.; Rehman, W.; Eperon, G. E.; Saliba, M.; Horantner, M. T.; Haghighirad, A.; Sakai, N.; Korte, L.; Rech, B.; Johnston, M. B.; Herz, L. M.; Snaith, H. J., A mixed-cation lead mixed-halide perovskite absorber for tandem solar cells. *Science* **2016,** *351* (6269), 151-155.
81. Kovalenko, M. V.; Protesescu, L.; Bodnarchuk, M. I., Properties and potential optoelectronic applications of lead halide perovskite nanocrystals. *Science* **2017,** *358* (6364), 745-750.
82. Akkerman, Q. A.; Rainò, G.; Kovalenko, M. V.; Manna, L., Genesis, challenges and opportunities for colloidal lead halide perovskite nanocrystals. *Nat. Mater.* **2018,** *17*, 394–405.
83. Lai, M.; Obliger, A.; Lu, D.; Kley, C. S.; Bischak, C. G.; Kong, Q.; Lei, T.; Dou, L.; Ginsberg, N. S.; Limmer, D. T., Intrinsic anion diffusivity in lead halide perovskites is facilitated by a soft lattice. *Proc. Natl. Acad. Sci.* **2018,** *115* (47), 11929-11934.
84. Miyata, K.; Meggiolaro, D.; Trinh, M. T.; Joshi, P. P.; Mosconi, E.; Jones, S. C.; De Angelis, F.; Zhu, X.-Y., Large polarons in lead halide perovskites. *Sci. Adv.* **2017,** *3* (8), e1701217.
85. Chu, W.; Saidi, W. A.; Zhao, J.; Prezhdo, O. V., Soft Lattice and Defect Covalency Rationalize Tolerance of β-CsPbI3 Perovskite Solar Cells to Native Defects. *Angew. Chem. Int. Ed.* **2020,** *59* (16), 6435-6441.

86. Saidaminov, M. I.; Mohammed, O. F.; Bakr, O. M., Low-Dimensional-Networked Metal Halide Perovskites: The Next Big Thing. *ACS Energy Lett.* **2017,** *2* (4), 889-896.
87. Pradhan, N., Journey of making cesium lead halide perovskite nanocrystals: what's next. *J. Phys. Chem. Lett.* **2019,** *10* (19), 5847-5855.
88. Zheng, K.; Zhu, Q.; Abdellah, M.; Messing, M. E.; Zhang, W.; Generalov, A.; Niu, Y.; Ribaud, L.; Canton, S. E.; Pullerits, T., Exciton binding energy and the nature of emissive states in organometal halide perovskites. *J. Phys. Chem. Lett.* **2015,** *6* (15), 2969-2975.
89. Akkerman, Q. A.; D'Innocenzo, V.; Accornero, S.; Scarpellini, A.; Petrozza, A.; Prato, M.; Manna, L., Tuning the Optical Properties of Cesium Lead Halide Perovskite Nanocrystals by Anion Exchange Reactions. *J Am Chem Soc* **2015,** *137* (32), 10276-81.
90. Pan, J.; Shang, Y.; Yin, J.; De Bastiani, M.; Peng, W.; Dursun, I.; Sinatra, L.; El-Zohry, A. M.; Hedhili, M. N.; Emwas, A. H.; Mohammed, O. F.; Ning, Z.; Bakr, O. M., Bidentate Ligand-Passivated CsPbI3 Perovskite Nanocrystals for Stable Near-Unity Photoluminescence Quantum Yield and Efficient Red Light-Emitting Diodes. *J. Am. Chem. Soc.* **2018,** *140* (2), 562-565.
91. Kumar, S.; Jagielski, J.; Kallikounis, N.; Kim, Y. H.; Wolf, C.; Jenny, F.; Tian, T.; Hofer, C. J.; Chiu, Y. C.; Stark, W. J.; Lee, T. W.; Shih, C. J., Ultrapure Green Light-Emitting Diodes Using Two-Dimensional Formamidinium Perovskites: Achieving Recommendation 2020 Color Coordinates. *Nano Lett.* **2017,** *17* (9), 5277-5284.
92. Yuan, J.; Hazarika, A.; Zhao, Q.; Ling, X.; Moot, T.; Ma, W.; Luther, J. M., Metal halide perovskites in quantum dot solar cells: progress and prospects. *Joule* **2020,** *4* (6), 1160-1185.
93. Liang, J.; Liu, J.; Jin, Z., All-Inorganic Halide Perovskites for Optoelectronics: Progress and Prospects. *Sol. RRL* **2017,** *1* (10), 1700086.
94. Van Le, Q.; Jang, H. W.; Kim, S. Y., Recent advances toward high-efficiency halide perovskite light-emitting diodes: review and perspective. *Small Methods* **2018,** *2* (10), 1700419.
95. Veldhuis, S. A.; Boix, P. P.; Yantara, N.; Li, M.; Sum, T. C.; Mathews, N.; Mhaisalkar, S. G., Perovskite materials for light-emitting diodes and lasers. *Adv. Mater.* **2016,** *28* (32), 6804-6834.
96. Kim, Y.-H.; Cho, H.; Lee, T.-W., Metal halide perovskite light emitters. *Proc. Natl. Acad. Sci. U.S.A* **2016,** *113* (42), 11694-11702.
97. Wang, H.; Kim, D. H., Perovskite-based photodetectors: materials and devices. *Chem. Soc. Rev.* **2017,** *46* (17), 5204-5236.
98. Hong, K.; Van Le, Q.; Kim, S. Y.; Jang, H. W., Low-dimensional halide perovskites: review and issues. *J. Mater. Chem. C* **2018,** *6* (9), 2189-2209.
99. Dong, Y.; Zhao, Y.; Zhang, S.; Dai, Y.; Liu, L.; Li, Y.; Chen, Q., Recent advances toward practical use of halide perovskite nanocrystals. *J. Mater. Chem. A* **2018,** *6* (44), 21729-21746.
100. Brown, A. A.; Damodaran, B.; Jiang, L.; Tey, J. N.; Pu, S. H.; Mathews, N.; Mhaisalkar, S. G., Lead halide perovskite nanocrystals: room temperature syntheses toward commercial viability. *Adv. Energy. Mater.* **2020,** *10* (34), 2001349.
101. Peng, X., Mechanisms for the shape-control and shape-evolution of colloidal semiconductor nanocrystals. *Adv. Mater.* **2003,** *15* (5), 459-463.
102. Nordell, K. J.; Boatman, E. M.; Lisensky, G. C., A safer, easier, faster synthesis for CdSe quantum dot nanocrystals. *J. Chem. Edu.* **2005,** *82* (11), 1697.
103. Micic, O. I.; Curtis, C. J.; Jones, K. M.; Sprague, J. R.; Nozik, A. J., Synthesis and characterization of InP quantum dots. *J. Phys. Chem.* **1994,** *98* (19), 4966-4969.
104. Li, Y.; Hou, X.; Dai, X.; Yao, Z.; Lv, L.; Jin, Y.; Peng, X., Stoichiometry-controlled InP-

based quantum dots: synthesis, photoluminescence, and electroluminescence. *J. Am. Chem. Soc.* **2019,** *141* (16), 6448-6452.
105. Gary, D. C.; Cossairt, B. M., Role of acid in precursor conversion during InP quantum dot synthesis. *Chem. Mater.* **2013,** *25* (12), 2463-2469.
106. de Mello Donegá, C.; Liljeroth, P.; Vanmaekelbergh, D., Physicochemical evaluation of the hot-injection method, a synthesis route for monodisperse nanocrystals. *Small* **2005,** *1* (12), 1152-1162.
107. Anikeeva, P. O.; Halpert, J. E.; Bawendi, M. G.; Bulovic, V., Quantum dot light-emitting devices with electroluminescence tunable over the entire visible spectrum. *Nano Lett.* **2009,** *9* (7), 2532-2536.
108. Zhang, W.; Wang, C.; Zhang, L.; Zhang, X.; Liu, X.; Tang, K.; Qian, Y., Room temperature synthesis of cubic nanocrystalline CdSe in aqueous Solution. *J. Solid State Chem.* **2000,** *151* (2), 241-244.
109. Pan, D.; Wang, Q.; Jiang, S.; Ji, X.; An, L., Low-temperature synthesis of oil-soluble CdSe, CdS, and CdSe/CdS core− shell nanocrystals by using various water-soluble anion precursors. *J. Phys. Chem. C* **2007,** *111* (15), 5661-5666.
110. Wang, W.; Germanenko, I.; El-Shall, M. S., Room-temperature synthesis and characterization of nanocrystalline CdS, ZnS, and Cd x Zn1-x S. *Chem. Mater.* **2002,** *14* (7), 3028-3033.
111. Zhao, N.; Qi, L., Low-temperature synthesis of star-shaped PbS nanocrystals in aqueous solutions of mixed cationic/anionic surfactants. *Adv. Mater.* **2006,** *18* (3), 359-362.
112. Phillips, T. W.; Lignos, I. G.; Maceiczyk, R. M.; deMello, A. J.; deMello, J. C., Nanocrystal synthesis in microfluidic reactors: where next? *Lab Chip* **2014,** *14* (17), 3172-3180.
113. Baek, J.; Allen, P. M.; Bawendi, M. G.; Jensen, K. F., Investigation of indium phosphide nanocrystal synthesis using a high-temperature and high-pressure continuous flow microreactor. *Angew. Chem. Int. Ed.* **2011,** *50* (3), 627-630.
114. Park, J.; An, K.; Hwang, Y.; Park, J.-G.; Noh, H.-J.; Kim, J.-Y.; Park, J.-H.; Hwang, N.-M.; Hyeon, T., Ultra-large-scale syntheses of monodisperse nanocrystals. *Nat. Mater.* **2004,** *3* (12), 891-895.
115. Li, J. J.; Wang, Y. A.; Guo, W.; Keay, J. C.; Mishima, T. D.; Johnson, M. B.; Peng, X., Large-scale synthesis of nearly monodisperse CdSe/CdS core/shell nanocrystals using air-stable reagents via successive ion layer adsorption and reaction. *J. Am. Chem. Soc.* **2003,** *125* (41), 12567-12575.
116. Srivastava, B. B.; Jana, S.; Karan, N. S.; Paria, S.; Jana, N. R.; Sarma, D.; Pradhan, N., Highly luminescent Mn-doped ZnS nanocrystals: gram-scale synthesis. *J. Phys. Chem. Lett.* **2010,** *1* (9), 1454-1458.
117. Shamsi, J.; Urban, A. S.; Imran, M.; De Trizio, L.; Manna, L., Metal Halide Perovskite Nanocrystals: Synthesis, Post-Synthesis Modifications, and Their Optical Properties. *Chem. Rev.* **2019,** *119* (5), 3296-3348.
118. Abdel-Latif, K.; Bateni, F.; Crouse, S.; Abolhasani, M., Flow Synthesis of Metal Halide Perovskite Quantum Dots: From Rapid Parameter Space Mapping to AI-Guided Modular Manufacturing. *Matter* **2020,** *3* (4), 1053-1086.
119. Epps, R. W.; Felton, K. C.; Coley, C. W.; Abolhasani, M., Automated microfluidic platform for systematic studies of colloidal perovskite nanocrystals: towards continuous nano-manufacturing. *Lap Chip* **2017,** *17* (23), 4040-4047.
120. Liang, X.; Baker, R. W.; Wu, K.; Deng, W.; Ferdani, D.; Kubiak, P. S.; Marken, F.;

Torrente-Murciano, L.; Cameron, P. J., Continuous low temperature synthesis of MAPbX 3 perovskite nanocrystals in a flow reactor. *React. Chem. Eng.* **2018,** *3* (5), 640-644.
121. Wei, S.; Yang, Y.; Kang, X.; Wang, L.; Huang, L.; Pan, D., Room-temperature and gram-scale synthesis of CsPbX 3 (X= Cl, Br, I) perovskite nanocrystals with 50–85% photoluminescence quantum yields. *Chem. Comm.* **2016,** *52* (45), 7265-7268.
122. Shamsi, J.; Rastogi, P.; Caligiuri, V.; Abdelhady, A. L.; Spirito, D.; Manna, L.; Krahne, R., Bright-Emitting Perovskite Films by Large-Scale Synthesis and Photoinduced Solid-State Transformation of CsPbBr3 Nanoplatelets. *ACS Nano* **2017,** *11* (10), 10206-10213.
123. Wang, K. H.; Wu, L.; Li, L.; Yao, H. B.; Qian, H. S.; Yu, S. H., Large-scale synthesis of highly luminescent perovskite-related CsPb2Br5 nanoplatelets and their fast anion exchange. *Angew. Chem. Int. Ed.* **2016,** *128* (29), 8468-8472.
124. Soe, C. M. M.; Nagabhushana, G.; Shivaramaiah, R.; Tsai, H.; Nie, W.; Blancon, J.-C.; Melkonyan, F.; Cao, D. H.; Traoré, B.; Pedesseau, L.; Kepenekian, M.; Katan, C.; Even, J.; Marks, T. J.; Navrotsky, A.; Mohite, A. D.; Stoumpos, C. C.; Kanatzidis, M. G., Structural and thermodynamic limits of layer thickness in 2D halide perovskites. *Proc. Natl. Acad. Sci. U.S.A* **2019,** *116* (1), 58-66.
125. Nagabhushana, G. P.; Shivaramaiah, R.; Navrotsky, A., Direct calorimetric verification of thermodynamic instability of lead halide hybrid perovskites. *Proc. Natl. Acad. Sci. U.S.A.* **2016,** *113* (28), 7717-21.
126. Ciccioli, A.; Latini, A., Thermodynamics and the Intrinsic Stability of Lead Halide Perovskites CH3NH3PbX3. *J. Phys. Chem. Lett.* **2018,** *9* (13), 3756-3765.
127. Ivanov, I.; Steparuk, A.; Bolyachkina, M.; Tsvetkov, D.; Safronov, A.; Zuev, A. Y., Thermodynamics of formation of hybrid perovskite-type methylammonium lead halides. *J. Chem. Thermodyn.* **2018,** *116*, 253-258.
128. Zhang, Y.-Y.; Chen, S.; Xu, P.; Xiang, H.; Gong, X.-G.; Walsh, A.; Wei, S.-H., Intrinsic instability of the hybrid halide perovskite semiconductor CH3NH3PbI3. *Chin. Phys. Lett.* **2018,** *35* (3), 036104.
129. Wang, D.; Wright, M.; Elumalai, N. K.; Uddin, A., Stability of perovskite solar cells. *Sol. Energy Mater. Sol. Cells* **2016,** *147*, 255-275.
130. Park, B. w.; Seok, S. I., Intrinsic instability of inorganic–organic hybrid halide perovskite materials. *Adv. Mater.* **2019,** *31* (20), 1805337.
131. Dang, Z.; Dhanabalan, B.; Castelli, A.; Dhall, R.; Bustillo, K. C.; Marchelli, D.; Spirito, D.; Petralanda, U.; Shamsi, J.; Manna, L.; Krahne, R.; Arciniegas, M. P., Temperature-Driven Transformation of CsPbBr3 Nanoplatelets into Mosaic Nanotiles in Solution through Self-Assembly. *Nano Lett.* **2020,** *20* (3), 1808-1818.
132. Gottesman, R.; Gouda, L.; Kalanoor, B. S.; Haltzi, E.; Tirosh, S.; Rosh-Hodesh, E.; Tischler, Y.; Zaban, A.; Quarti, C.; Mosconi, E.; De Angelis, F., Photoinduced Reversible Structural Transformations in Free-Standing CH3NH3PbI3 Perovskite Films. *J. Phys. Chem. Lett.* **2015,** *6* (12), 2332-8.
133. Niu, G.; Guo, X.; Wang, L., Review of recent progress in chemical stability of perovskite solar cells. *J. Mater. Chem. A* **2015,** *3* (17), 8970-8980.
134. Wang, Y.; Li, X.; Sreejith, S.; Cao, F.; Wang, Z.; Stuparu, M. C.; Zeng, H.; Sun, H., Photon Driven Transformation of Cesium Lead Halide Perovskites from Few-Monolayer Nanoplatelets to Bulk Phase. *Adv. Mater.* **2016,** *28* (48), 10637-10643.
135. Krishnan, U.; Kaur, M.; Kumar, M.; Kumar, A., Factors affecting the stability of perovskite solar cells: a comprehensive review. *J. Photonics Energy* **2019,** *9* (2), 021001.

136. Huang, H.; Bodnarchuk, M. I.; Kershaw, S. V.; Kovalenko, M. V.; Rogach, A. L., Lead halide perovskite nanocrystals in the research spotlight: stability and defect tolerance. *ACS Energy Lett.* **2017,** *2* (9), 2071-2083.
137. Jagielski, J.; Kumar, S.; Yu, W.-Y.; Shih, C.-J., Layer-controlled two-dimensional perovskites: synthesis and optoelectronics. *J. Mater. Chem. C* **2017,** *5* (23), 5610-5627.
138. Weidman, M. C.; Goodman, A. J.; Tisdale, W. A., Colloidal halide perovskite nanoplatelets: An exciting new class of semiconductor nanomaterials. *Chem. Mater.* **2017,** *29* (12), 5019-5030.
139. Akkerman, Q. A.; Motti, S. G.; Srimath Kandada, A. R.; Mosconi, E.; D'Innocenzo, V.; Bertoni, G.; Marras, S.; Kamino, B. A.; Miranda, L.; De Angelis, F.; Petrozza, A.; Prato, M.; Manna, L., Solution Synthesis Approach to Colloidal Cesium Lead Halide Perovskite Nanoplatelets with Monolayer-Level Thickness Control. *J. Am. Chem. Soc.* **2016,** *138* (3), 1010-6. Link: https://pubs.acs.org/doi/abs/10.1021/jacs.5b12124
140. Bekenstein, Y.; Koscher, B. A.; Eaton, S. W.; Yang, P.; Alivisatos, A. P., Highly Luminescent Colloidal Nanoplates of Perovskite Cesium Lead Halide and Their Oriented Assemblies. *J. Am. Chem. Soc.* **2015,** *137* (51), 16008-16011.
141. Bertolotti, F.; Nedelcu, G.; Vivani, A.; Cervellino, A.; Masciocchi, N.; Guagliardi, A.; Kovalenko, M. V., Crystal Structure, Morphology, and Surface Termination of Cyan-Emissive, Six-Monolayers-Thick CsPbBr3 Nanoplatelets from X-ray Total Scattering. *ACS Nano* **2019,** *13* (12), 14294-14307.
142. Bohn, B. J.; Tong, Y.; Gramlich, M.; Lai, M. L.; Doblinger, M.; Wang, K.; Hoye, R. L. Z.; Muller-Buschbaum, P.; Stranks, S. D.; Urban, A. S.; Polavarapu, L.; Feldmann, J., Boosting Tunable Blue Luminescence of Halide Perovskite Nanoplatelets through Postsynthetic Surface Trap Repair. *Nano Lett.* **2018,** *18* (8), 5231-5238.
143. Huang, H.; Li, Y.; Tong, Y.; Yao, E. P.; Feil, M. W.; Richter, A. F.; Doblinger, M.; Rogach, A. L.; Feldmann, J.; Polavarapu, L., Spontaneous Crystallization of Perovskite Nanocrystals in Nonpolar Organic Solvents: A Versatile Approach for their Shape-Controlled Synthesis. *Angew. Chem.* **2019,** *58* (46), 16558-16562.
144. Mehetor, S. K.; Ghosh, H.; Pradhan, N., Acid-Amine Equilibria for Formation and Long-Range Self-Organization of Ultrathin CsPbBr3 Perovskite Platelets. *J. Phys. Chem. Lett.* **2019,** *10* (6), 1300-1305.
145. Shamsi, J.; Dang, Z.; Bianchini, P.; Canale, C.; Di Stasio, F.; Brescia, R.; Prato, M.; Manna, L., Colloidal synthesis of quantum confined single crystal CsPbBr3 nanosheets with lateral size control up to the micrometer range. *J. Am. Chem. Soc.* **2016,** *138* (23), 7240-7243. Link: https://pubs.acs.org/doi/abs/10.1021/jacs.6b03166
146. Vybornyi, O.; Yakunin, S.; Kovalenko, M. V., Polar-solvent-free colloidal synthesis of highly luminescent alkylammonium lead halide perovskite nanocrystals. *Nanoscale* **2016,** *8* (12), 6278-6283.
147. Wei, M.; de Arquer, F. P. G.; Walters, G.; Yang, Z.; Quan, L. N.; Kim, Y.; Sabatini, R.; Quintero-Bermudez, R.; Gao, L.; Fan, J. Z.; Fan, F.; Gold-Parker, A.; Toney, M. F.; Sargent, E. H., Ultrafast narrowband exciton routing within layered perovskite nanoplatelets enables low-loss luminescent solar concentrators. *Nat. Energy* **2019,** *4* (3), 197-205.
148. Wu, Y.; Wei, C.; Li, X.; Li, Y.; Qiu, S.; Shen, W.; Cai, B.; Sun, Z.; Yang, D.; Deng, Z.; Zeng, H., In Situ Passivation of PbBr64– Octahedra toward Blue Luminescent CsPbBr3 Nanoplatelets with Near 100% Absolute Quantum Yield. *ACS Energy Lett.* **2018,** *3* (9), 2030-2037.
149. Zhang, Y.; Wang, C.; Deng, Z., Colloidal synthesis of monolayer-thick formamidinium lead bromide perovskite nanosheets with a lateral size of micrometers. *ChemComm* **2018,** *54* (32),

4021-4024.
150. Kumar, S.; Jagielski, J.; Yakunin, S.; Rice, P.; Chiu, Y.-C.; Wang, M.; Nedelcu, G.; Kim, Y.; Lin, S.; Santos, E. J.; Kovalenko, M. V.; Shih, C.-J., Efficient blue electroluminescence using quantum-confined two-dimensional perovskites. *ACS Nano* **2016,** *10* (10), 9720-9729.
151. Cao, D. H.; Stoumpos, C. C.; Farha, O. K.; Hupp, J. T.; Kanatzidis, M. G., 2D Homologous Perovskites as Light-Absorbing Materials for Solar Cell Applications. *J. Am. Chem. Soc.* **2015,** *137* (24), 7843-50.
152. Quan, L. N.; Yuan, M.; Comin, R.; Voznyy, O.; Beauregard, E. M.; Hoogland, S.; Buin, A.; Kirmani, A. R.; Zhao, K.; Amassian, A.; Kim, D. H.; Sargent, E. H., Ligand-Stabilized Reduced-Dimensionality Perovskites. *J Am Chem Soc* **2016,** *138* (8), 2649-55.
153. Sichert, J. A.; Tong, Y.; Mutz, N.; Vollmer, M.; Fischer, S.; Milowska, K. Z.; Garcia Cortadella, R.; Nickel, B.; Cardenas-Daw, C.; Stolarczyk, J. K.; Urban, A. S.; Feldmann, J., Quantum Size Effect in Organometal Halide Perovskite Nanoplatelets. *Nano Lett.* **2015,** *15* (10), 6521-6527.
154. Tyagi, P.; Arveson, S. M.; Tisdale, W. A., Colloidal Organohalide Perovskite Nanoplatelets Exhibiting Quantum Confinement. *J. Phys. Chem. Lett.* **2015,** *6* (10), 1911-6.
155. Mitzi, D. B., Synthesis, structure, and properties of organic-inorganic perovskites and related materials. *Prog. Inorg. Chem.* **1999,** *48*, 1-121.
156. Mitzi, D. B.; Feild, C. A.; Harrison, W. T. A.; Guloy, A. M., Conducting tin halides with a layered organic-based perovskite structure. *Nature* **1994,** *369* (6480), 467-469.
157. Mitzi, D. B.; Wang, S.; Feild, C. A.; Chess, C. A.; Guloy, A. M., Conducting Layered Organic-Inorganic Halides Containing (110)-Oriented Perovskite Sheets. *Science* **1995,** *267* (5203), 1473-1476.
158. Ishihara, T.; Hong, X.; Ding, J.; Nurmikko, A. V., Dielectric Confinement Effect For Exciton and Biexciton States in PbI4-Based 2-Dimensional Semiconductor Structures. *Surf. Sci.* **1992,** *267*, 323-326.
159. Ishihara, T.; Takahashi, J.; Goto, T., Optical properties due to electronic transitions in two-dimensional semiconductors (CnH2n+1NH3)2PbI4. *Phys. Rev. B* **1990,** *42* (17), 11099.
160. Koutselas, I.; Ducasse, L.; Papavassiliou, G. C., Electronic properties of three-and low-dimensional semiconducting materials with Pb halide and Sn halide units. *J. Phys.: Condens. Matter* **1996,** *8* (9), 1217.
161. Ishihara, T.; Takahashi, J.; Goto, T., Exciton state in two-dimensional perovskite semiconductor (C10H21NH3) 2PbI4. *Solid State Commun.* **1989,** *69* (9), 933-936.
162. Stoumpos, C. C.; Cao, D. H.; Clark, D. J.; Young, J.; Rondinelli, J. M.; Jang, J. I.; Hupp, J. T.; Kanatzidis, M. G., Ruddlesden–Popper hybrid lead iodide perovskite 2D homologous semiconductors. *Chem. Mater.* **2016,** *28* (8), 2852-2867.
163. Riedinger, A.; Ott, F. D.; Mule, A.; Mazzotti, S.; Knusel, P. N.; Kress, S. J. P.; Prins, F.; Erwin, S. C.; Norris, D. J., An intrinsic growth instability in isotropic materials leads to quasi-two-dimensional nanoplatelets. *Nat. Mater.* **2017,** *16* (7), 743-748.
164. Paritmongkol, W.; Dahod, N. S.; Stollmann, A.; Mao, N.; Settens, C.; Zheng, S.-L.; Tisdale, W. A., Synthetic Variation and Structural Trends in Layered Two-Dimensional Alkylammonium Lead Halide Perovskites. *Chem. Mater.* **2019,** *31* (15), 5592-5607.
165. Stoumpos, C. C.; Soe, C. M. M.; Tsai, H.; Nie, W.; Blancon, J.-C.; Cao, D. H.; Liu, F.; Traoré, B.; Katan, C.; Even, J.; Mohite, A. D.; Kanatzidis, M. G., High Members of the 2D Ruddlesden-Popper Halide Perovskites: Synthesis, Optical Properties, and Solar Cells of (CH 3 (CH 2) 3 NH 3) 2 (CH 3 NH 3) 4 Pb 5 I 16. *Chem* **2017,** *2* (3), 427-440.

166. Zhao, J.; Cao, S.; Li, Z.; Ma, N., Amino Acid-Mediated Synthesis of CsPbBr3 Perovskite Nanoplatelets with Tunable Thickness and Optical Properties. *Chem. Mater.* **2018,** *30* (19), 6737-6743.
167. Ha, S. K.; Tisdale, W. A., Facile Synthesis of Colloidal Lead Halide Perovskite Nanoplatelets via Ligand-Assisted Reprecipitation. *J. Vis. Exp.* **2019,** (152), e60114.
168. Bonato, L. G.; Moral, R. F.; Nagamine, G.; Alo, A.; Germino, J. C.; da Silva, D. S.; Almeida, D. B.; Zagonel, L. F.; Galembeck, F.; Padilha, L. A.; Nogueira, A. F., Revealing the Role of Tin(IV) Halides in the Anisotropic Growth of CsPbX3 Perovskite Nanoplates. *Angew. Chem.* **2020**.
169. Yang, D.; Zou, Y.; Li, P.; Liu, Q.; Wu, L.; Hu, H.; Xu, Y.; Sun, B.; Zhang, Q.; Lee, S.-T., Large-scale synthesis of ultrathin cesium lead bromide perovskite nanoplates with precisely tunable dimensions and their application in blue light-emitting diodes. *Nano Energy* **2018,** *47*, 235-242.
170. Yuan, Z.; Shu, Y.; Xin, Y.; Ma, B., Highly luminescent nanoscale quasi-2D layered lead bromide perovskites with tunable emissions. *ChemComm* **2016,** *52* (20), 3887-90.
171. Huang, S.; Li, Z.; Wang, B.; Zhu, N.; Zhang, C.; Kong, L.; Zhang, Q.; Shan, A.; Li, L., Morphology Evolution and Degradation of CsPbBr3 Nanocrystals under Blue Light-Emitting Diode Illumination. *ACS Appl. Mater. Interfaces* **2017,** *9* (8), 7249-7258.
172. DeCrescent, R. A.; Venkatesan, N. R.; Dahlman, C. J.; Kennard, R. M.; Chabinyc, M. L.; Schuller, J. A., Optical Constants and Effective-Medium Origins of Large Optical Anisotropies in Layered Hybrid Organic/Inorganic Perovskites. *ACS Nano* **2019,** *13* (9), 10745-10753.
173. Nistal, A.; Garcia, E.; Pérez -Coll, D.; Prieto, C.; Belmonte, M.; Osendi, M. I.; Miranzo, P., Low percolation threshold in highly conducting graphene nanoplatelets/glass composite coatings. *Carbon* **2018,** *139*, 556-563.
174. Tong, Y.; Ehrat, F.; Vanderlinden, W.; Cardenas-Daw, C.; Stolarczyk, J. K.; Polavarapu, L.; Urban, A. S., Dilution-Induced Formation of Hybrid Perovskite Nanoplatelets. *ACS Nano* **2016,** *10* (12), 10936-10944.
175. Sun, S.; Yuan, D.; Xu, Y.; Wang, A.; Deng, Z., Ligand-Mediated Synthesis of Shape-Controlled Cesium Lead Halide Perovskite Nanocrystals via Reprecipitation Process at Room Temperature. *ACS Nano* **2016,** *10* (3), 3648-57.
176. Cho, J.; Choi, Y.-H.; O'Loughlin, T. E.; De Jesus, L.; Banerjee, S., Ligand-Mediated Modulation of Layer Thicknesses of Perovskite Methylammonium Lead Bromide Nanoplatelets. *Chem. Mater.* **2016,** *28* (19), 6909-6916.
177. Seth, S.; Samanta, A., A Facile Methodology for Engineering the Morphology of CsPbX3 Perovskite Nanocrystals under Ambient Condition. *Sci. Rep.* **2016,** *6*, 37693.
178. Pan, A.; He, B.; Fan, X.; Liu, Z.; Urban, J. J.; Alivisatos, A. P.; He, L.; Liu, Y., Insight into the Ligand-Mediated Synthesis of Colloidal CsPbBr3 Perovskite Nanocrystals: The Role of Organic Acid, Base, and Cesium Precursors. *ACS Nano* **2016,** *10* (8), 7943-54.
179. Almeida, G.; Goldoni, L.; Akkerman, Q.; Dang, Z.; Khan, A. H.; Marras, S.; Moreels, I.; Manna, L., Role of Acid-Base Equilibria in the Size, Shape, and Phase Control of Cesium Lead Bromide Nanocrystals. *ACS Nano* **2018,** *12* (2), 1704-1711.
180. Tong, Y.; Bladt, E.; Ayguler, M. F.; Manzi, A.; Milowska, K. Z.; Hintermayr, V. A.; Docampo, P.; Bals, S.; Urban, A. S.; Polavarapu, L.; Feldmann, J., Highly Luminescent Cesium Lead Halide Perovskite Nanocrystals with Tunable Composition and Thickness by Ultrasonication. *Angew. Chem.* **2016,** *55* (44), 13887-13892.
181. Hintermayr, V. A.; Richter, A. F.; Ehrat, F.; Döblinger, M.; Vanderlinden, W.; Sichert, J.

A.; Tong, Y.; Polavarapu, L.; Feldmann, J.; Urban, A. S., Tuning the Optical Properties of Perovskite Nanoplatelets through Composition and Thickness by Ligand-Assisted Exfoliation. *Adv. Mater.* **2016,** *28* (43), 9478-9485.
182. Dou, L. T.; Wong, A. B.; Yu, Y.; Lai, M. L.; Kornienko, N.; Eaton, S. W.; Fu, A.; Bischak, C. G.; Ma, J.; Ding, T. N.; Ginsberg, N. S.; Wang, L. W.; Alivisatos, A. P.; Yang, P. D., Atomically thin two-dimensional organic-inorganic hybrid perovskites. *Science* **2015,** *349* (6255), 1518-1521.
183. Burlakov, V. M.; Hassan, Y.; Danaie, M.; Snaith, H. J.; Goriely, A., Competitive Nucleation Mechanism for CsPbBr3 Perovskite Nanoplatelet Growth. *J. Phys. Chem. Lett.* **2020,** *11* (16), 6535-6543.
184. Dahlman, C. J.; Venkatesan, N. R.; Corona, P. T.; Kennard, R. M.; Mao, L.; Smith, N. C.; Zhang, J.; Seshadri, R.; Helgeson, M. E.; Chabinyc, M. L., Structural Evolution of Layered Hybrid Lead Iodide Perovskites in Colloidal Dispersions. *ACS Nano* **2020,** *14* (9), 11294-11308.
185. Mir, W. J.; Jagadeeswararao, M.; Das, S.; Nag, A., Colloidal Mn-Doped Cesium Lead Halide Perovskite Nanoplatelets. *ACS Energy Lett.* **2017,** *2* (3), 537-543.
186. Saidaminov, M. I.; Abdelhady, A. L.; Murali, B.; Alarousu, E.; Burlakov, V. M.; Peng, W.; Dursun, I.; Wang, L.; He, Y.; Maculan, G.; Goriely, A.; Wu, T.; Mohammed, O. F.; Bakr, O. M., High-quality bulk hybrid perovskite single crystals within minutes by inverse temperature crystallization. *Nat. Commun.* **2015,** *6*, 7586.
187. Gangishetty, M. K.; Hou, S.; Quan, Q.; Congreve, D. N., Reducing Architecture Limitations for Efficient Blue Perovskite Light-Emitting Diodes. *Adv. Mater.* **2018,** *30* (20), 1706226.
188. Congreve, D. N.; Weidman, M. C.; Seitz, M.; Paritmongkol, W.; Dahod, N. S.; Tisdale, W. A., Tunable Light-Emitting Diodes Utilizing Quantum-Confined Layered Perovskite Emitters. *ACS Photonics* **2017,** *4* (3), 476-481.
189. Kim, Y. H.; Cho, H.; Heo, J. H.; Kim, T. S.; Myoung, N.; Lee, C. L.; Im, S. H.; Lee, T. W., Multicolored organic/inorganic hybrid perovskite light-emitting diodes. *Adv Mater* **2015,** *27* (7), 1248-54.
190. Pan, J.; Quan, L. N.; Zhao, Y.; Peng, W.; Murali, B.; Sarmah, S. P.; Yuan, M.; Sinatra, L.; Alyami, N. M.; Liu, J.; Yassitepe, E.; Yang, Z.; Voznyy, O.; Comin, R.; Hedhili, M. N.; Mohammed, O. F.; Lu, Z. H.; Kim, D. H.; Sargent, E. H.; Bakr, O. M., Highly Efficient Perovskite-Quantum-Dot Light-Emitting Diodes by Surface Engineering. *Adv. Mater.* **2016,** *28* (39), 8718-8725.
191. Tsai, H.; Nie, W.; Blancon, J. C.; Stoumpos, C. C.; Soe, C. M. M.; Yoo, J.; Crochet, J.; Tretiak, S.; Even, J.; Sadhanala, A.; Azzellino, G.; Brenes, R.; Ajayan, P. M.; Bulovic, V.; Stranks, S. D.; Friend, R. H.; Kanatzidis, M. G.; Mohite, A. D., Stable Light-Emitting Diodes Using Phase-Pure Ruddlesden–Popper Layered Perovskites. *Advanced Materials* **2018,** *30* (6), 1704217.
192. Sutherland, B. R.; Hoogland, S.; Adachi, M. M.; Wong, C. T.; Sargent, E. H., Conformal organohalide perovskites enable lasing on spherical resonators. *ACS nano* **2014,** *8* (10), 10947-10952.
193. Deschler, F.; Price, M.; Pathak, S.; Klintberg, L. E.; Jarausch, D.-D.; Higler, R.; Hüttner, S.; Leijtens, T.; Stranks, S. D.; Snaith, H. J., High photoluminescence efficiency and optically pumped lasing in solution-processed mixed halide perovskite semiconductors. *The journal of physical chemistry letters* **2014,** *5* (8), 1421-1426.
194. Zhu, H.; Fu, Y.; Meng, F.; Wu, X.; Gong, Z.; Ding, Q.; Gustafsson, M. V.; Trinh, M.

T.; Jin, S.; Zhu, X., Lead halide perovskite nanowire lasers with low lasing thresholds and high quality factors. *Nature materials* **2015,** *14* (6), 636.
195. Fang, Y.; Huang, J., Resolving weak light of sub-picowatt per square centimeter by hybrid perovskite photodetectors enabled by noise reduction. *Advanced Materials* **2015,** *27* (17), 2804-2810.
196. Shen, L.; Fang, Y.; Wang, D.; Bai, Y.; Deng, Y.; Wang, M.; Lu, Y.; Huang, J., A Self-Powered, Sub-nanosecond-Response Solution-Processed Hybrid Perovskite Photodetector for Time-Resolved Photoluminescence-Lifetime Detection. *Advanced Materials* **2016,** *28* (48), 10794-10800.
197. Dou, L.; Yang, Y. M.; You, J.; Hong, Z.; Chang, W.-H.; Li, G.; Yang, Y., Solution-processed hybrid perovskite photodetectors with high detectivity. *Nature communications* **2014,** *5*, 5404.
198. Schmidt, L. C.; Pertegas, A.; Gonzalez-Carrero, S.; Malinkiewicz, O.; Agouram, S.; Minguez Espallargas, G.; Bolink, H. J.; Galian, R. E.; Perez-Prieto, J., Nontemplate synthesis of CH3NH3PbBr3 perovskite nanoparticles. *J. Am. Chem. Soc.* **2014,** *136* (3), 850-853.
199. Imran, M.; Ijaz, P.; Baranov, D.; Goldoni, L.; Petralanda, U.; Akkerman, Q.; Abdelhady, A. L.; Prato, M.; Bianchini, P.; Infante, I., Shape-Pure, Nearly Monodispersed CsPbBr3 Nanocubes Prepared Using Secondary Aliphatic Amines. *Nano letters* **2018,** *18* (12), 7822-7831.
200. Dong, Y.; Qiao, T.; Kim, D.; Parobek, D.; Rossi, D.; Son, D. H., Precise Control of Quantum Confinement in Cesium Lead Halide Perovskite Quantum Dots via Thermodynamic Equilibrium. *Nano Lett.* **2018,** *18* (6), 3716-3722.
201. Sun, S.; Yuan, D.; Xu, Y.; Wang, A.; Deng, Z., Ligand-mediated synthesis of shape-controlled cesium lead halide perovskite nanocrystals via reprecipitation process at room temperature. *ACS nano* **2016,** *10* (3), 3648-3657.
202. Zhang, D.; Eaton, S. W.; Yu, Y.; Dou, L.; Yang, P., Solution-phase synthesis of cesium lead halide perovskite nanowires. *Journal of the American Chemical Society* **2015,** *137* (29), 9230-9233.
203. Huang, H.; Polavarapu, L.; Sichert, J. A.; Susha, A. S.; Urban, A. S.; Rogach, A. L., Colloidal lead halide perovskite nanocrystals: synthesis, optical properties and applications. *NPG Asia Materials* **2016,** *8* (11), e328.
204. Kojima, A.; Teshima, K.; Shirai, Y.; Miyasaka, T., Organometal Halide Perovskites as Visible-Light Sensitizers for Photovoltaic Cells. *Journal of the American Chemical Society* **2009,** *131* (17), 6050-+.
205. Bischak, C. G.; Hetherington, C. L.; Wu, H.; Aloni, S.; Ogletree, D. F.; Limmer, D. T.; Ginsberg, N. S., Origin of reversible photoinduced phase separation in hybrid perovskites. *Nano letters* **2017,** *17* (2), 1028-1033.
206. Mauck, C. M.; Tisdale, W. A., Excitons in 2D Organic–Inorganic Halide Perovskites. *Trends in Chemistry* **2019**.
207. Gong, X.; Voznyy, O.; Jain, A.; Liu, W.; Sabatini, R.; Piontkowski, Z.; Walters, G.; Bappi, G.; Nokhrin, S.; Bushuyev, O.; Yuan, M.; Comin, R.; McCamant, D.; Kelley, S. O.; Sargent, E. H., Electron-phonon interaction in efficient perovskite blue emitters. *Nat. Mater.* **2018,** *17* (6), 550-556.
208. deMello, J. C.; Wittmann, H. F.; Friend, R. H., An improved experimental determination of external photoluminescence quantum efficiency. *Advanced Materials* **1997,** *9* (3), 230-&.
209. Yang, X.; Xu, X.; Zhou, G., Recent advances of the emitters for high performance deep-blue organic light-emitting diodes. *J. Mater. Chem. C* **2015,** *3* (5), 913-944.

210. Im, Y.; Byun, S. Y.; Kim, J. H.; Lee, D. R.; Oh, C. S.; Yook, K. S.; Lee, J. Y., Recent Progress in High-Efficiency Blue-Light-Emitting Materials for Organic Light-Emitting Diodes. *Adv. Funct. Mater.* **2017,** *27* (13), 1603007.
211. Dai, X.; Deng, Y.; Peng, X.; Jin, Y., Quantum-Dot Light-Emitting Diodes for Large-Area Displays: Towards the Dawn of Commercialization. *Adv. Mater.* **2017,** *29* (14), 1607022.
212. Shirasaki, Y.; Supran, G. J.; Tisdale, W. A.; Bulović, V., Origin of efficiency roll-off in colloidal quantum-dot light-emitting diodes. *Phys. Rev. Lett.* **2013,** *110* (21), 217403.
213. Verzellesi, G.; Saguatti, D.; Meneghini, M.; Bertazzi, F.; Goano, M.; Meneghesso, G.; Zanoni, E., Efficiency droop in InGaN/GaN blue light-emitting diodes: Physical mechanisms and remedies. *J. Appl. Phys.* **2013,** *114* (7), 10_1.
214. Wilks, R. G.; Bär, M., Perovskite solar cells: Danger from within. *Nat. Energy* **2017,** *2* (1), 16204.
215. Zhang, F.; Zhong, H.; Chen, C.; Wu, X.-g.; Hu, X.; Huang, H.; Han, J.; Zou, B.; Dong, Y., Brightly Luminescent and Color-Tunable Colloidal CH3NH3PbX3 (X = Br, I, Cl) Quantum Dots: Potential Alternatives for Display Technology. *ACS Nano* **2015,** *9* (4), 4533-4542.
216. Yao, E. P.; Yang, Z.; Meng, L.; Sun, P.; Dong, S.; Yang, Y.; Yang, Y., High-Brightness Blue and White LEDs based on Inorganic Perovskite Nanocrystals and their Composites. *Adv. Mater.* **2017,** *29* (23), 1606859.
217. Sadhanala, A.; Ahmad, S.; Zhao, B.; Giesbrecht, N.; Pearce, P. M.; Deschler, F.; Hoye, R. L.; Godel, K. C.; Bein, T.; Docampo, P.; Dutton, S. E.; De Volder, M. F.; Friend, R. H., Blue-Green Color Tunable Solution Processable Organolead Chloride-Bromide Mixed Halide Perovskites for Optoelectronic Applications. *Nano Lett.* **2015,** *15* (9), 6095-6101.
218. Kumawat, N. K.; Dey, A.; Kumar, A.; Gopinathan, S. P.; Narasimhan, K. L.; Kabra, D., Band Gap Tuning of CH(3)NH(3)Pb(Br(1-x)Clx)(3) Hybrid Perovskite for Blue Electroluminescence. *ACS Appl. Mater. Interfaces* **2015,** *7* (24), 13119-13124.
219. Pedesseau, L.; Sapori, D.; Traore, B.; Robles, R.; Fang, H. H.; Loi, M. A.; Tsai, H.; Nie, W.; Blancon, J. C.; Neukirch, A.; Tretiak, S.; Mohite, A. D.; Katan, C.; Even, J.; Kepenekian, M., Advances and Promises of Layered Halide Hybrid Perovskite Semiconductors. *ACS Nano* **2016,** *10* (11), 9776-9786.
220. Wang, Q.; Ren, J.; Peng, X.-F.; Ji, X.-X.; Yang, X.-H., Efficient Sky-Blue Perovskite Light-Emitting Devices Based on Ethylammonium Bromide Induced Layered Perovskites. *ACS Appl. Mater. Interfaces* **2017,** *9* (35), 29901-29906.
221. Jagielski, J.; Kumar, S.; Wang, M.; Scullion, D.; Lawrence, R.; Li, Y.-T.; Yakunin, S.; Tian, T.; Kovalenko, M. V.; Chiu, Y.-C.; Santos, E. J. G.; Lin, S.; Shih, C.-J., Aggregation-induced emission in lamellar solids of colloidal perovskite quantum wells. *Sci. Adv.* **2017,** *3* (12), eaaq0208.
222. Fu, R.; Zhao, Y.; Li, Q.; Zhou, W.; Yu, D.; Zhao, Q., Enhanced long-term stability of perovskite solar cells by 3-hydroxypyridine dipping. *Chem. Commun.* **2017,** *53* (11), 1829-1831.
223. Yuan, Y.; Huang, J., Ion Migration in Organometal Trihalide Perovskite and Its Impact on Photovoltaic Efficiency and Stability. *Acc. Chem. Res.* **2016,** *49* (2), 286-293.
224. Gonzalez-Carrero, S.; Galian, R. E.; Pérez-Prieto, J., Maximizing the emissive properties of CH 3 NH 3 PbBr 3 perovskite nanoparticles. *J. Mater. Chem. A* **2015,** *3* (17), 9187-9193.
225. Gottlieb, H. E.; Kotlyar, V.; Nudelman, A., NMR chemical shifts of common laboratory solvents as trace impurities. *J. Org. Chem.* **1997,** *62* (21), 7512-7515.
226. Yan, K.; Long, M.; Zhang, T.; Wei, Z.; Chen, H.; Yang, S.; Xu, J., Hybrid halide perovskite solar cell precursors: colloidal chemistry and coordination engineering behind device

processing for high efficiency. *J. Am. Chem. Soc.* **2015,** *137* (13), 4460-4468.
227. Boonmongkolras, P.; Kim, D.; Alhabshi, E. M.; Gereige, I.; Shin, B., Understanding effects of precursor solution aging in triple cation lead perovskite. *RSC Adv.* **2018,** *8* (38), 21551-21557.
228. Long, M.; Zhang, T.; Chai, Y.; Ng, C. F.; Mak, T. C.; Xu, J.; Yan, K., Nonstoichiometric acid-base reaction as reliable synthetic route to highly stable CH3NH3PbI3 perovskite film. *Nat. Commun.* **2016,** *7*, 13503.
229. McMeekin, D. P.; Wang, Z.; Rehman, W.; Pulvirenti, F.; Patel, J. B.; Noel, N. K.; Johnston, M. B.; Marder, S. R.; Herz, L. M.; Snaith, H. J., Crystallization Kinetics and Morphology Control of Formamidinium–Cesium Mixed-Cation Lead Mixed-Halide Perovskite via Tunability of the Colloidal Precursor Solution. *Adv. Mater.* **2017,** *29* (29), 1607039.
230. Goldschmidt, V. M., The laws of crystal chemistry. *Naturwissenschaften* **1926,** *14* (21), 477-485.
231. Saparov, B.; Mitzi, D. B., Organic–inorganic perovskites: structural versatility for functional materials design. *Chem. Rev.* **2016,** *116* (7), 4558-4596.
232. Saidaminov, M. I.; Kim, J.; Jain, A.; Quintero-Bermudez, R.; Tan, H.; Long, G.; Tan, F.; Johnston, A.; Zhao, Y.; Voznyy, O.; Sargent, E. H., Suppression of atomic vacancies via incorporation of isovalent small ions to increase the stability of halide perovskite solar cells in ambient air. *Nat. Energy* **2018,** *3* (8), 648-654.
233. Li, Z.; Yang, M.; Park, J.-S.; Wei, S.-H.; Berry, J. J.; Zhu, K., Stabilizing perovskite structures by tuning tolerance factor: formation of formamidinium and cesium lead iodide solid-state alloys. *Chem. Mater.* **2015,** *28* (1), 284-292.
234. Kieslich, G.; Sun, S.; Cheetham, A. K., Solid-state principles applied to organic–inorganic perovskites: new tricks for an old dog. *Chem. Sci.* **2014,** *5* (12), 4712-4715.
235. Merdasa, A.; Bag, M.; Tian, Y.; Källman, E.; Dobrovolsky, A.; Scheblykin, I. G., Super-Resolution Luminescence Microspectroscopy Reveals the Mechanism of Photoinduced Degradation in CH3NH3PbI3Perovskite Nanocrystals. *J. Phys. Chem. C* **2016,** *120* (19), 10711-10719.
236. Tan, H.; Che, F.; Wei, M.; Zhao, Y.; Saidaminov, M. I.; Todorović, P.; Broberg, D.; Walters, G.; Tan, F.; Zhuang, T.; Sun, B.; Liang, Z.; Yuan, H.; Fron, E.; Kim, J.; Yang, Z.; Voznyy, O.; Asta, M.; Sargent, E. H., Dipolar cations confer defect tolerance in wide-bandgap metal halide perovskites. *Nat. Commun.* **2018,** *9*, 3100.
237. Kirchnerová, J.; Cave, G. C. B., The solubility of water in low-dielectric solvents. *Can. J. Chem.* **1976,** *54* (24), 3909-3916.
238. Gottesman, R.; Haltzi, E.; Gouda, L.; Tirosh, S.; Bouhadana, Y.; Zaban, A.; Mosconi, E.; De Angelis, F., Extremely Slow Photoconductivity Response of CH3NH3PbI3 Perovskites Suggesting Structural Changes under Working Conditions. *J. Phys. Chem. Lett.* **2014,** *5* (15), 2662-2669.
239. Manser, J. S.; Saidaminov, M. I.; Christians, J. A.; Bakr, O. M.; Kamat, P. V., Making and Breaking of Lead Halide Perovskites. *Acc. Chem. Res.* **2016,** *49* (2), 330-338.
240. De Roo, J.; Ibanez, M.; Geiregat, P.; Nedelcu, G.; Walravens, W.; Maes, J.; Martins, J. C.; Van Driessche, I.; Kovalenko, M. V.; Hens, Z., Highly Dynamic Ligand Binding and Light Absorption Coefficient of Cesium Lead Bromide Perovskite Nanocrystals. *ACS Nano* **2016,** *10* (2), 2071-2081.
241. Azpiroz, J. M.; Mosconi, E.; Bisquert, J.; De Angelis, F., Defect migration in methylammonium lead iodide and its role in perovskite solar cell operation. *Energy Environ. Sci.*

2015, *8* (7), 2118-2127.
242. Nie, W.; Blancon, J. C.; Neukirch, A. J.; Appavoo, K.; Tsai, H.; Chhowalla, M.; Alam, M. A.; Sfeir, M. Y.; Katan, C.; Even, J.; Tretiak, S.; Crochet, J. J.; Gupta, G.; Mohite, A. D., Light-activated photocurrent degradation and self-healing in perovskite solar cells. *Nat. Commun.* **2016,** *7* (1), 11574.
243. Krieg, F.; Ochsenbein, S. T.; Yakunin, S.; Ten Brinck, S.; Aellen, P.; Süess, A.; Clerc, B.; Guggisberg, D.; Nazarenko, O.; Shynkarenko, Y.; Kumar, S.; Shih, C.-J.; Infante, I.; Kovalenko, M. V., Colloidal CsPbX3 (X= Cl, Br, I) nanocrystals 2.0: Zwitterionic capping ligands for improved durability and stability. *ACS Energy Lett.* **2018,** *3* (3), 641-646.
244. Chen, H.-Y.; Chen, T.-Y.; Berdugo, E.; Park, Y.; Lovering, K.; Son, D. H., Hot Electrons from Consecutive Exciton–Mn Energy Transfer in Mn-Doped Semiconductor Nanocrystals. *J. Phys. Chem. C* **2011,** *115* (23), 11407-11412.
245. Chen, O.; Shelby, D. E.; Yang, Y.; Zhuang, J.; Wang, T.; Niu, C.; Omenetto, N.; Cao, Y. C., Excitation-intensity-dependent color-tunable dual emissions from manganese-doped CdS/ZnS core/shell nanocrystals. *Angew. Chem. Int. Ed.* **2010,** *49* (52), 10132-10135.
246. Chen, Z.; Chen, H.; Zhang, C.; Chen, L.; Qin, Z.; Sang, H.; Wang, X.; Xiao, M., Excitation-tailored dual-color emission of manganese(II)-doped perovskite nanocrystals. *Applied Physics Letters* **2019,** *114* (4).
247. Bradshaw, L. R.; Hauser, A.; McLaurin, E. J.; Gamelin, D. R., Luminescence Saturation via Mn2+–Exciton Cross Relaxation in Colloidal Doped Semiconductor Nanocrystals. *The Journal of Physical Chemistry C* **2012,** *116* (16), 9300-9310.
248. Das Adhikari, S.; Guria, A. K.; Pradhan, N., Insights of Doping and the Photoluminescence Properties of Mn-Doped Perovskite Nanocrystals. *J. Phys. Chem. Lett.* **2019,** *10* (9), 2250-2257.
249. Gan, C.; Zhang, Y.; Battaglia, D.; Peng, X.; Xiao, M., Fluorescence lifetime of Mn-doped ZnSe quantum dots with size dependence. *Appl. Phys. Lett.* **2008,** *92* (24), 241111.
250. Guria, A. K.; Dutta, S. K.; Adhikari, S. D.; Pradhan, N., Doping Mn2+ in Lead Halide Perovskite Nanocrystals: Successes and Challenges. *ACS Energy Lett.* **2017,** *2* (5), 1014-1021.
251. Mikoshiba, S.; Shirai, S.; Shinada, S.; Fukushima, M., Saturation of Zn2SiO4: Mn luminescence under intense VUV excitation. *J. Appl. Phys.* **1979,** *50* (2), 1088-1090.
252. Vlaskin, V. A.; Janssen, N.; van Rijssel, J.; Beaulac, R.; Gamelin, D. R., Tunable dual emission in doped semiconductor nanocrystals. *Nano Lett* **2010,** *10* (9), 3670-4.
253. Beaulac, R.; Archer, P. I.; van Rijssel, J.; Meijerink, A.; Gamelin, D. R., Exciton storage by Mn2+ in colloidal Mn2+-doped CdSe quantum dots. *Nano lett.* **2008,** *8* (9), 2949-2953.
254. Lin, J.; Zhang, Q.; Wang, L.; Liu, X.; Yan, W.; Wu, T.; Bu, X.; Feng, P., Atomically precise doping of monomanganese ion into coreless supertetrahedral chalcogenide nanocluster inducing unusual red shift in Mn(2+) emission. *J. Am. Chem. Soc.* **2014,** *136* (12), 4769-79.
255. Yang, Y.; Chen, O.; Angerhofer, A.; Cao, Y. C., Radial-position-controlled doping of CdS/ZnS core/shell nanocrystals: surface effects and position-dependent properties. *Chem. Eur. J.* **2009,** *15* (13), 3186-97.
256. Pradhan, N.; Sarma, D., Advances in light-emitting doped semiconductor nanocrystals. *J. Phys. Chem. Lett.* **2011,** *2* (21), 2818-2826.
257. Meinardi, F.; Akkerman, Q. A.; Bruni, F.; Park, S.; Mauri, M.; Dang, Z.; Manna, L.; Brovelli, S., Doped Halide Perovskite Nanocrystals for Reabsorption-Free Luminescent Solar Concentrators. *ACS Energy Lett.* **2017,** *2* (10), 2368-2377.
258. Peng, L.; Li, D.; Zhang, Z.; Huang, K.; Zhang, Y.; Shi, Z.; Xie, R.; Yang, W., Large-scale synthesis of single-source, thermally stable, and dual-emissive Mn-doped Zn–Cu–In–S

nanocrystals for bright white light-emitting diodes. *Nano Res.* **2015,** *8* (10), 3316-3331.
259. Santra, P. K.; Kamat, P. V., Mn-doped quantum dot sensitized solar cells: a strategy to boost efficiency over 5%. *J. Am. Chem. Soc.* **2012,** *134* (5), 2508-2511.
260. Kobak, J.; Smoleński, T.; Goryca, M.; Papaj, M.; Gietka, K.; Bogucki, A.; Koperski, M.; Rousset, J.-G.; Suffczyński, J.; Janik, E., Designing quantum dots for solotronics. *Nat. Commun.* **2014,** *5* (1), 1-8.
261. Wolf, S.; Awschalom, D.; Buhrman, R.; Daughton, J.; von Molnár, v. S.; Roukes, M.; Chtchelkanova, A. Y.; Treger, D., Spintronics: a spin-based electronics vision for the future. *Science* **2001,** *294* (5546), 1488-1495.
262. Erwin, S. C.; Zu, L.; Haftel, M. I.; Efros, A. L.; Kennedy, T. A.; Norris, D. J., Doping semiconductor nanocrystals. *Nature* **2005,** *436* (7047), 91-94.
263. Ronning, C.; Gao, P.; Ding, Y.; Wang, Z. L.; Schwen, D., Manganese-doped ZnO nanobelts for spintronics. *Appl. Phys. Lett.* **2004,** *84* (5), 783-785.
264. Kagan, C. R.; Bassett, L. C.; Murray, C. B.; Thompson, S. M., Colloidal Quantum Dots as Platforms for Quantum Information Science. *Chem. Rev.* **2020,** *121* (5), 3186-3233.
265. Huang, H.; Susha, A. S.; Kershaw, S. V.; Hung, T. F.; Rogach, A. L., Control of emission color of high quantum yield CH3NH3PbBr3 perovskite quantum dots by precipitation temperature. *Adv. Sci.* **2015,** *2* (9), 1500194.
266. Deng, S.; Shi, E.; Yuan, L.; Jin, L.; Dou, L.; Huang, L., Long-range exciton transport and slow annihilation in two-dimensional hybrid perovskites. *Nat. Commun.* **2020,** *11* (1), 664.
267. Babu, K. J.; Kaur, G.; Shukla, A.; Kaur, A.; Goswami, T.; Ghorai, N.; Ghosh, H. N., Concurrent Energy- and Electron-Transfer Dynamics in Photoexcited Mn-Doped CsPbBr3 Perovskite Nanoplatelet Architecture. *J. Phys. Chem. Lett.* **2021,** *12* (1), 302-309.
268. Das Adhikari, S.; Dutta, A.; Dutta, S. K.; Pradhan, N., Layered Perovskites L2(Pb1–xMnx)Cl4 to Mn-Doped CsPbCl3 Perovskite Platelets. *ACS Energy Lett.* **2018,** *3* (6), 1247-1253.
269. Gao, X.; Shen, X.; Xue, D.; Li, X.; Lu, P.; Lu, M.; Li, C.; Yu, W. W.; Bai, X., Dual-color emitting Mn2+ ion doped (PEA)2PbBr4 perovskite towards white light-emitting diodes. *Mater. Chem. Front* **2021,** *5* (2), 937-943.
270. Li, Z.-J.; Hofman, E.; Davis, A. H.; Khammang, A.; Wright, J. T.; Dzikovski, B.; Meulenberg, R. W.; Zheng, W., Complete Dopant Substitution by Spinodal Decomposition in Mn-Doped Two-Dimensional CsPbCl3 Nanoplatelets. *Chem. Mater.* **2018,** *30* (18), 6400-6409.
271. Zhang, H.; Yao, J.; Fu, H., Ultrathin Monolayer Mn2+-Alloyed 2D Perovskite Colloidal Quantum Wells. *Adv. Opt. Mater.* **2020,** *9* (6).
272. Liu, W.; Lin, Q.; Li, H.; Wu, K.; Robel, I.; Pietryga, J. M.; Klimov, V. I., Mn(2+)-Doped Lead Halide Perovskite Nanocrystals with Dual-Color Emission Controlled by Halide Content. *J. Am. Chem. Soc.* **2016,** *138* (45), 14954-14961.
273. Parobek, D.; Roman, B. J.; Dong, Y.; Jin, H.; Lee, E.; Sheldon, M.; Son, D. H., Exciton-to-dopant energy transfer in Mn-doped cesium lead halide perovskite nanocrystals. *Nano Lett.* **2016,** *16* (12), 7376-7380.
274. Paul, S.; Bladt, E.; Richter, A. F.; Doblinger, M.; Tong, Y.; Huang, H.; Dey, A.; Bals, S.; Debnath, T.; Polavarapu, L.; Feldmann, J., Manganese-Doping-Induced Quantum Confinement within Host Perovskite Nanocrystals through Ruddlesden-Popper Defects. *Angew. Chem. Int. Ed.* **2020,** *59* (17), 6794-6799.
275. Sarang, S.; Delmas, W.; Bonabi Naghadeh, S.; Cherrette, V.; Zhang, J. Z.; Ghosh, S., Low-Temperature Energy Transfer via Self-Trapped Excitons in Mn(2+)-Doped 2D Organometal Halide Perovskites. *J. Phys. Chem. Lett.* **2020,** *11* (24), 10368-10374.

276. Su, B.; Molokeev, M. S.; Xia, Z., Unveiling Mn(2+) Dopant States in Two-Dimensional Halide Perovskite toward Highly Efficient Photoluminescence. *J. Phys. Chem. Lett.* **2020,** *11* (7), 2510-2517.
277. Rossi, D.; Parobek, D.; Dong, Y.; Son, D. H., Dynamics of exciton–Mn energy transfer in Mn-doped CsPbCl3 perovskite nanocrystals. *J. Phys. Chem. C* **2017,** *121* (32), 17143-17149.
278. Pradhan, N., Red-Tuned Mn d–d Emission in Doped Semiconductor Nanocrystals. *ChemPhysChem* **2016,** *17* (8), 1087-1094.
279. Pathak, S.; Sakai, N.; Wisnivesky Rocca Rivarola, F.; Stranks, S. D.; Liu, J.; Eperon, G. E.; Ducati, C.; Wojciechowski, K.; Griffiths, J. T.; Haghighirad, A. A.; Pellaroque, A.; Friend, R. H.; Snaith, H. J., Perovskite Crystals for Tunable White Light Emission. *Chemistry of Materials* **2015,** *27* (23), 8066-8075.
280. Vegard, L., Die konstitution der mischkristalle und die raumfüllung der atome. *Zeitschrift für Physik* **1921,** *5* (1), 17-26.
281. Li, Z.; Yang, M.; Park, J.-S.; Wei, S.-H.; Berry, J. J.; Zhu, K., Stabilizing perovskite structures by tuning tolerance factor: formation of formamidinium and cesium lead iodide solid-state alloys. *Chem. Mater.* **2016,** *28* (1), 284-292.
282. Paul, S.; Bladt, E.; Richter, A. F.; Döblinger, M.; Tong, Y.; Huang, H.; Dey, A.; Bals, S.; Debnath, T.; Polavarapu, L., Manganese-Doping-Induced Quantum Confinement within Host Perovskite Nanocrystals through Ruddlesden–Popper Defects. *Angew. Chem. Int. Ed.* **2020,** *59* (17), 6794-6799.
283. Xiong, S.; Lee, S.-Y.; Noyan, I. C., Average and local strain fields in nanocrystals. *J. Appl. Crystallogr.* **2019,** *52* (2), 262-273.
284. Fu, Y.; Hautzinger, M. P.; Luo, Z.; Wang, F.; Pan, D.; Aristov, M. M.; Guzei, I. A.; Pan, A.; Zhu, X.; Jin, S., Incorporating Large A Cations into Lead Iodide Perovskite Cages: Relaxed Goldschmidt Tolerance Factor and Impact on Exciton-Phonon Interaction. *ACS Cent. Sci.* **2019,** *5* (8), 1377-1386.
285. Rabouw, F. T.; van der Bok, J. C.; Spinicelli, P.; Mahler, B.; Nasilowski, M.; Pedetti, S.; Dubertret, B.; Vanmaekelbergh, D., Temporary charge carrier separation dominates the photoluminescence decay dynamics of colloidal CdSe nanoplatelets. *Nano Lett.* **2016,** *16* (3), 2047-2053.
286. Blancon, J.-C.; Stier, A. V.; Tsai, H.; Nie, W.; Stoumpos, C. C.; Traore, B.; Pedesseau, L.; Kepenekian, M.; Katsutani, F.; Noe, G.; Kono, J.; Tretiak, S.; Crooker, S.; Katan, C.; Kanatzidis, M.; Crochet, J.; Even, J.; Mohite, A., Scaling law for excitons in 2D perovskite quantum wells. *Nat. Commun.* **2018,** *9* (1), 1-10.
287. Song, B.; Hou, J.; Wang, H.; Sidhik, S.; Miao, J.; Gu, H.; Zhang, H.; Liu, S.; Fakhraai, Z.; Even, J.; Blancon, J.-C.; Mohite, A. D.; Jariwala, D., Determination of Dielectric Functions and Exciton Oscillator Strength of Two-Dimensional Hybrid Perovskites. *ACS Mater. Lett.* **2020,** *3*, 148-159.
288. Manser, J. S.; Christians, J. A.; Kamat, P. V., Intriguing optoelectronic properties of metal halide perovskites. *Chem. Rev.* **2016,** *116* (21), 12956-13008.
289. Gélvez-Rueda, M. C.; Hutter, E. M.; Cao, D. H.; Renaud, N.; Stoumpos, C. C.; Hupp, J. T.; Savenije, T. J.; Kanatzidis, M. G.; Grozema, F. C., Interconversion between free charges and bound excitons in 2D hybrid lead halide perovskites. *J. Phys. Chem. C* **2017,** *121* (47), 26566-26574.
290. Wang, S.; Leng, J.; Yin, Y.; Liu, J.; Wu, K.; Jin, S., Ultrafast dopant-induced exciton auger-like recombination in Mn-doped perovskite nanocrystals. *ACS Energy Lett.* **2020,** *5*, 328-

334.
291. Chen, H.-Y.; Chen, T.-Y.; Son, D. H., Measurement of energy transfer time in colloidal Mn-doped semiconductor nanocrystals. *J. Phys. Chem. C* **2010,** *114* (10), 4418-4423.
292. Dey, A.; Ye, J.; De, A.; Debroye, E.; Ha, S. K.; Bladt, E.; Kshirsagar, A. S.; Wang, Z.; Yin, J.; Wang, Y.; Quan, L. N.; Yan, F.; Gao, M.; Li, X.; Shamsi, J.; Debnath, T.; Cao, M.; Scheel, M. A.; Kumar, S.; Steele, J. A.; Gerhard, M.; Chouhan, L.; Xu, K.; Wu, X.-g.; Li, Y.; Zhang, Y.; Dutta, A.; Han, C.; Vincon, I.; Rogach, A. L.; Nag, A.; Samanta, A.; Korgel, B. A.; Shih, C.-J.; Gamelin, D. R.; Son, D. H.; Zeng, H.; Zhong, H.; Sun, H.; Demir, H. V.; Scheblykin, I. G.; Mora-Seró, I.; Stolarczyk, J. K.; Zhang, J. Z.; Feldmann, J.; Hofkens, J.; Luther, J. M.; Pérez-Prieto, J.; Li, L.; Manna, L.; Bodnarchuk, M. I.; Kovalenko, M. V.; Roeffaers, M. B. J.; Pradhan, N.; Mohammed, O. F.; Bakr, O. M.; Yang, P.; Müller-Buschbaum, P.; Kamat, P. V.; Bao, Q.; Zhang, Q.; Krahne, R.; Galian, R. E.; Stranks, S. D.; Bals, S.; Biju, V.; Tisdale, W. A.; Yan, Y.; Hoye, R. L. Z.; Polavarapu, L., State of the Art and Prospects for Halide Perovskite Nanocrystals. *ACS Nano* **2021**.
293. Peulen, T.-O.; Opanasyuk, O.; Seidel, C. A., Combining graphical and analytical methods with molecular simulations to analyze time-resolved FRET measurements of labeled macromolecules accurately. *J. Phys. Chem. B* **2017,** *121* (35), 8211-8241.
294. Giechaskiel, B.; Ntziachristos, L.; Samaras, Z., Calibration and modelling of ejector dilutors for automotive exhaust sampling. *Meas. Sci. Technol.* **2004,** *15* (11), 2199.
295. Delport, G.; Chehade, G.; Ledee, F.; Diab, H.; Milesi-Brault, C.; Trippe-Allard, G.; Even, J.; Lauret, J. S.; Deleporte, E.; Garrot, D., Exciton-Exciton Annihilation in Two-Dimensional Halide Perovskites at Room Temperature. *J. Phys. Chem. Lett.* **2019,** *10* (17), 5153-5159.
296. Goodman, A. J.; Lien, D. H.; Ahn, G. H.; Spiegel, L. L.; Amani, M.; Willard, A. P.; Javey, A.; Tisdale, W. A., Substrate-Dependent Exciton Diffusion and Annihilation in Chemically Treated MoS2 and WS2. *J. Phys. Chem. C* **2020,** *124* (22), 12175-12184.
297. Lee, W.; Han, J. W.; Chen, Y.; Cai, Z.; Yildiz, B., Cation size mismatch and charge interactions drive dopant segregation at the surfaces of manganite perovskites. *J. Am. Chem. Soc.* **2013,** *135* (21), 7909-7925.